Buckling of fibres embedded in a matrix analysed with the discrete element method

Cordewener, Britt H.H.A.

Award date:
2019

BUCKLING OF FIBRES EMBEDDED IN A MATRIX

ANALYSED WITH THE DISCRETE ELEMENT METHOD

MASTER'S THESIS

B.H.H.A. (BRITT) CORDEWENER

23 - 09 - 2019

EINDHOVEN UNIVERSITY OF TECHNOLOGY

BUCKLING OF FIBRES EMBEDDED IN A MATRIX

ANALYSED WITH THE DISCRETE ELEMENT METHOD

Thesis for completing the master's degree of Structural Design and Engineering of the master program Architecture, Building and Planning at the Eindhoven University of Technology.

Thesis

Report number	A-2018.244
Date	September 23, 2019

Educational institution

University	Eindhoven University of Technology
Department	Built Environment
Master program	Architecture, Building and Planning
Unit	Structural Design and Engineering
Chair	Applied Mechanics

Author

Name	B.H.H.A. (Britt) Cordewener
Student number	0842104
Email	b.h.h.a.cordewener@student.tue.nl britt.cordewener@gmail.com

Graduation supervision committee

Chairman	Prof. Dr. ir.	A.S.J. (Akke) Suiker	(TU/e)
2nd supervisor	Dr. ir.	E. (Emanuela) Bosco	(TU/e)
3rd supervisor	Prof. Dr. ir.	H.H. (Bert) Snijder	(TU/e)

Abstract

The application of fibre reinforced composites within the engineering field has increased substantially over the last few years due to their excellent mechanical properties and weight saving ability. For most composites, the compressive strengths reach merely 50 to 60% of their tensile strengths, causing them to be a design limiting feature in many applications. Extensive research is therefore devoted to the analysis of the corresponding failure mechanisms.
In this research, a Discrete Element Method (DEM) model is used to create a simplified and accessible, yet sophisticated model to elaborate on the various relations between physical material properties and the micro-buckling of fibres embedded in a matrix. Rosen's theory is adopted, approaching embedded fibres as aligned and slender columns supported by an elastic foundation representing the matrix. Firstly, the buckling behaviour of a single embedded fibre is modelled and the influence of matrix properties is analysed with the DEM and verified using Finite Element Modelling. The critical buckling load is found to be highly sensitive to small heterogeneities in the bending stiffness of the fibre $E_f I_f$, the fibre length L_f and the foundation modulus of the matrix K_c.
Two ways to compute the foundation modulus of the matrix have been evaluated. Following Su, Liu, Terwagne, Reis, and Bertoldi (2014), the continuous spring stiffness is computed using Kelvin's solution for the displacement field of an infinite unbounded elastic medium subjected to a concentrated force. Alternatively, a simplified approximation for the continuous spring stiffness is computed, using merely the Young's modulus of the matrix. Results show that the value of the spring stiffness is linearly dependent on the matrix-fibre stiffness ratio E_m/E_f and that for low values of the matrix-fibre stiffness ratio, the application of the simple approximation of the foundation modulus by $K_c = E_m$ is allowed.
Plasticity of the matrix is included using a bilinear material model. When modelled in combination with fibre plasticity, plastic matrix behaviour causes the fibres to fail in plastic micro-buckling and using the DEM models, the initiation of fibre kinking is observed.
Secondly, a model for fibre bundles embedded in a matrix is constructed and used to evaluate the influence of initial imperfections and fibre volume fractions on the buckling behaviour of fibres. It is observed that for low fibre volume fractions, fibres may buckle out of phase, depending on their initial imperfections and misalignment. While on contrary, for composites with high fibre volume fractions, the limited distance between adjacent fibres causes the fibres to buckle in phase, despite their possibly in opposite direction imposed initial imperfections.
It is concluded that the DEM models are able to accurately describe the buckling behaviour of embedded fibres. However, since comprehensive FEM and homogenisation models are established in extensive previous research, it is expected that the value of the created DEM models lies in particular in their accessibility and their capability to provide a quick understanding of the governing relations between material properties and the micro-buckling of embedded fibres and the application and implementation of numerical analysis techniques.

Preface

This thesis is the result of my graduation project on the buckling behaviour of unidirectional fibres embedded in a matrix, analysed with the Discrete Element Method. It has been written in partial fulfilment of the requirements for the degree of Master of Science in Architecture, Building and Planning with a specialisation in Structural Engineering and Design at the Eindhoven University of Technology.

I would like to express my gratitude to the members of my graduation supervision committee, Prof. dr. ir. Akke Suiker, Dr. ir. Emanuela Bosco and Prof. dr. ir. Bert Snijder, for their time, guidance and support over the past year. My sincere thanks go to Akke Suiker and Emanuela Bosco, since I could always step by in case I encountered problems during this project and they were always willing to help me. It has been a challenging project and their patience, knowledge and encouragement were incredibly helpful during this research.

Furthermore, I would like to thank my fellow students and friends for their support and the great atmosphere in Vertigo, even during the summer holidays. Special thanks go to Caroline Koks and Derk Bos, for always being critical sparring partners to me and their help with the preparation of my colloquia.

Last but not least, I would like to thank my family for their unconditional support and patience during my studies, especially during this last year. Your faith and support motivated me whenever needed throughout this project. It has been an inspiring year in which I have been working with great pleasure and dedication on this interesting subject.

Britt Cordewener
Eindhoven, September 2019

Contents

1 Introduction

The application of fibre composites within the engineering field has increased substantially over the last few years due to their excellent mechanical properties and weight saving ability (Scappin, 2017; L. Zhou, Zhao, Liu, & Zhang, 2018). With this, the attention for failure mechanisms of fibre composites has increased as well. Though significant improvements have been made to the tensile strength, impact resistance and toughness, the longitudinal compressive performance of Fibre Reinforced Composites (FRC) has not been increased. For most fibre composites, their compressive strength is substantially less than their tensile strength. The compressive strengths of unidirectional carbon fibre epoxy composites, for example, are approximately 50 to 60% of their tensile strengths, causing them to be a design limiting feature in many applications (Fleck & Budiansky, 1991; Ueda, Hiraga, & Nishimura, 2011).
Therefore, the compressive failure of composite materials has been the subject of extensive previous research in which several competing failure modes have been identified. Elastic micro-buckling, plastic micro-buckling, fibre crushing, splitting, buckle delamination and shear-band formation are regarded as the main competing mechanisms of compressive failure of unidirectional long fibre composites. The governing mode appears to be strongly correlated with the shear properties of the matrix and the gradation of initial imperfections such as the fibre misalignment. While having low shear strengths, micro-buckling - the localised buckling of fibres in a cooperative manner - is observed as the compressive failure of unidirectional polymer-matrix composites (Fleck, 1997). This particular compressive failure mechanism will be the main topic of this research.
In Section 1.1 a short introduction to fibre composite materials is given, followed by a recap of the main compressive failure mechanisms in Section 1.2. The introduction is concluded with the outline of the research scope in Section1.3.

1.1 Fibre Composites

Composite materials are defined as engineered materials consisting of two or more constituents with different physical and/or chemical properties that remain separate and distinct in the finished material. On a microscopic scale, this translates into two or more distinct *phases* which are separated by a certain *interface*. The continuous phase is usually referred to as the *matrix*, whereas the other phase is known as the *reinforcement* as it enhances the properties of the matrix (Savage, 2010).
Fibre Reinforced Composites (FRC) are defined as composite materials in which the reinforcement of the matrix is provided by, either long fibres (continuous fibre reinforced composites), shown in Figure 1.1, or short fibres (discontinuous fibre reinforced composites). Fibres of high strength and modulus are embedded in or bonded to the matrix while a distinct interface remains between them. The fibres are considered as the principal load-carrying constituents, whereas the surrounding matrix acts mainly as a load-transferring medium between the fibres and a binder to maintain the shape of the product and orientation of the fibres (Mallick, 2008).
The arrangement of fibres in a composite is defined as the *fibre architecture* and is influencing the properties, failure mechanisms and the processing of the fibre composite. The mechanical properties of composite materials are influenced by fibre architecture features such as fibre orientation, fibre continuity and fibre interlocking. Depending on the fibre continuity, the fibre architecture can be defined as one-, two- or three-dimensional for continuous fibres and can be either oriented

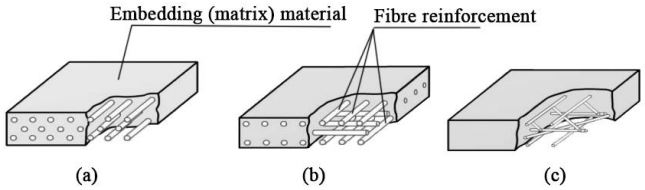

Figure 1.1: Structure of a continuous fibre reinforced composite with (a) unidirectional, (b) bidirectional and (c) multidirectional fibre orientation.

or randomly distributed. Whereas the latter results in isotropic properties of the material, the composite properties are strongly related to the fibre orientation in case of other fibre architectures. In one-dimensional fibre architectures, often referred to as unidirectional fibre composites, the majority of the fibres run in one direction. For those composites, usually fibres with high strength and stiffness are combined with lower strength matrix materials with higher toughness to endow the composite with adequate in-plane strength and ductility. Accordingly, composites with high strength and modulus in the fibre direction, but significantly lower strength and modulus in the transverse direction, are produced.
Two-dimensional continuous fibre architectures can be distinguished as either bidirectional, with woven or interlaced fibre yarns in perpendicular directions, or multidirectional. Finally, three-dimensional architectures can be created by weaving, braiding or stitching a stack of woven fabrics (Mallick, 2008; Fleck, 1997).

1.2 Compressive Failure Mechanisms of Unidirectional Fibre Composites

Depending on the mechanical properties of the fibre and matrix, a number of competing failure mechanisms have been identified to affect the compressive strength of continuous unidirectional fibre composites. The governing compressive failure mode strongly correlates with the matrix properties and initial imperfection of the fibres. Extensive theoretical and experimental studies have resulted in six most common compressive failure modes, which are summarised in sections 1.2.1 to 1.2.6.

1.2.1 Elastic Micro-Buckling

In fibre reinforced composites with a relatively low matrix modulus compared to the fibre modulus, failure in longitudinal compression is often initiated by localised buckling of the fibres in a cooperative manner. The first model for the phenomenon of elastic micro-buckling, a shear buckling instability in which the matrix deforms in simple shear, was developed by Rosen (1965). Rosen approached fibres as being perfectly aligned elastic and slender columns supported by an elastic foundation, representing the matrix material. The overall composite plate is assumed to be stiff and free of buckling in compression on the macro-scale. However, on the micro-scale, the individual slender fibres can buckle in two distinct micro-buckling patterns; either in transverse buckling mode, or in shear buckling mode, causing the matrix to undergo extensional straining in transverse direction or shearing parallel to the fibres respectively, see Figure 1.2 (Fleck, 1997; Fleck & Budiansky, 1991). For composites with low fibre volume fractions, $v_f < 0.2$, the transverse or extensional buckling mode occurs, resulting in extensional strain in the matrix because of the out-of-phase buckling of the fibres. For composites with a higher fibre volume fraction, $v_f > 0.2 - 0.3$, the shear buckling mode is governing and creates in-phase deformation of the fibre and matrix. Assuming

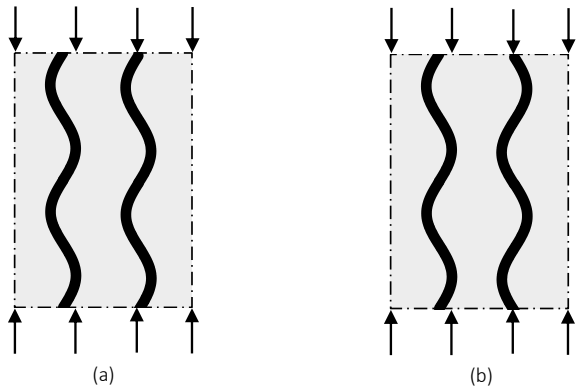

Figure 1.2: Elastic micro-buckling of fibres in a unidirectional continuous fibre composite under longitudinal compressive loading in (a) shear buckling mode and (b) extensional buckling mode.

the fibres to be initially perfectly aligned, Rosen predicted the elastic compressive strengths for the transverse buckling mode and shear buckling mode as

$$\text{Transverse buckling mode:} \qquad \sigma_{\mathrm{c}} = 2\mathrm{v}_f \left(\frac{\mathrm{v}_f E_{\mathrm{m}} E_f}{3\left(1-\mathrm{v}_f\right)} \right)^{1/2}, \tag{1.1a}$$

$$\text{Shear buckling mode:} \qquad \sigma_{\mathrm{c}} = \frac{G_{\mathrm{m}}}{\left(1-\mathrm{v}_f\right)} + \frac{\pi^2}{3} \left(\frac{d}{\lambda} \right)^2 E_f \mathrm{v}_f, \tag{1.1b}$$

respectively, where G_{m} denotes the matrix shear modulus, Ef and E_{m} are the Young's modulus of the fibre and matrix respectively, v_f is the fibre volume fraction, d is the fibre diameter and λ the buckling wavelength.
Since most fibre reinforced composites contain fibre volume fraction of over 30%, the shear buckling mode is governing for most composites. In the predicted compressive strength for this buckling mode, as given in Equation 1.1b, G represents the contribution from matrix shear, whereas the remaining term, $\frac{\pi^2}{3}\left(\frac{d}{\lambda}\right)^2 E_f \mathrm{v}_f$, is the contribution to the compressive strength provided by the bending resistance of the fibres. Accordingly, it is noted that the lowest strength is observed for the long-wavelength limit and that the role of fibre bending is negligible for approximating the compressive strength of the composite. This reduces Equation 1.1b to the commonly given equation for the compressive strength of fibre composites subjected to shear buckling

$$\sigma_c = \frac{G_{\mathrm{m}}}{\left(1-\mathrm{v}_f\right)}. \tag{1.2}$$

Though Rosen's equation is, according to experimental research, accurate for matrices with a linear elastic response, more typically, polymer and metal matrices of long-fibre composites show a non-linear behaviour during compression tests. For those composites, the observed longitudinal compressive strengths are generally about $\sigma_{\mathrm{c}} = \frac{1}{4}\frac{G_{\mathrm{m}}}{(1-\mathrm{v}_f)}$ due to the occurrence of highly imperfection-sensitive plastic micro-buckling. (Mallick, 2008; Fleck, 1997; Fleck & Budiansky, 1991; Parnes & Chiskis, 2002; Scappin, 2017)

1.2.2 Plastic Micro-Buckling

Plastic micro-buckling is a shear instability occurring at sufficiently large strains for the matrix to deform in a non-linear manner. This compression failure mode occurs in localised areas in which the fibres are initially misaligned from the loading direction. Fibre bundles rotate or tilt in these areas by an additional angle ϕ from their initial configuration, causing large shear deformation in the surrounding matrix and the so-called kink bands, see Figure 1.3a. Hence, the failure mechanism is also referred to as fibre kinking. As stated by Argon (1972) and Budiansky (1983), the compressive strength of a fibre composite is highly imperfection sensitive and determined by the

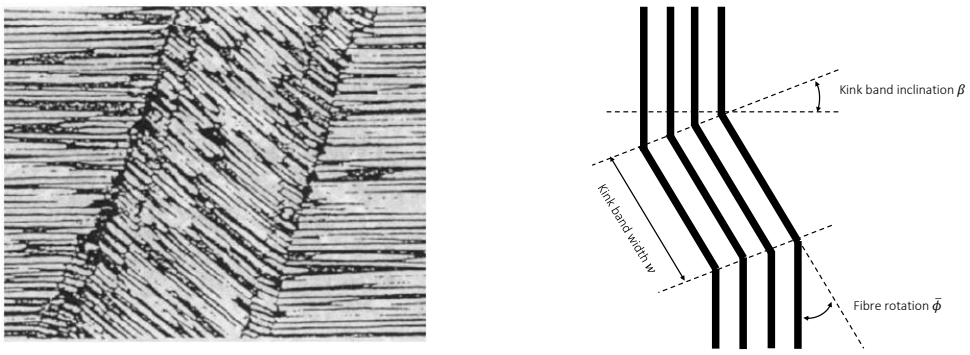

(a) (b)

Figure 1.3: (a)Micrograph of plastic micro-buckling or fibre kinking (Feld et al., 2011) and (b) the corresponding geometrical parameters following the definition by Argon and Budiansky.

fibre misalignment and plastic shear deformation in the matrix. In accordance with elastic microbuckling, the contribution of the bending resistance of the fibres to the compressive strength of the fibre composite is neglected in their research. The fibres are assumed to suffer from an initial uniform misalignment, expressed by the initial fibre rotation $\bar{\phi}$ over a band of infinite length and finite width w. The kin band inclination β is defined as the rotation of the unit normal to the band of imperfection with respect to the fibre direction (Figure 1.3b). Assuming an initial kink band inclination $\beta = 0$, Argon (1972) defined the critical compressive stress for a rigid perfectly plastic composite with yield strength k in longitudinal shear

$$\sigma_c = \frac{k}{\bar{\phi}}. \tag{1.3}$$

Once the critical compressive strength is reached, an additional rotation ϕ will develop and the compressive stress decreases with increasing ϕ in accordance with $\sigma_c = \frac{k}{\bar{\phi}+\phi}$. Budiansky (1983) extended the Argon formula, Equation 1.3, for elastic-perfectly plastic composites with a corresponding yield strain in longitudinal shear $\gamma_y = k/G$, resulting in the critical compressive stress

$$\sigma_c = \frac{k}{\gamma_y + \bar{\phi}} = \frac{G}{1 + \frac{\bar{\phi}}{\gamma_y}}. \tag{1.4}$$

If the initial inclination angle of the fibres becomes zero ($\bar{\phi} = 0$), which is the case for initially perfectly aligned fibres, Equation 1.4 approaches Rosen's equation for the minimum bifurcation stress in the long-wavelength limit (Equation 1.2). Alternatively, Equation 1.4 is asymptotically equivalent to Argon's formula (Equation 1.3) for large initial inclination angles ($\bar{\phi}$).(Mallick, 2008; Scappin, 2017)

1.2.3 Fibre crushing

When the matrix of a composite is sufficiently strong and stiff, other compressive failure mechanisms on a fibre scale can intervene. In case the longitudinal strain of the composite is equal to the fibre compressive failure strain, fibre crushing will occur (Figure 1.4a)). A variety of mechanisms may be associated with fibre crushing, examples can be found in plastic yielding, longitudinal splitting or microscopic buckling within each fibre. The latter resulting in kink bands within the fibres of widths less than the fibre radius. Carbon fibres, for instance, fail in compression by a combination of longitudinal splitting and microscopic buckling. The governing fibre crushing mechanism is determined by the specific fibre properties. For microscopic buckling, the corresponding compression strength of the fibre, σ_{fc}, is of the order $G/4$, where G is the longitudinal shear modulus of the fibre (Fleck, 1997; Scappin, 2017).

1.2.4 Splitting

Splitting occurs as compressive failure mode whenever the matrix stiffness exceed the fibre stiffness. In this case the matrix cracks in tensile mode I, parallel to the fibre direction, initiating at local voids or imperfections of the matrix (Figure 1.4b). This compressive failure mode is associated with a low toughness of the matrix material and high porosity. The mechanism is common for ceramic-ceramic composites such as SiC-SiC. For those composites, the elastic modulus of the fibres equals approximately half of the elastic modulus of the matrix, causing the fibres to act as compliant inclusions helping to induce splitting. The corresponding compression strength of such composites is approximated by

$$\sigma_{\mathrm{c}} = \frac{C(f)K_{IC}}{\sqrt{\pi a}}, \tag{1.5}$$

where K_{IC} represents the mode I fracture toughness of the matrix, a the mean radius of pores perpendicular to the loading direction and $C(f)$ a coefficient depending on the composite porosity f, ranging from 2 to 15 for 30% and 0.3% porosity, respectively (Fleck, 1997).

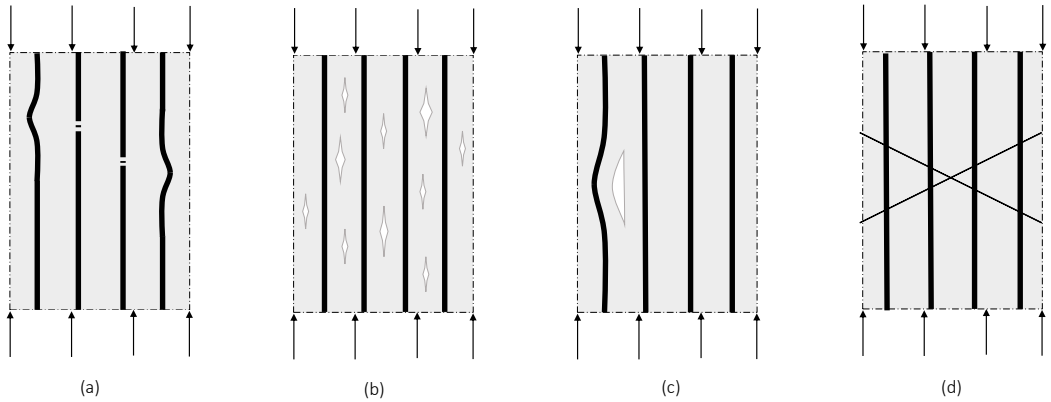

Figure 1.4: Compressive failure modes of composites: (a) Fibre crushing, (b) Matrix splitting, (c) Buckle delamination, (d) Shear band formation.

1.2.5 Buckle delamination

Buckle delamination is associated with buckling of the surface layer, causing splitting parallel to the fibre direction (Figure 1.4c). The buckling of the surface layer is initiated due to poor cohesion between the fibre and matrix over a finite length. Buckle delamination is an important concern in the application of fibre composites, since post-impact compressive strength can be drastically reduced due to debonding caused by impact events. Subsequent compressive loading can then induce buckle-delamination growth. Overall, this failure mode is associated with a low matrix toughness and the presence of zones with reduced cohesion. Using the Euler buckling condition, the critical compressive stress for the initiation of buckle delamination in a composite with a subsurface crack in an isotropic homogeneous solid is derived as

$$\sigma_c = \frac{\pi^2}{12} E \left(\frac{h}{b} \right)^2, \tag{1.6}$$

where E is the homogenised elastic modulus of the composite, h is the depth at which delamination occurs and $2b$ equals the initial crack length (Scappin, 2017).

1.2.6 Shear band formation

For composites with extremely low fibre volume fraction and polymer-matrix, shear band failure can dominate. In this failure mode, yielding and fracture of the matrix occur in a band, oriented at about 45 degrees with respect to longitudinal loading direction (Figure 1.4d). This failure mode is in essence identical to the failure mode occurring in the unreinforced matrix material, and is therefore not considered to be significant at conventional fibre volume fractions.

1.2.7 Failure maps

The competition between the different compressive failure mechanisms can be displayed in so-called failure maps. Fleck (1997) presented in his work a two- and three-dimensional map showing the region of dominance of the various competing failure mechanisms as introduced in Sections 1.2.1 to 1.2.6, see Figure 1.5a and 1.5b. Fleck constructed the map by considering the boundaries between each mechanism:

(i) By comparison of equations 1.2 and 1.4, plastic micro-buckling is expected to dominate elastic micro-buckling when $\frac{\overline{\phi}}{\gamma_y} > 0$.

(ii) Fibre crushing dominates buckle delamination when the compressive strength associated with it is less than the compressive strength given by Equation 1.6 for buckle delamination. By equating both compressive strengths, fibre crushing is expected to occur when $\frac{b}{h} < \frac{\pi}{(2\sqrt{3\varepsilon_{fc}})}$.

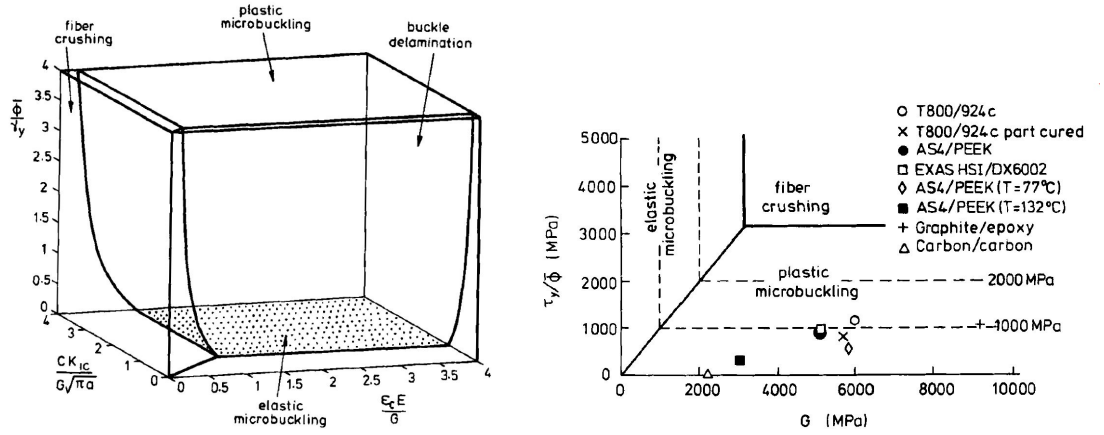

(a) (b)

Figure 1.5: (a) Three dimensional failure map showing region of dominance of competing failure mechanisms, (b) two-dimensional failure map with the test data of several commercial polymer matrix composites failing by plastic micro-buckling (Fleck, 1997).

(iii) Using Equation 1.4, fibre crushing is found to be governing over plastic micro-buckling when

$$\frac{\varepsilon_{fc}E}{G} < \frac{1}{1+\left(\overline{\phi}/\gamma_y\right)}, \tag{1.7}$$

where E and G represent homogenised properties of the composite, ε_{fc} is the fibre-crushing strain, $\overline{\phi}$ is the initial fibre rotation and γ_y is the yield strain of the composite in longitudinal strain.

(iv) Finally, equating 1.5 and 1.4, splitting is expected to occur in preference to plastic micro-buckling when

$$\frac{CK_{IC}}{G\sqrt{\pi a}} < \frac{1}{1+\left(\overline{\phi}/\gamma_y\right)}. \tag{1.8}$$

The simpler, two-dimensional version of the map in Figure 1.5b uses the in-plane shear modulus of the composite G and ratio of in-plane shear strength τ_y, with respect to fibre misalignment angle $\overline{\phi}$ as axes. It is noted that an increased compressive strength could be achieved by increasing τ_y and decreasing $\overline{\phi}$ without the intervention of fibre crushing. However, the demand for improved toughness of composites in common practice causes a progressive decrease in the shear strength of the matrix. This leaves the reduction of the fibre misalignment, $\overline{\phi}$, as main strategy to increase compressive strengths of composites (Fleck, 1997).

1.3 Research scope

In this research the influence of physical properties on the buckling stability of fibres embedded in a matrix is studied, using a linear and non-linear Discrete Element Method (DEM).
With the rapid progress in applications of non-linear finite element and allied computational methods, extensive previous research has been devoted to the analysis of non-linear stability problems, among which the buckling analysis of fibres in composite materials. Though these models are able to accurately describe the behaviour of fibre composites, it is frequently noted that they need large computational capabilities, tend to be too complex and require an exceptional understanding of the user (El-Naschie, Wu, & Wifi, 1988).
In the present work, alternatively, it is tried to elucidate the various relations between physical properties and the micro-buckling of fibres using a simplified and accessible, yet sophisticated mathematical model constructed in MATLAB.
Following El Naschie (1990a), based on the classical work of Hencky, the discrete element technique is adopted and implemented for the analysis of the micro-buckling of fibres in a composite.

Moreover, the present research initially follows Rosen's theory by approaching fibres as being perfectly aligned elastic and slender columns supported by an elastic foundation representing the matrix material. This allows for the exclusive modelling of the fibre material, in contrast to complex contemporary models, often containing fibre, matrix and interface elements.
In Section 2, section 2.1, the analytical model based on Rosen's theory is further introduced. The discrete element technique and resulting numerical model, adopting the principle of stationary total potential energy, are elaborated in section 2.2. The parametrically-built model is validated for the buckling of a single unsupported fibre and a mesh refinement study has been conducted. The support of the matrix against buckling of the fibres is modelled by linear elastic translation springs. The bifurcation load for individual fibres is obtained and the model is validated by comparison with the analytical solution for a beam on an elastic foundation loaded by a point load.
Imperfections are introduced and a non-linear buckling analysis is performed using a Newton-Raphson incremental-iterative procedure. The results are verified using a Finite Element Method (FEM) model.
In Section 3, the behaviour of individual embedded fibres is elaborated. A parametric study is conducted, evaluating the spring stiffness representing the matrix support. Non-linear matrix behaviour is implemented, using a bilinear material model for the matrix. The influence of non-linear material parameters on the buckling behaviour of the fibres is examined.
In Section 4, the model is extended for multiple embedded fibres. The influence of initial imperfections and plastic fibre behaviour, using a bilinear material model for the fibre, on the buckling of multiple unidirectional fibres is reviewed. Finally, the conclusions of this research are presented in Section 5 and recommendations for further research are provided.

2 Methodology

2.1 Analytical Model

An analytical solution for the bifurcation load of individual fibres in a matrix is derived. An elastic and slender fibre, embedded in an elastic medium is considered and subjected to axial compression. Based on the Euler-Bernoulli beam theory, the relation between the Young's modulus of the matrix and the buckling of an individual fibre is presented.

2.1.1 Method

Rosen's approach to fibres as being perfectly aligned elastic and slender columns supported by an elastic foundation representing the matrix is adopted. As in the Winkler foundation model, the elastomeric matrix is simplified as an array of springs with continuous spring stiffness K_c, often referred to as the foundation modulus in Newton per square meter (Timoshenko & Gere, 1961; Su et al., 2014; Parnes & Chiskis, 2002; Andrianov, Kalamkarov, & Weichert, 2012).
Assuming small strains and small rotations, the differential equation for an individual embedded elastic fibre can be derived from the general differential equation from the Euler-Bernoulli beam theory

$$\frac{\partial^2}{\partial x^2}\left(EI\frac{\partial^2 w}{\partial x^2}\right) - \frac{\partial}{\partial x}\left(N_0\frac{\partial w}{\partial x}\right) = q_z. \tag{2.1}$$

By assuming the Young's modulus E_f and the second moment of area I_f of the fibre to be constant over the length of the fibre, the normal force in the fibre to equal the applied compressive force F, $N_0 = -F$, and express the lateral restraint provided by the matrix in the foundation modulus as $q_z = K_c w$, Eq. 2.1 becomes

$$E_f I_f \frac{\partial^4 w}{\partial x^4} + F\frac{\partial^2 w}{\partial x^2} + K_c w = 0. \tag{2.2}$$

Introducing the fibre length L_f, the normalised displacement, $\omega = \frac{w}{L_f}$, and position along the fibre axis, $\chi = \frac{x}{L_f}$, allows for Eq. 2.2 to be rewritten in dimensionless form,

$$\frac{\partial^4 \omega}{\partial \chi^4} + \overline{F}\frac{\partial^2 \omega}{\partial \chi^2} + \overline{\mathrm{K}}_c\omega = 0, \tag{2.3}$$

where $\overline{F} = \frac{FL_f^2}{E_f I_f}$ and $\overline{\mathrm{K}}_c = \frac{\mathrm{K}_c L_f^4}{E_f I_f}$ are the dimensionless compressive force and continuous spring stiffness of the matrix (foundation modulus), respectively.
When both ends of the fibre are free to rotate and restricted against lateral displacements, the boundary conditions of the system are given by

$$\begin{aligned} &\chi = 0, \quad \omega(0) = 0, \quad M(0) = -\frac{EI}{L_f}\frac{d^2\omega}{d\chi^2} = 0, \\ &\chi = 1, \quad \omega(1) = 0, \quad M(1) = -\frac{EI}{L_f}\frac{d^2\omega}{d\chi^2} = 0, \end{aligned} \tag{2.4}$$

and the general solution of the differential equation has the form $\omega_n = C\sin(\alpha_n\chi)$, with $\alpha_n = n\pi$ and n denoting the mode number.
Substituting the general solution into the differential equation, Eq. 2.2 and dividing by $\sin(\alpha_n\chi)$ yields the non-trivial solution

$$\alpha_n^4 - \overline{F}_n\alpha_n^2 + \overline{\mathrm{K}}_c = 0, \tag{2.5}$$

which, with the above expression for α_n, gives the analytical solution for the buckling load of a continuously supported fibre as

$$\overline{F}_n = n^2\pi^2 + \frac{\overline{\mathrm{K}}_c}{n^2\pi^2} \quad \text{where } n = 1, 2, 3, \ldots \tag{2.6}$$

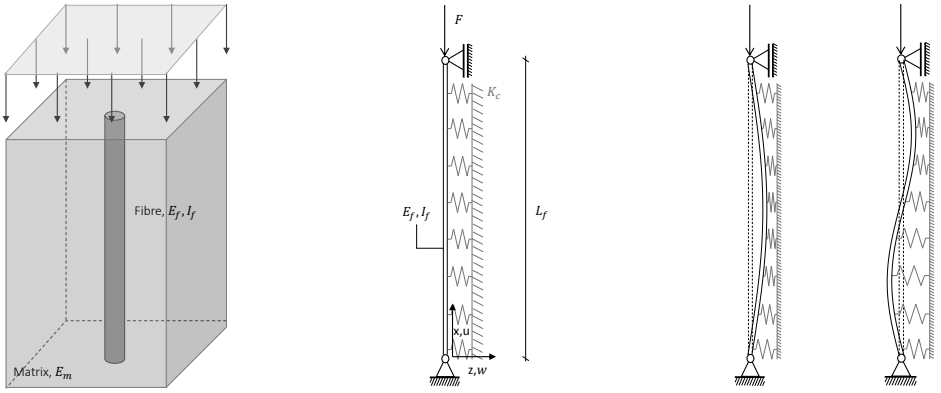

Figure 2.1: Theoretical model of an individual fibre embedded in a matrix subjected to compression with corresponding two-dimensional interpretation and illustration of the first and second buckling mode.

2.1.2 Observations

The critical buckling force of an individual fibre embedded in a matrix can be found upon calculation of the mode number that minimises $\overline{F}_n$ in Eq. 2.6, in other words by solving $\frac{\partial \overline{F}_n}{\partial n} = 0$. The result is shown in Figure 2.2. The governing buckling mode increases with increasing continuous spring stiffness representing the matrix.
It is noted that, in contrast to fibres not embedded in a matrix, the critical buckling load does not decrease monotonically with increasing fibre length. Instead, the governing buckling mode with corresponding number of half waves becomes highly sensitive to small heterogeneities in the bending stiffness of the fibre, $E_f I_f$, the fibre length L_f and the foundation modulus K_c.

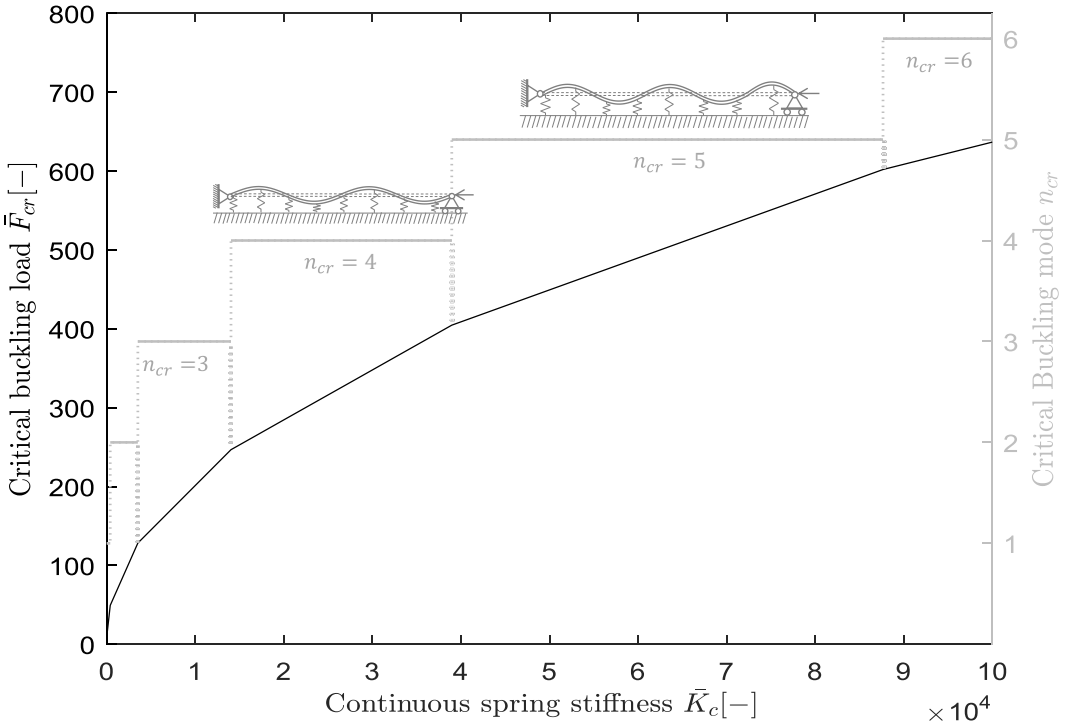

Figure 2.2: Analytically determined dimensionless critical buckling load of an individual embedded fibre. The governing buckling mode n_{cr}, is shown on the right axis in grey.

2.2 Numerical Model

A numerical model is constructed to evaluate the buckling behaviour of fibres in a matrix using MATLAB. For the analytical model, the differential equation resulting from the equilibrium formulation is used to derive the critical buckling load. For the numerical model, however, an energy approach is adopted, as presented in Section 2.2.1. The Discrete Element Method is applied and introduced in Section 2.2.2. The numerical approach is verified for fibres without matrix support and a mesh refinement study regarding the number of discrete elements is performed.
A non-linear buckling analysis is required to study the influence of the matrix properties. The non-linear solving strategy is elaborated in Section 2.2.5.

2.2.1 Method

As an alternative to equilibrium formulations, energy considerations such as the principle of stationary total potential energy, may be used to analyse stability problems. This principle is derived from the principal of virtual work and is closely related to the Euler-Lagrange differential equation and the calculus of variations. It states that for a system to be in equilibrium, the total potential energy must have a stationary value (Alfutov, 2011; El Naschie, 1990b).
The potential energy of a conservative mechanical system is defined as the internal elastic deformation (strain) energy stored inside the system minus the work done by the external forces acting on the system during a particular deformation,

$$V = U + L_p, \tag{2.7}$$

where U is the strain energy and L_p is the load potential, defined as a quantity of which the first variation (its first-order change) is equal to minus the variational work of the loading.
The principle of stationary total potential energy, also referred to as the stationarity condition of the Langrange functional, states that for equilibrium the first variation vanishes. In this particular application for stability problems, only the displacement field is subjected to variation, which in the present work is expressed in terms of the nodal rotation vector $\boldsymbol{\phi}$, see Eq. 2.8a. The stationarity condition should hold for arbitrary variations in the displacement field, allowing Eq. 2.8a to be written as 2.8b (Alfutov, 2011; Hoff, 1966; El Naschie, 1990b).

$$\delta V = \frac{\partial V}{\partial \boldsymbol{\phi}} \delta \boldsymbol{\phi} = 0 \qquad \forall\, \delta \boldsymbol{\phi} \tag{2.8a}$$

$$\delta V = \frac{\partial V}{\partial \boldsymbol{\phi}} = 0 \tag{2.8b}$$

The obtained bifurcation load at which the loss of stability in the initial equilibrium state of a conservative system occurs, the principle of stationary potential energy is applied to find equilibrium in the deformed state, see Section 2.2.4. For non-linear buckling analysis, Eq. 2.8b is solved for the nodal rotation vector $\boldsymbol{\phi}$ to find all equilibrium positions of the structure within a certain range.

2.2.2 Discretization

In this research, a discrete approximation technique is used for the buckling analysis of fibres embedded in a matrix including imperfections and non-linear material behaviour.
The Discrete Element Method is rather intuitive and can be regarded as an elementary version of the Finite Element Method. In this method, a structure is regarded as a fictitious discrete system consisting of a certain number of rigid elements interconnected with elastic rotational springs. In other words, the original continuous beam is replaced by a discrete mechanical model with straight and rigid elements connected at frictionless joints by rotational springs with an adequate spring constant which approximates the bending stiffness of the continuous beam. Due to this localised stiffness assumption, the nodal rotations are the only degrees of freedom of the system, simplifying the kinematic expressions of deformations and consequently the non-linear formulations (El-Naschie et al., 1988).

2.2.2.1 Bending stiffness of the fibre

To accomplish the transition from the continuous beam properties to the discrete rotational springs, the Euler-Bernoulli beam theory is used, given by

$$M = EI\frac{d^2w}{dx^2} = EI\frac{d\phi}{dx}, \tag{2.9}$$

with EI the bending stiffness of the fibre (El Naschie, 1990c, 1990a). Eq. 2.9 can be written in finite difference form as

$$M = EI\frac{\mathrm{d}\phi}{\mathrm{d}x} = EI\lim_{\Delta x\to 0}\frac{\Delta\phi}{\Delta x} \simeq EI\frac{\Delta\phi}{\Delta x} \simeq \frac{EI}{\Delta x}\Delta\phi, \tag{2.10}$$

where $\Delta\phi$ is the change in angle ϕ of the tangent to the line of deflection.
For the discrete system, the bending moment for a linear rotational spring evidently equals

$$M = C\cdot\Delta\phi. \tag{2.11}$$

Since the bending moment has to be the same in both the discrete and the continuous system, equations 2.10 and 2.11 can be equated. Hence, the stiffness of the rotational springs can be determined as

$$C = \frac{EI}{\Delta x} = \frac{EI}{L/m}, \tag{2.12}$$

in which L and m are the total length of the fibre and the number of elements used for the discrete element approximation, respectively. Finally, the obtained rotational spring stiffness can be rewritten in dimensionless form as

$$\overline{C} = \frac{CL}{EI} = m[-]. \tag{2.13}$$

2.2.2.2 Matrix support

The buckling of an individual embedded fibre is constrained by the stiffness of the adjacent matrix material. The elastic foundation representing the matrix is discretised for the numerical model in discrete linear elastic translational springs with stiffness k in $[N/mm]$. Hence, the support is localised at the nodes between the rigid discrete elements, see Figure 2.3, and the discrete spring stiffness in $[N/mm]$ or in dimensionless form is given as

$$k\left[\frac{N}{mm}\right] = \frac{K_cL}{m}, \tag{2.14a}$$

$$\overline{k}\,[-] = \frac{\overline{\mathrm{K}}_c}{m} = \frac{\mathrm{K}_cL_f^4}{E_fI_fm}. \tag{2.14b}$$

Besides the horizontal translational springs representing resistance to buckling of the fibres created by the stiffness of the matrix, also vertical translational springs representing the resistance due to friction between the matrix and the fibres are implemented. Discretization of these springs is carried out in a similar manner. The value for those vertical and horizontal springs and their influence of the buckling behaviour of the embedded fibre is evaluated in parameter study in Section 3.

2.2.3 Boundary conditions

In this research, four boundary conditions of an embedded fibre are considered; a simply supported system (pinned - pinned), a cantilevered system (clamped - free), a clamped system (clamped - clamped) and a clamped - pinned system. The boundary condition is reflected in the total potential energy by means of a rotational spring and by the application of an additional kinematic constraint equation. To illustrate this, Figure 2.3 is provided.
For clamped connections, an additional rotational spring is added in the mechanical discrete model

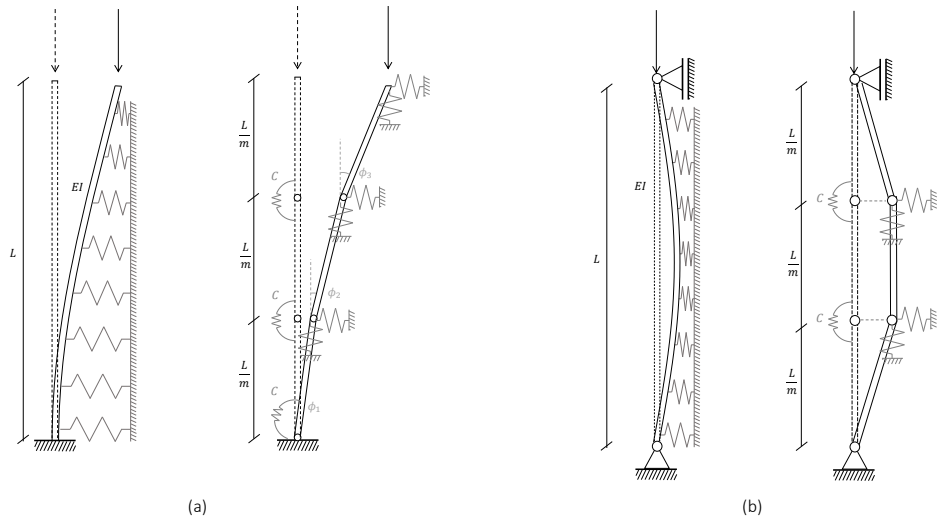

Figure 2.3: Discretization of a cantilevered embedded fibre (a) and a simply supported fibre (b), note the extra rotational spring to model the clamped connection.

of the fibre. The spring stiffness is set equal to the derived spring stiffness corresponding to the bending stiffness of the fibre, which is obviously not an accurate approximation for the clamped behaviour. This is however inherent to the applied discretization method and still provides reasonable approximations of the buckling behaviour of the fibre, as will be shown in Section 2.2.4.1. Moreover, an additional kinematic constraint equation has to be satisfied for all boundary conditions except for the cantilevered fibre, to ensure that the horizontal top displacement of the fibre equals zero. The corresponding equilibrium solution of the system is established by formulating an auxiliary potential Φ^* that combines the total potential energy of the system as derived in Section 2.2.1, with the additional kinematic constraint equation for the essential boundary condition at the top of the fibre

$$\Phi^* = V + \Lambda f(\boldsymbol{\phi}), \tag{2.15}$$

in which Λ is the unknown Lagrange multiplier and the additional kinematic constraint equation has the form $f(\boldsymbol{\phi}) = \frac{L}{m}\sum_{i=1}^{m}\sin(\phi_i)$. Stationarity of the auxiliary potential is then expressed by

$$\delta\Phi^* = \left(\frac{\partial V}{\partial \boldsymbol{\phi}} + \frac{\partial(\Lambda \cdot f(\boldsymbol{\phi}))}{\partial \boldsymbol{\phi}}\right) \cdot \delta\boldsymbol{\phi} + \frac{\partial(\Lambda \cdot f(\boldsymbol{\phi}))}{\partial \Lambda} \cdot \delta\Lambda = 0, \tag{2.16}$$

which for arbitrary variations $\delta\boldsymbol{\phi}$ and $\delta\Lambda$ leads to the set of coupled equations

$$\begin{aligned} \frac{\partial V}{\partial \boldsymbol{\phi}} + \frac{\partial(\Lambda \cdot f(\boldsymbol{\phi}))}{\partial \boldsymbol{\phi}} &= 0 \\ \frac{\partial(\Lambda \cdot f(\boldsymbol{\phi}))}{\partial \Lambda} = f(\boldsymbol{\phi}) &= 0. \end{aligned} \tag{2.17}$$

Depending on the boundary conditions, either Eq. 2.8b or the set of equations 2.17 can be solved for F and $\boldsymbol{\phi}$ using a linear or non-linear solving technique as elaborated in sections 2.2.4 and 2.2.5 respectively.

2.2.4 Linear buckling analysis

For a linear buckling analysis, one starts from the equilibrium conditions derived from the stationarity of either the total potential energy or the auxiliary potential of the embedded fibre, equations 2.8b and 2.17 respectively. For small angles $0 < |\phi| \ll \frac{\pi}{2}$, the equations may be linearised around the initial state, using $\sin\phi \approx \tan\phi \approx \phi$ and $\cos\phi \approx 1$. The resulting homogeneous linearised equations of the elastic stability theory can be applied for detection of the bifurcation points of

the initial equilibrium state and description of the new equilibrium configurations of the system in the vicinity of the bifurcation points to an accuracy of a scale factor (Alfutov, 2011).
The homogeneous linearised equations can be reformulated in matrix-vector format resulting in a global stiffness matrix of the system and a column vector of the unknown variables, i.e. the degrees of freedom of the system. A non-trivial solution can be found by solving the eigenvalue problem and equating the determinant of the global stiffness matrix to zero, that is by solving the m-th order polynomial characteristic equation of the system. The buckling modes or bifurcational displacements of the fibre related to these new equilibrium configurations are found up to the accuracy of a scale factor by substituting the corresponding buckling loads into the matrix-vector formulation.

2.2.4.1 Validation and mesh refinement

In the present work, a parametric MATLAB code using the method as described in the previous sections, is created for the linear buckling analysis of an individual embedded fibre. The results of this numerical model are validated using the analytical solution obtained in Section 2.1, see Figure 2.4. The bifurcation load of the embedded fibre is shown for a certain range of the continuous spring stiffness representing the matrix support. The results are plotted for four different discrete approximations, $m = 2, 3, 4, 8$ as well as for the analytical solution.
As observed in Section 2.1.2, the critical buckling mode n_{cr} is highly sensitive to the continuous spring stiffness of the matrix. The ability of a certain number of rigid discrete elements to approximate the analytical buckling load is strongly correlated with the governing buckling mode. From Figure 2.4 it is noted that though DEM models with two and three elements may be able to approximate the buckling force for a governing first and second buckling mode respectively, a increasing error is observed for higher governing buckling modes. This can be easily explained by the fact that in a discrete element model, no displacement is allowed over the fibre axis itself and the degrees of freedom are localised in the nodes. Hence, DEM models with two and three elements are unable to describe the sinusoidal shape of higher buckling modes than the first and second order, respectively. Therefore, it is concluded that the minimum number of required discrete elements equals $m_{min} = n_{cr} + 1$.

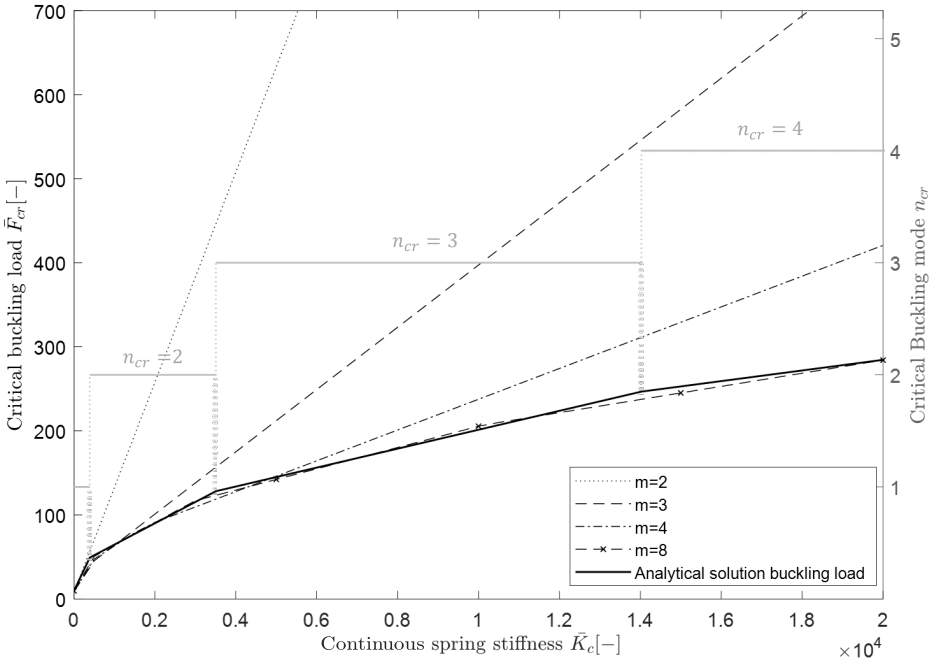

Figure 2.4: Validation of the numerical linear buckling model for various numbers of discrete element approximations.

The influence of the number of discrete elements on the approximation of the bifurcation load is further analysed for $\overline{K_c} = 0$, see Figure 2.5. In Figure 2.5a the number discrete elements used for the model, in this case varying form 2 up to 18, is plotted versus the obtained bifurcation loads. The results are plotted for four considered boundary conditions, as indicated by their abbreviations. The horizontal lines show the corresponding analytical values of the buckling loads.
It is observed that with increasing number of applied elements, the approximation of the buckling load becomes more accurate. However, the convergence towards the analytical solution differs for each boundary condition.
This effect can be observed more clearly in Figure 2.5b in which the relative error between the discrete approximation of the bifurcation load and the analytical buckling load is plotted against the number of discrete elements. The approximation with the discrete element model for the simply supported (pinned-pinned) system is substantially more accurate than the approximation of a fibre clamped on both sides with the same number of discrete elements. This property of the created MATLAB model can, however, be easily explained since an approximation for the rotational spring stiffness is adopted in which no difference between the multiple boundary conditions has been made. For clamped connections, an additional rotational spring is added in the mechanical discrete model of the fibre of which the spring stiffness is set equal to the derived discrete bending stiffness of the fibre, which is obviously not an accurate approximation for the clamped behaviour. This is, however, inherent to the applied discretization method and it is therefore expected that models with boundary conditions with one or more clamped connections, will have a less accurate approximation than the model for a simply supported fibre. To improve the approximation for systems with clamped behaviour, an alternatively calculated spring stiffness representing the inclination may be calculated using the beam theory.

2.2.5 Non-linear buckling analysis

Critical bifurcation loads and buckling modes of the stability loss of an elastically embedded fibre can be determined using stationarity principles and linearised equations. However, the homogeneous linearised equations of the elastic stability theory cannot give any information on the type of bifurcation or the behaviour of the system after stability loss. Therefore, a non-linear buckling analysis is required to study the influence of imperfections, non-linear matrix and non-linear fibre properties on the buckling and post-buckling behaviour of an embedded fibre (Alfutov, 2011).
One effective numerical method for solving the set of non-linear equations resulting from 2.8b or 2.17 is the Newton-Raphson iterative method. In this most commonly used incremental-iterative procedure, the equilibrium path is constructed by increments of a certain control parameter and subsequent iterations to restore equilibrium. The Newton-Raphson scheme is elaborated indepen-

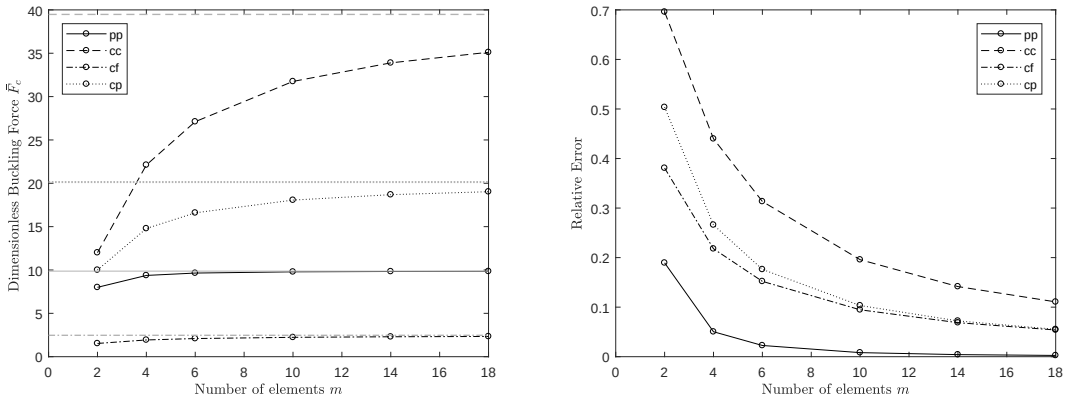

(a) (b)

Figure 2.5: Obtained bifurcation loads versus the number of discrete elements used for the linear DEM analysis including the corresponding analytical solutions (a) and the corresponding relative errors with respect to the analytically obtained bifurcation load (b).

dently from the incremental control strategy in Section 2.2.5.1. In Sections 2.2.5.2 and 2.2.5.3, the adopted incremental control strategies, Load control and Arc-length control respectively, are elaborated. Finally, the programmed non-linear DEM buckling model is validated using existing Finite Element Method (FEM) software.

2.2.5.1 Newton-Raphson iterative method

The Newton-Raphson iterative method involves the repeated linearisation of the non-linear equations as it breaks down the equilibrium path into a series of simpler piecewise linear steps (Holtzer, 2017). An initial trial solution for an equilibrium point on the load-displacement curve is guessed, which is then gradually improved by using the slope of the load-displacement curve. The slope may be updated at each iteration, or kept constant for sequential iterations and be only updated for each increment, referred to as the full and modified Newton-Raphson, respectively. A residual is calculated at each iteration i reflecting the discrepancy between the actual solution of the system of equations and the current 'guessed' solution. In general, the set of algebraic non-linear equations to be satisfied for equilibrium is given by

$$\boldsymbol{\Psi}(\mathbf{d}) = \mathbf{f} - \mathbf{P}(\mathbf{d}) = \mathbf{0}, \tag{2.18}$$

where $\mathbf{d}$ are the degrees of freedom of the system, $\mathbf{f}$ is a vector independent of the degrees of freedom (dof's) and $\mathbf{P}$ a vector dependent on the dof's. In the present work, the dof's are represented by the nodal rotations $\boldsymbol{\phi}$ & $\mathbf{f}$ and $\mathbf{P}$ are the actual solution for stationarity of the total potential energy of the system (stating equilibrium), i.e. $\mathbf{0}$, and the current solution for the first variation of the potential energy $\delta V(\boldsymbol{\phi})$, respectively. The resulting equation for the residual vector is then found to be

$$\mathbf{R}(\boldsymbol{\phi}) = \mathbf{0} - \frac{\partial V}{\partial \boldsymbol{\phi}} = -\frac{\partial V}{\partial \boldsymbol{\phi}}. \tag{2.19}$$

A converged solution on the equilibrium path is found when the non-linear system of equations $\mathbf{R}(\boldsymbol{\phi}) = \mathbf{0}$ is satisfied within a specified tolerance. The convergence criterium in the present work is defined as the norm of $\mathbf{R}$, i.e. the square root of the scalar product of the residual vector and calculated by

$$R_{tol} = \sqrt{\mathbf{R} \cdot \mathbf{R}} = \sqrt{\sum_{k=1}^{m} \left(-\frac{\partial V}{\partial \phi_k} \right)^2}. \tag{2.20}$$

To follow the incremental-iterative procedure of the Newton-Raphson method, assume that the last converged solution on the equilibrium path of the structure is found at increment t. The next incremental solution is then found at increment $t+1$ and is accepted when $(R_{tol})_{t+1}$ is equal to or lower than a predefined convergence tolerance. Hence the solution has to satisfy, within this specified tolerance, the non-linear system of equations

$$\mathbf{R}_{t+1}(\boldsymbol{\phi}_{t+1}) = -\frac{\partial V(\boldsymbol{\phi}_{t+1})}{\partial \boldsymbol{\phi}} = \mathbf{0}. \tag{2.21}$$

To obtain the next solution satisfying Eq. 2.21, a sequence of iterations i is generated to improve an initially guessed next equilibrium solution. The residual of the next iteration $i+1$ is found by linearisation about the last iteration i of Eq. 2.21 using a first order Taylor series expansion

$$\mathbf{R}^{i+1}_{t+1}(\boldsymbol{\phi}^{i+1}_{t+1}) = \mathbf{R}^{i}_{t+1}(\boldsymbol{\phi}^{i}_{t+1}) + \left(\frac{\partial R}{\partial \boldsymbol{\phi}} \right)^{i}_{t+1} \delta \boldsymbol{\phi}^{i+1}_{t+1}, \tag{2.22}$$

with the assembled tangential stiffness matrix $\mathbf{K}^{i}_{t+1} = \left(\frac{\partial R}{\partial \boldsymbol{\phi}} \right)^{i}_{t+1}$ and the iterative correction for the rotations $\delta \boldsymbol{\phi}^{i+1}_{t+1} = \boldsymbol{\phi}^{i+1}_{t+1} - \boldsymbol{\phi}^{i}_{t+1}$.
Inverting Eq. 2.22 turns the nodal rotation iterative correction to

$$\delta \boldsymbol{\phi}^{i+1}_{t+1} = -\left(\mathbf{K}^{i}_{t+1} \right)^{-1} \mathbf{R}^{i}_{t+1}(\boldsymbol{\phi}^{i}_{t+1}). \tag{2.23}$$

The residual vector is then recalculated with the newly found rotations $\boldsymbol{\phi}_{t+1}^{i+1} = \boldsymbol{\phi}_t + \Delta\boldsymbol{\phi}_{t+1}^{i+1}$ in which the corrected incremental step size equals

$$\Delta\boldsymbol{\phi}_{t+1}^{i+1} = \Delta\boldsymbol{\phi}_{t+1}^{i} + \delta\boldsymbol{\phi}_{t+1}^{i+1} = \sum_{k=1}^{i+1} \delta\boldsymbol{\phi}_{t+1}^{k}. \tag{2.24}$$

The total residual is checked for satisfaction of the convergence criterium, and as long as R_{tol} exceeds the predefined tolerance, the iterative procedure is continued. If convergence is reached, the search for the next incremental is solution is started based on the applied incremental control strategy (Suiker, Askes, & Sluys, n.d.). In the present work, either a load controlled or arc length controlled strategy is adopted.

2.2.5.2 Load controlled method

The load controlled incremental strategy is the most commonly applied strategy in which the externally applied load is prescribed at the beginning of each increment and the corresponding rotations are searched using the iterative procedure as previously described. Throughout the iterative process, the load is held constant, resulting in a horizontal line as the constraint surface of possible solutions in the load-displacement diagram, see the graphical interpretation in Figure 2.6a.
The load incremental scheme is widely implemented in commercial Finite Element software due to its fast (quadratic) convergence rate. However, the incremental strategy fails to follow the equilibrium path once the tangent stiffness reaches zero under snap-through behaviour, due to its horizontally constraint solution space. Alternative control strategies are required to overcome those limit points with zero tangent stiffness. A displacement controlled incremental strategy may be adopted. Analogous to load control, a displacement component is fixed as the control parameter to trace the equilibrium path. However, in a similar manner, this strategy is unable to follow the equilibrium path at limit points in displacement under snap-back behaviour, since the constraint surface of the incremental strategy is a vertical line in the load displacement curve.

2.2.5.3 Arc length method

Arc length control is a robust control strategy that is able to overcome both limit points in force and displacement. The strategy is a path-following method that considers simultaneously variation in both the load parameter λ and displacement variables $\boldsymbol{\phi}$ during an increment. Hence both are

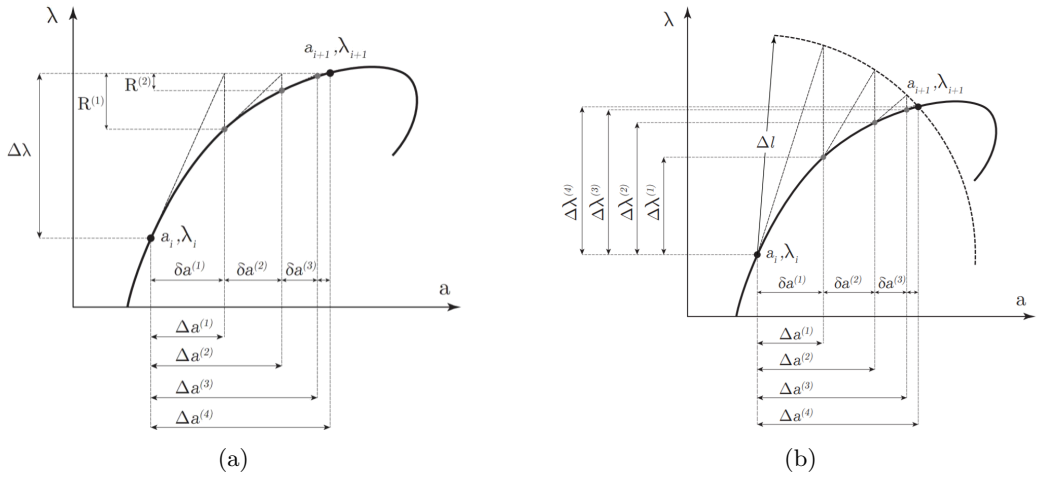

Figure 2.6: Graphical interpretation of the incremental control strategies (a) load controlled and (b) arc length controlled. The displacement parameter is denoted by a and λ represents the load incrementation parameter. δ and Δ refer to the iterative correction and to the updated incremental step size respectively (Vasios, 2015).

considered as unknowns, in contrast to the load control strategy where λ is prefixed during an increment and the problem was iteratively solved for $\boldsymbol{\phi}$. The supplementary equation $C(\Delta\boldsymbol{\phi}, \Delta\lambda)$ to complete the system constraints the solution space to an arc length Δl, as indicated in Figure 2.6b, and is referred to as the arc length equation. With the additional variable and constraint equation, the original system of equations 2.21 is extended to

$$\begin{aligned} \mathbf{R}_{t+1}(\boldsymbol{\phi}_{t+1}, \lambda_{t+1}) &= -\left(\frac{\partial V(\boldsymbol{\phi}_{t+1}), \lambda_{t+1}}{\partial \boldsymbol{\phi}} + \frac{\partial V(\boldsymbol{\phi}_{t+1}), \lambda_{t+1}}{\partial \lambda}\right) = \mathbf{0}, \\ C(\Delta\boldsymbol{\phi}, \Delta\lambda) &= 0. \end{aligned} \tag{2.25}$$

The system of equations is linearised about the last iteration $(\boldsymbol{\phi}^i_{t+1}, \lambda^i_{t+1})$ using a first order Taylor series expansion to obtain

$$\begin{aligned} \mathbf{R}^{i+1}_{t+1}(\boldsymbol{\phi}^{i+1}_{t+1}, \lambda^{i+1}_{t+1}) &= \mathbf{R}^i_{t+1}(\boldsymbol{\phi}^i_{t+1}, \lambda^i_{t+1}) + \left(\frac{\partial R}{\partial \boldsymbol{\phi}}\right)^i_{t+1} \delta\boldsymbol{\phi}^{i+1}_{t+1} + \left(\frac{\partial R}{\partial \lambda}\right)^i_{t+1} \delta\lambda^{i+1}_{t+1}, \\ C^{i+1}_{t+1}(\boldsymbol{\phi}^{i+1}_{t+1}, \lambda^{i+1}_{t+1}) &= C^i_{t+1}(\boldsymbol{\phi}^i_{t+1}, \lambda^i_{t+1}) + \left(\frac{\partial C}{\partial \boldsymbol{\phi}}\right)^i_{t+1} \delta\boldsymbol{\phi}^{i+1}_{t+1} + \left(\frac{\partial C}{\partial \lambda}\right)^i_{t+1} \delta\lambda^{i+1}_{t+1}, \end{aligned} \tag{2.26}$$

with the assembled tangential stiffness matrix $\mathbf{K}^i_{t+1} = \left(\frac{\partial R}{\partial \boldsymbol{\phi}}\right)^i_{t+1}$, the iterative correction for the rotations and load parameter defined as $\delta\boldsymbol{\phi}^{i+1}_{t+1} = \boldsymbol{\phi}^{i+1}_{t+1} - \boldsymbol{\phi}^i_{t+1}$ and $\delta\lambda^{i+1}_{t+1} = \lambda^{i+1}_{t+1} - \lambda^i_{t+1}$ and partial derivative $\mathbf{f_{ext}}^i_{t+1} = \left(\frac{\partial R}{\partial \lambda}\right)^i_{t+1}$.
The linearised system in Eq. 2.26 can be rewritten in matrix-vector format to find

$$\begin{bmatrix} -\mathbf{K}^i_{t+1} & -\mathbf{f_{ext}}^i_{t+1} \\ \frac{\partial C}{\partial \boldsymbol{\phi}} & \frac{\partial C}{\partial \lambda} \end{bmatrix} \begin{bmatrix} \delta\boldsymbol{\phi}^{i+1}_{t+1} \\ \delta\lambda^{i+1}_{t+1} \end{bmatrix} = \begin{bmatrix} \mathbf{R}^i_{t+1} \\ -C^{i+1}_{t+1} \end{bmatrix}, \tag{2.27}$$

which is an augmented version of the equations found in Section 2.2.5.1. The disadvantage of this augmented version is that the matrix in Eq. 2.27, that should be inverted to calculate the new iterative corrections of the rotations and load parameter, lost the symmetric and banded structure the tangent stiffness matrix in Eq. 2.22 and 2.23 does have. Computationally, solving this system with a traditional method would be undesirable with respect to both storage and efficiency. Batoz and Dhatt (1979) presented a technique to overcome this disadvantage by splitting the iterative displacement vector into two components (Fafard & Massicotte, 1993; Holtzer, 2017). An uncoupled system of equations is obtained as

$$\delta\boldsymbol{\phi}^{i+1}_{t+1} = \left(\delta\boldsymbol{\phi}^{i+1}_{t+1}\right)^{res} + \delta\lambda^{i+1}_{t+1} \left(\delta\boldsymbol{\phi}^{i+1}_{t+1}\right)^{ext}, \tag{2.28}$$

in which the two displacement components can be calculated by solving the two systems of equations

$$-\mathbf{K}^i_{t+1} \left(\delta\boldsymbol{\phi}^{i+1}_{t+1}\right)^{res} = \mathbf{R}^i_{t+1} \qquad \mathbf{K}^i_{t+1} \left(\delta\boldsymbol{\phi}^{i+1}_{t+1}\right)^{ext} = \mathbf{f_{ext}}^i_{t+1}. \tag{2.29}$$

The solution is found by inverting both equations in 2.29, resulting in

$$\left(\delta\boldsymbol{\phi}^{i+1}_{t+1}\right)^{res} = -\left(\mathbf{K}^i_{t+1}\right)^{-1} \mathbf{R}^i_{t+1} \qquad \left(\delta\boldsymbol{\phi}^{i+1}_{t+1}\right)^{ext} = \left(\mathbf{f_{ext}}^i_{t+1}\right)^{-1} \mathbf{R}^i_{t+1}. \tag{2.30}$$

The stiffness matrix $\mathbf{K}^i_{t+1}$ is now the same as used for the other incremental control strategies. It is used for the calculation of both (partial) iterative displacement corrections yet only needs to be inverted once. Moreover, the symmetric and banded properties are retained.
To compute the total iterative displacement correction with Eq. 2.28, the iterative load parameter $\delta\lambda^{i+1}_{t+1}$ is required. To obtain $\delta\lambda^{i+1}_{t+1}$, Chrisfield's method (Crisfield, 1981; Vasios, 2015; Holtzer, 2017; Fafard & Massicotte, 1993; Ritto-Corrêa & Camotim, 2008) is adopted in combination with the quadratic constraint equation $C(\Delta\boldsymbol{\phi}, \Delta\lambda)$, i.e. the arc length equation

$$C(\Delta\boldsymbol{\phi}, \Delta\lambda) = \left(\Delta\boldsymbol{\phi}^{i+1}_{t+1}\right)^{\mathrm{T}} \Delta\boldsymbol{\phi}^{i+1}_{t+1} + \beta^2 \left(\Delta\lambda^{i+1}_{t+1}\right)^2 - \Delta l^2 = 0, \tag{2.31}$$

in which $\boldsymbol{\phi}_{t+1}^{i+1} = \boldsymbol{\phi}_t + \Delta\boldsymbol{\phi}_{t+1}^{i+1}$ and $\Delta\lambda_{t+1}^{i+1} = \lambda_t + \Delta\lambda_{t+1}^{i+1}$, see also Eq. 2.24.
Using the the computed partial iterative displacement corrections, $\left(\delta\boldsymbol{\phi}_{t+1}^{i+1}\right)^{res}$ and $\left(\delta\boldsymbol{\phi}_{t+1}^{i+1}\right)^{ext}$, substitution in 2.31 leads to the quadratic equation in $\delta\lambda_{t+1}^{i+1}$

$$a\delta\left(\lambda_{t+1}^{i+1}\right)^2 + b\delta\lambda_{t+1}^{i+1} + c = 0, \tag{2.32}$$

where

$$\begin{aligned} a &= \left(\delta\boldsymbol{\phi}_{t+1}^{i+1}\right)^{ext} \cdot \left(\delta\boldsymbol{\phi}_{t+1}^{i+1}\right)^{ext} + \psi^2, \\ b &= 2\left(\Delta\boldsymbol{\phi}_{t+1}^{i} + \left(\delta\boldsymbol{\phi}_{t+1}^{i+1}\right)^{res}\right)^T \left(\delta\boldsymbol{\phi}_{t+1}^{i+1}\right)^{ext} + 2\psi^2\Delta\lambda_{t+1}^{i}, \\ c &= \left(\Delta\boldsymbol{\phi}_{t+1}^{i} + \left(\delta\boldsymbol{\phi}_{t+1}^{i+1}\right)^{res}\right)^T \left(\Delta\boldsymbol{\phi}_{t+1}^{i} + \left(\delta\boldsymbol{\phi}_{t+1}^{i+1}\right)^{res}\right) + \psi^2\Delta\lambda_{t+1}^{i} - \Delta l^2. \end{aligned} \tag{2.33}$$

At the start of each increment, i.e. $i = 0$, $\Delta\boldsymbol{\phi}_{t+1}^{i} = 0$, $\Delta\lambda_{t+1}^{i} = 0$ and $\left(\delta\boldsymbol{\phi}_{t+1}^{i+1}\right)^{res} = 0$, resulting in $b = 0$ and the solution of Eq. 2.32 to equal the upper part of Eq. 2.34.
For subsequent iterative corrections, i.e. at $i \leq 1$ the quadratic equation in 2.32 has two roots, as obviously follows from the two intersections the circular constraint surface has with the equilibrium path of the system. For these subsequent iterations, the load parameter equals the lower part of Eq. 2.34.

$$\delta\lambda_{t+1}^{i+1} = \begin{cases} \delta\lambda_{t+1}^{i+1} = \pm\frac{\Delta l}{\sqrt{\left(\delta\boldsymbol{\phi}_{t+1}^{i+1}\right)^{ext}\cdot\left(\delta\boldsymbol{\phi}_{t+1}^{i+1}\right)^{ext}+\psi^2}} & \text{for } i = 0 \\ \delta\lambda_{t+1}^{i+1} = -\frac{b}{2a} \pm \sqrt{\left(\frac{b}{2a}\right)^2 - \frac{c}{a}} = \begin{cases} \left(\delta\lambda_{t+1}^{i+1}\right)_1 \\ \left(\delta\lambda_{t+1}^{i+1}\right)_2 \end{cases} & \text{for } i \geq 1 \end{cases} \tag{2.34}$$

The sign of the load parameter in Eq. 2.34 during the first iteration ($i = 0$) is positive in the first incremental load step, i.e. $t = 0$, and afterwards ($t \geq 1$) is chosen on the basis of the previous increment, while it should be positive for loading and negative for unloading. Following Crisfield (1981) & Ritto-Corrêa and Camotim (2008), the solution is taken positive if $\left(\delta\boldsymbol{\phi}_{t+1}^{i+1}\right)^{ext} \cdot \Delta\boldsymbol{\phi}_{t+1}^{i} + \psi^2\Delta\lambda_{t+1}^{i} \geq 0$ and negative otherwise.
The sign of the load parameter in Eq. 2.34 during subsequent iterations ($i \geq 0$) is chosen so that the root corresponds to a solution closest to the one obtained in the last iteration. This proximity is assessed by the dot product $D = \Delta\boldsymbol{\phi}_{t+1}^{i} \cdot \left(\delta\boldsymbol{\phi}_{t+1}^{i+1}\right)^{ext} + \psi^2\Delta\lambda_{t+1}^{i}$, which should be maximised. Hence, the load parameter $\delta\lambda_{t+1}^{i+1}$ for $i \geq 1$ is consequently chosen as

$$\delta\lambda_{t+1}^{i+1} = \begin{cases} \left(\delta\lambda_{t+1}^{i+1}\right)_1 & \text{if } D\cdot\left(\delta\lambda_{t+1}^{i+1}\right)_1 > D\cdot\left(\delta\lambda_{t+1}^{i+1}\right)_2 \\ \left(\delta\lambda_{t+1}^{i+1}\right)_2 & \text{otherwise} \end{cases} \tag{2.35}$$

This root selection procedure using Eq. 2.35 prevents the equilibrium path to double back on itself. In other words, it prevents the obtained solutions from moving back on the equilibrium path, but instead forces them to evolve forwards.

Although the aforementioned root selection procedures are adopted in an effort to force the solution to evolve forwards on the equilibrium path, it may occur that convergence issues still arise at limit points with sharp turns in the path. To increase the robustness of the implemented arc length method, several additional strategies are implemented and shortly outlined below.
It may occur that the load parameters obtained with Eq. 2.34 for the subsequent iterations ($i \geq 0$) have complex values. Real values are obtained when the condition $b^2 - 4ac > 0$ is met. In the case this condition is not met, the usual practice is to decrease the applied incremental arc length Δl, for example by halving it. However, another strategy may be adopted in which partial corrections are applied, making it possible to find real roots for Eq. 2.32 even when this condition is not met. In this procedure, as originally proposed by Z. Zhou and Murray (1995), the non-dimensional quantity Δs is introduced as the applied fraction of the 'ideal' correction $\left(\delta\boldsymbol{\phi}_{t+1}^{i+1}\right)^{res}$, with Δs

ranging between $0 < \Delta s \leq 1$. Following Ritto-Corrêa and Camotim (2008) in their implementation of the technique, Eq. 2.28 is then changed into

$$\delta\boldsymbol{\phi}_{t+1}^{i+1} = \Delta s \left(\delta\boldsymbol{\phi}_{t+1}^{i+1}\right)^{res} + \delta\lambda_{t+1}^{i+1} \left(\delta\boldsymbol{\phi}_{t+1}^{i+1}\right)^{ext}. \tag{2.36}$$

The value for the partial correction Δs preferably equals $\Delta s = 1$ from a Newton-Raphson point of view. However, when complex roots prevent that the linearised equilibrium solution intersects with the constraint surface of the arc length control strategy, the partial correction is chosen as the maximum value of Δs for which this condition does satisfy, which is given by

$$\Delta s_{max} = -\frac{b_s}{2a_s} + \sqrt{\left(\frac{b_s}{2a_s}\right)^2 - \frac{c_s}{a_s}}, \tag{2.37}$$

with

$$\begin{aligned} a_s &= b_1^2 - 4a_0c_2, \\ b_s &= 2b_0b_1 - 4a_0c_1, \\ c_s &= b_0^2 - 4a_0c_0, \end{aligned} \tag{2.38}$$

and

$$\begin{aligned} a_0 &= \left(\delta\boldsymbol{\phi}_{t+1}^{i+1}\right)^{ext} \cdot \left(\delta\boldsymbol{\phi}_{t+1}^{i+1}\right)^{ext} + \psi^2, \\ b_0 &= 2\left(\delta\boldsymbol{\phi}_{t+1}^{i+1}\right)^{ext} \cdot \Delta\boldsymbol{\phi}_{t+1}^{i} + 2\psi^2\Delta\lambda_{t+1}^{i}, \\ b_1 &= 2\left(\delta\boldsymbol{\phi}_{t+1}^{i+1}\right)^{ext} \cdot \left(\delta\boldsymbol{\phi}_{t+1}^{i+1}\right)^{res}, \\ c_0 &= \Delta\boldsymbol{\phi}_{t+1}^{i} \cdot \Delta\boldsymbol{\phi}_{t+1}^{i} + \psi^2\Delta\lambda_{t+1}^{i} - \Delta l^2, \\ c_1 &= 2\left(\delta\boldsymbol{\phi}_{t+1}^{i+1}\right)^{res} \cdot \Delta\boldsymbol{\phi}_{t+1}^{i}, \\ c_2 &= \left(\delta\boldsymbol{\phi}_{t+1}^{i+1}\right)^{res} \cdot \left(\delta\boldsymbol{\phi}_{t+1}^{i+1}\right)^{res}. \end{aligned} \tag{2.39}$$

Due to the application of partial corrections, the iterative process may eventually converge, eliminating the need to cut the incremental step length (Δl) and reducing the net computational effort.

At last, the robustness of the arc length method is increased by the automatic updating of the applied arc length increment Δl. The updated arc length increment Δl_{t+1} is chosen by an algorithm based on the desired number of iteration per increment N_{des} as defined by the user. The updated arc length increment is then found to be

$$\Delta l_{t+1} = \Delta l_t \left(\frac{N_{des}}{N_t}\right)^{0.5}, \tag{2.40}$$

where N_t equals the number of iterations needed for convergence in the previous increment.

A non-linear buckling analysis for an individual simply supported embedded fibre using the arc length method and additional strategies for robustness, is provided in appendix A.

2.2.5.4 Validation

A parametric MATLAB code using the method as described in the previous sections, is created for the non-linear buckling analysis of an individual embedded fibre. The results of this numerical model are validated using the analytical solution obtained in Section 2.1, and a FEM model constructed with Abaqus, see Figure 2.7.
It is observed that the results for both the Discrete Element Method models and the Finite Element Method model approximate the analytical solution as obtained in Section 2.1. As expected, the FEM model provides an overestimation of the analytically obtained bifurcation load. On the contrary, the DEM models approximate the analytical solution from below. For 100 elements, the results of the DEM model and the FEM model coincide and therefore, the solutions are assumed to be converged. It is observed that while using less elements, the relative error of solutions obtained with the DEM model is smaller than the relative error obtained with the FEM model. Thus for low

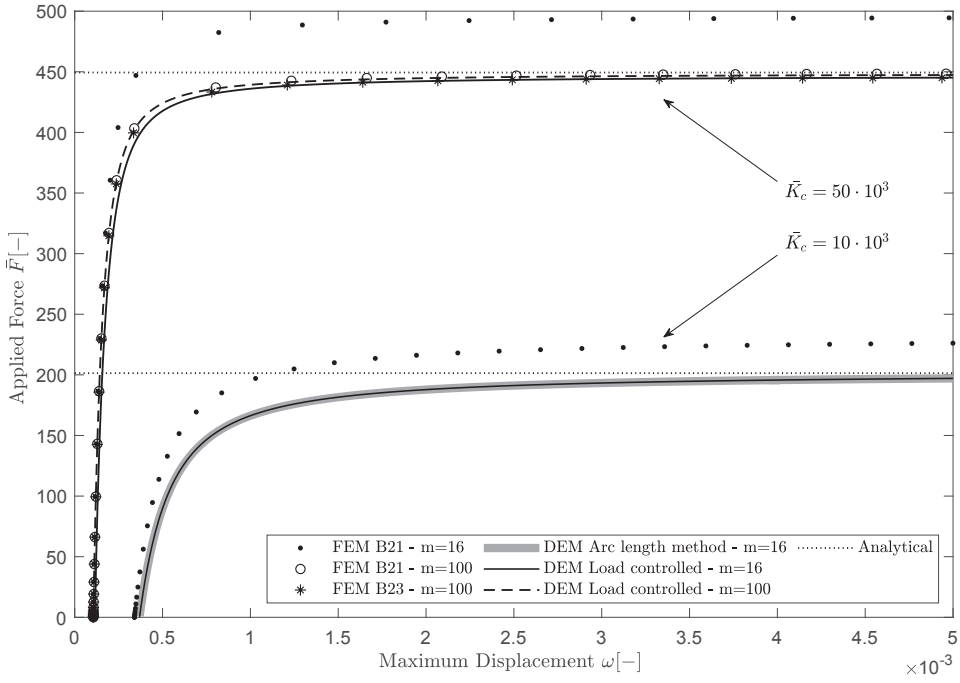

Figure 2.7: Validation of the numerical non-linear buckling model for two values of the matrix stiffness. The results of the DEM model with Newton-Raphson incremental-iterative scheme are shown for both a load controlled and arc-length incremental strategy.

number of elements, a more accurate approximation of the buckling behaviour may be obtained using the DEM model, since a faster mesh convergence rate is shown for these models. This can however be explained by the modelling process of the matrix influence. For both the FEM and DEM model, the influence of the matrix is modelled by linearly elastic discrete springs applied at the nodes between elements. In the DEM model, all degrees of freedom of the system are localised at these nodes, however, in the FEM model, a n-th order polynomial displacement function is applied over the elements. (In Figure 2.7 a first or third order function is used for B21 or B23 elements, respectively.) It is expected that the absence of matrix support over the elements in the FEM model, results in a less accurate approximation of the bifurcation load. By increasing the amount of elements, the influence of the matrix support is distributed more evenly over the beam length and the FEM approximation is indeed improved. However it may be concluded that this modelling process has less influence on the accuracy of the approximation with the Discrete Element Method. The influence of this modelling process on the FEM approximation increases for increasing matrix moduli.

Lastly, it is observed that the obtained solution and approximation of the buckling load is independent of the incremental strategy used. That is, the solutions of the force controlled incremental approach and arc length method coincide with each other The arc length method however, tends to be more sensitive for user-defined simulation parameters.

3 Individual embedded fibres

The programmed numerical Discrete Element Method (DEM) model is used to analyse the buckling behaviour of individual fibres embedded in a matrix. The non-linear model has been adopted for the analysis and parameter study performed in the current chapter.
From the analytical solution given by Eq. 2.6 in Section 2.1 it is concluded that the critical buckling load of an individual embedded fibre is solely subjected to the stiffness of the surrounding matrix. The foundation modulus, or continuous spring stiffness, characterises the interaction between the fibre and the matrix and its quantitative relation to the composite properties is evaluated in Section 3.1. Two approaches for establishing this quantitative relation are elaborated and compared. A parameter range is set based on common fibre reinforced composite constituents and properties and the non-linear DEM model is used to analyse the behaviour of a single fibre subjected to axial compressive loading. Additionally, resistance due to friction on the fibre-matrix interface is considered in Section 3.1.2.
In sections 3.2 and 3.3 the influence of non-linear matrix behaviour on the buckling of individual fibres is analysed by modelling bilinear matrix stiffness and damage behaviour.

3.1 Influence of the matrix

When subjected to compressive loading, fibres embedded in a matrix can sustain considerably higher compressive loads than unembedded fibres. The surrounding matrix provides support against buckling in radial or, when considered in 2D, lateral direction. Moreover, due to friction on the fibre-matrix interface, resistance is offered against vertical displacement of the fibre with respect to the matrix itself. Both effects are quantitatively examined in Section 3.1.1 and 3.1.2, respectively.

3.1.1 Evaluation of the matrix foundation modulus

The relation between theoretical analysis and experimental results can be made more quantitative by exploring the relation of the continuous spring stiffness K_c with respect to material properties. Several approaches may be adopted, of which two are considered in the present work.
The foundation modulus is approximated by the Young's Modulus of the matrix E_m in the first approach. The dimensionless continuous spring stiffness in the analytical model, can then be found as

$$\overline{K}_c = \frac{E_m L_f^4}{E_f I_f}. \tag{3.1}$$

Substitution of the second moment of area for circular fibre sections $I = \frac{1}{4}\pi r^4$, yields

$$\overline{\mathrm{K}}_c = \frac{4}{\pi}\frac{E_m}{E_f}\left(\frac{L_f}{r}\right)^4. \tag{3.2}$$

By adopting the Winkler foundation model, the matrix is simplified as an array of springs with discrete spring stiffness k $[N/mm]$ acting in lateral direction. Hence, the dimensionless discrete spring stiffness is computed as $\overline{k} = \frac{\overline{K}_c}{m}$ in which m is the number of discrete elements used for the numerical analysis.
For the second approach, the foundation modulus is approximated following the work of Su et al. (2014) based on the derivation of the continuous spring stiffness by Lanir and Fung (1972) and Herrmann, Mason, and Chan (1967). The support of the matrix is considered to be proportional to the deflection due to lateral displacement of the fibre. The displacement field of an infinite, unbounded elastic medium subjected to a concentrated force can be obtained from the integration of Kelvin's solution. The continuous spring stiffness is then approximated as

$$K = \frac{16\pi G_m (1-\nu_m)}{2(3-4\nu_m) K_0(n\pi r_f/L_f) + n\pi r_f K_1(n\pi r_f/L_f)/L_f}, \tag{3.3}$$

with shear modulus $G_m = E_m/(2(1+\nu_m))$, Young's modulus E_m and Poisson's ratio ν_m of the matrix, radius r_f and length L_f of the fibre, n the critical buckling mode of the embedded fibre

and K_0 and K_1 are modified Bessel functions of the second kind (Su et al., 2014; Lanir & Fung, 1972; Zhao, Li, Cao, & Feng, 2016). For slender fibres, i.e. for which $r_f/L_f \to 0$, Eq. 3.3 can be significantly simplified to

$$\mathrm{K_c} \approx \frac{8\pi G_m \left(1-\nu_m\right)}{\ln\left(\frac{2L_f}{nr_f}\right)}, \tag{3.4}$$

which by substituting $G_m = E_m/\left(2\left(1+\nu_m\right)\right)$ and dividing through $E_f I_f/L_f^4$ may be presented in dimensionless form as

$$\overline{K}_c \approx \frac{8\pi E_m \frac{(1-\nu_m)}{2(1+\nu_m)}}{\ln\left(\frac{2L_f}{nr_f}\right)} \frac{L_f^4}{E_f I_f} \approx 32 \frac{\frac{(1-\nu_m)}{2(1+\nu_m)}}{\ln\left(\frac{2L_f}{nr_f}\right)} \frac{E_m}{E_f} \left(\frac{L_f}{r}\right)^4. \tag{3.5}$$

From Eq. 3.5 it is concluded that for the approach following Su et al., the foundation modulus depends on both matrix and fibre properties. Moreover, K_c depends on the critical buckling mode of the embedded fibre n.

From Section 2.1.2 one recalls that the critical buckling force of an individual fibre embedded in a matrix can be found upon calculation of the mode number that minimises $\overline{F}_n$, i.e. by solving $\frac{\partial \overline{F}_n}{\partial n} = 0$. A non-linear relation between the governing buckling mode and the foundation modulus is obtained as

$$\overline{F}_n = n^2\pi^2 + \frac{\overline{\mathrm{K}}_c}{n^2\pi^2} \quad \text{where } n = 1, 2, 3, \ldots, \tag{3.6a}$$

$$\partial \overline{F}/\partial n = 0 \qquad \rightarrow \qquad n_{cr} = \sqrt[4]{\frac{\overline{K}_c}{\pi^4}}. \tag{3.6b}$$

To compute the value for $\overline{K}_c$, the non-linear relation in 3.6b is solved using a Newton-Raphson solution procedure in which the residual, out of balance term is calculated as

$$R = n^4 - \frac{32}{\pi^4} \frac{\frac{(1-\nu_m)}{2(1+\nu_m)}}{\ln\left(\frac{2L_f}{nr_f}\right)} \frac{E_m}{E_f} \left(\frac{L_f}{r}\right)^4. \tag{3.7}$$

Comparing both approximations,

$$\overline{\mathrm{K}}_c = \frac{4}{\pi} \frac{E_m}{E_f} \left(\frac{L_f}{r}\right)^4, \qquad \overline{K}_{cSu} \approx 32 \frac{\frac{(1-\nu_m)}{2(1+\nu_m)}}{\ln\left(\frac{2L_f}{nr_f}\right)} \frac{E_m}{E_f} \left(\frac{L_f}{r_f}\right)^4,$$

the Matrix-Fibre stiffness ratio $\frac{E_m}{E_f}$ and Fibre aspect ratio $\frac{L_f}{r_f}$ are identified as physical and geometrical parameters influencing the dimensionless foundation modulus of the matrix, respectively. For common fibre reinforced composites, the values for those ratios range between $10^{-5} \leq \frac{E_m}{E_f} \leq 1$ and $50 \leq \frac{L_f}{r_f} \leq 1000$. Hence, the value for the dimensionless foundation modulus is found to range between $10^2 \lesssim \overline{K}_c \lesssim 10^{12}$.

Within these ranges, the approximations of $\overline{K}_c$ using the Young's modulus approach and the approach as proposed by Su et al. (2014) are compared in Figures 3.1 up to 3.7.

In Figure 3.1 the value for the continuous spring stiffness of the matrix for both approximations is plotted versus the matrix-fibre stiffness ratio for three different fibre aspect ratios. An increasing spring stiffness is observed for an increasing ratio E_m/E_f. If the Young's modulus of the fibre is assumed to be fixed, this effect can be directly assigned to the increase in Young's modulus of the matrix. As follows from both equations and is observed in Figure 3.2, the value for the continuous spring stiffness is linearly dependent of the matrix-fibre stiffness ratio. With the value for the dimensionless spring constant known, the critical buckling load $\overline{F}_c$ can be determined and its value is plotted versus the matrix-fibre stiffness ratio for both approximation methods for $\overline{K}_c$ in Figure 3.3. It is observed that for increasing E_m, the critical buckling force is increasing. Additionally, it can be seen that for higher fibre aspect ratios, i.e. for more slender fibres, a higher dimensionless critical buckling force is obtained. This counter-intuitive result is, however, caused by the specific dimensionless formulation of the force, as is confirmed in Figure 3.4, in which the critical buckling force is given in Newton.

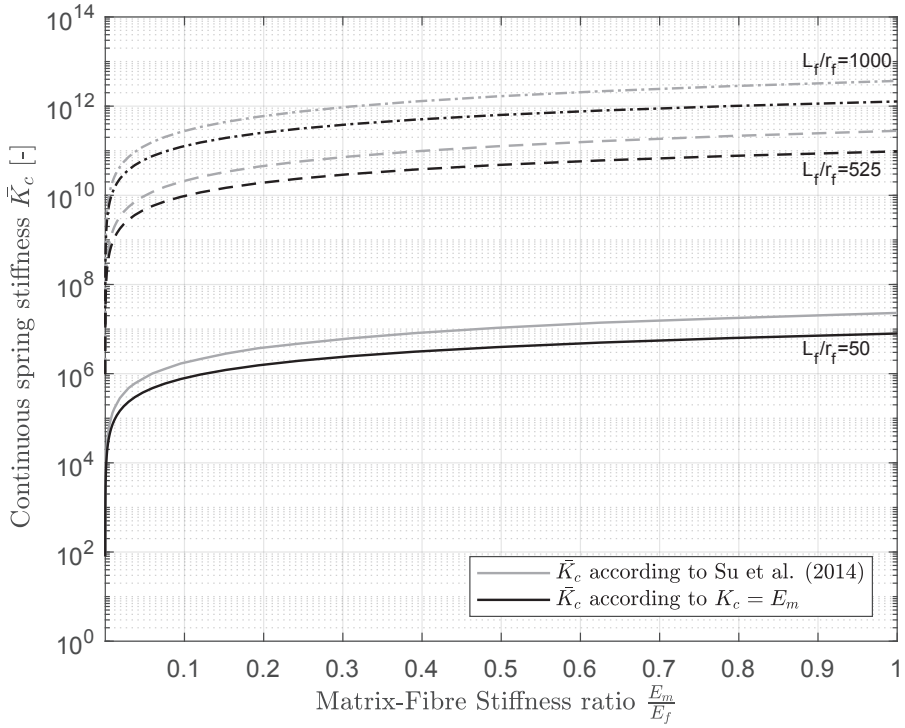

Figure 3.1: The continuous spring stiffness representing the matix versus the Matrix-Fibre stiffness ratio, plotted for three values of $\frac{L_f}{r_f}$.

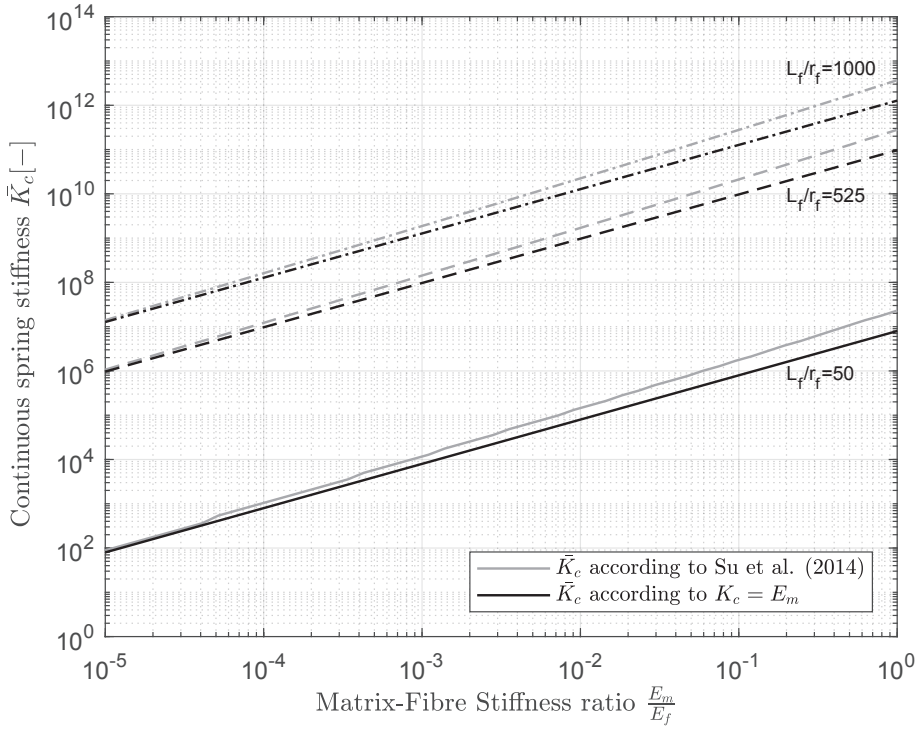

Figure 3.2: The continuous spring stiffness representing the matix versus the Matrix-Fibre stiffness ratio, plotted for three values of $\frac{L_f}{r_f}$ on a double logarithmic scale, showing the linear dependency.

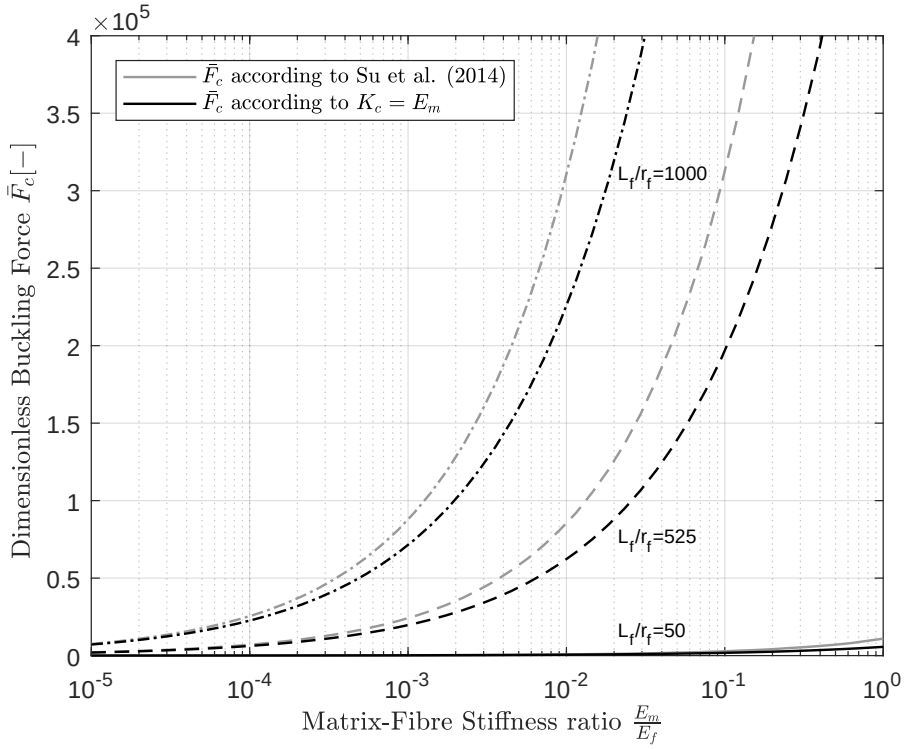

Figure 3.3: The critical buckling load $\overline{F}_c$ plotted versus the matrix-fibre stiffness ratio E_m/E_f for both approximations of $\overline{K}_c$ and three values of $\frac{L_f}{r_f}$.

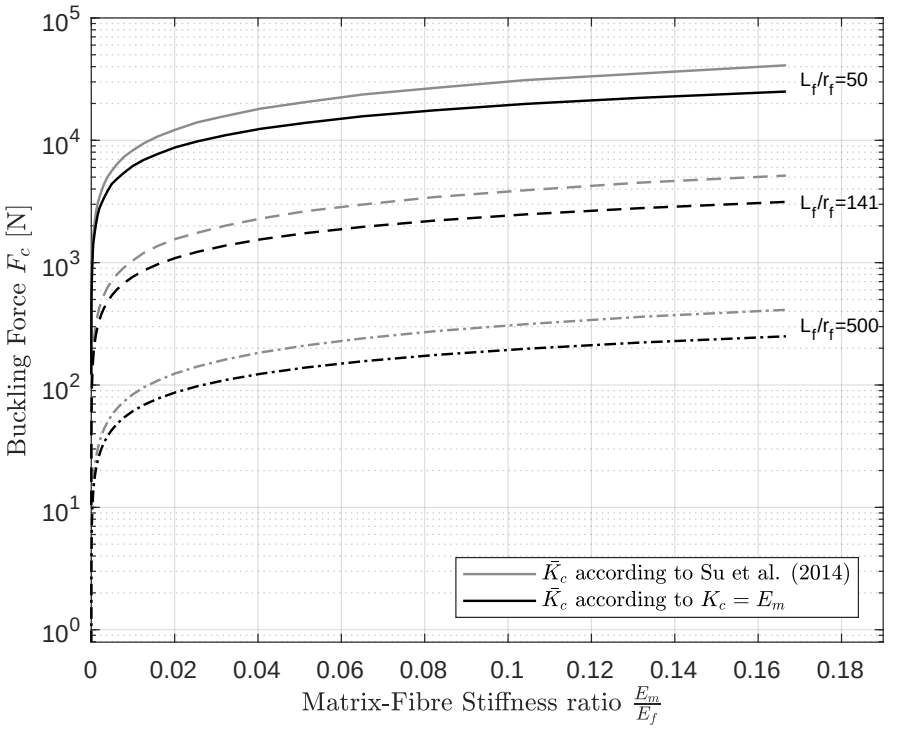

Figure 3.4: F_c [N] versus E_m/E_f. Higher critical buckling loads are found for less slender fibres, indicating the counter-intuitive results in 3.3 are due to dimensionless formulation of F_c.

A discrepancy in the approximations of the continuous spring stiffness $\overline{K}_c$ and resulting critical buckling load $\overline{F}_c$ by the Young's modulus approach and the approach of Su et al. (2014) is observed in Figures 3.2 till 3.4. The approximation of the foundation modulus with the Young's modulus approach results in lower values than those obtained with the approach of Su et al. Consequently, the obtained critical buckling forces are lower as well. The source of this discrepancy has been further evaluated by plotting the ratios between the results of the approximation methods with respect to the fibre aspect ratio.
In Figure 3.5 the ratio $\overline{K}_{cSu}$ / $\overline{K}_{cE_m}$ is plotted versus the fibre aspect ratio. The resulting lines are nearly horizontal indicating that the ratio between the approximations is mainly depending on the matrix-fibre stiffness ratio E_m/E_f.
The same conclusion holds for Figure 3.6 in which the ratio between the obtained critical buckling forces $\overline{F}_{cSu}$ / $\overline{F}_{cE_m}$ is plotted versus the fibre aspect ratio for three different values of the matrix-fibre stiffness ratio. For lower ratios, that is for fibre composites in which the Young's modulus is substantially less than the Young's modulus of the fibre, the deviation between both approximations is decreasing. For higher ratios, however, the deviation is substantial and the ratios $\overline{K}_{cSu}$ / $\overline{K}_{cE_m}$ and $\overline{F}_{cSu}$ / $\overline{F}_{cE_m}$ rise up to a value of 3 and 2 respectively.
The observations are summarised in Figure 3.7, in which the ratios between the results of the approximation methods for both the spring stiffness and critical buckling load are shown with respect to the matrix-fibre stiffness ratio E_m/E_f. From figures 3.5 and 3.6, it is concluded that both ratios are nearly independent of the fibre aspect ratios and that, following from 3.7, for low values of E_m/E_f the difference is sufficiently small allowing the application of the more simple approximation of the foundation modulus by $K_c = E_m$.

3.1.2 Frictional resistance

In addition to the lateral support of the matrix against buckling of the embedded fibre, resistance against vertical displacement of the fibre with respect to the matrix due to friction on the fibre-

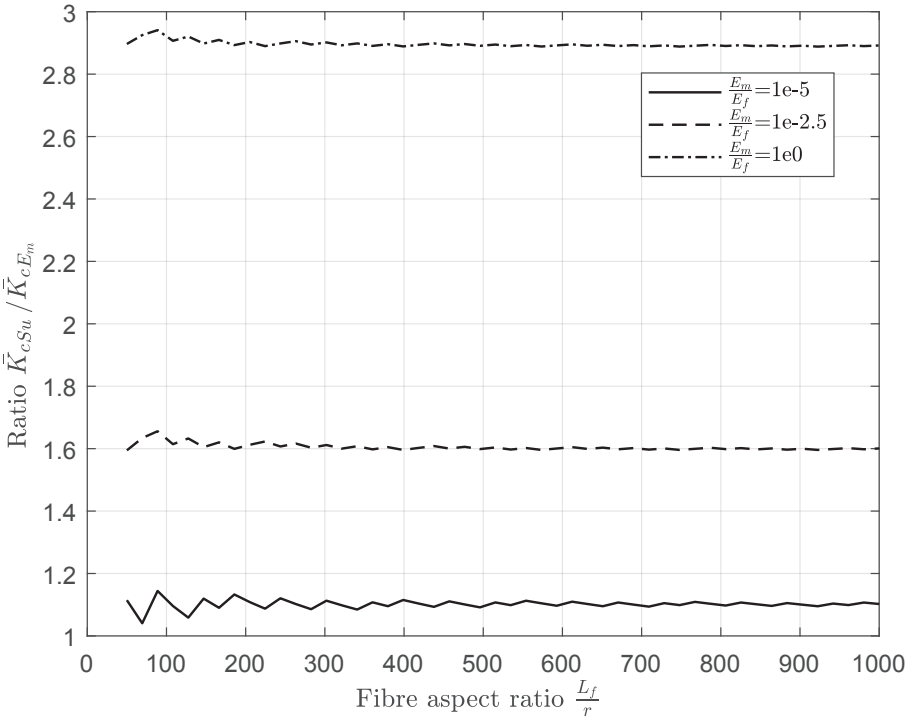

Figure 3.5: Ratio between approximation methods for $\overline{K}_{cSu}$ / $\overline{K}_{cE_m}$ plotted versus the fibre aspect ratio $\frac{L_f}{r_f}$ for three different matrix-fibre stiffness ratios.

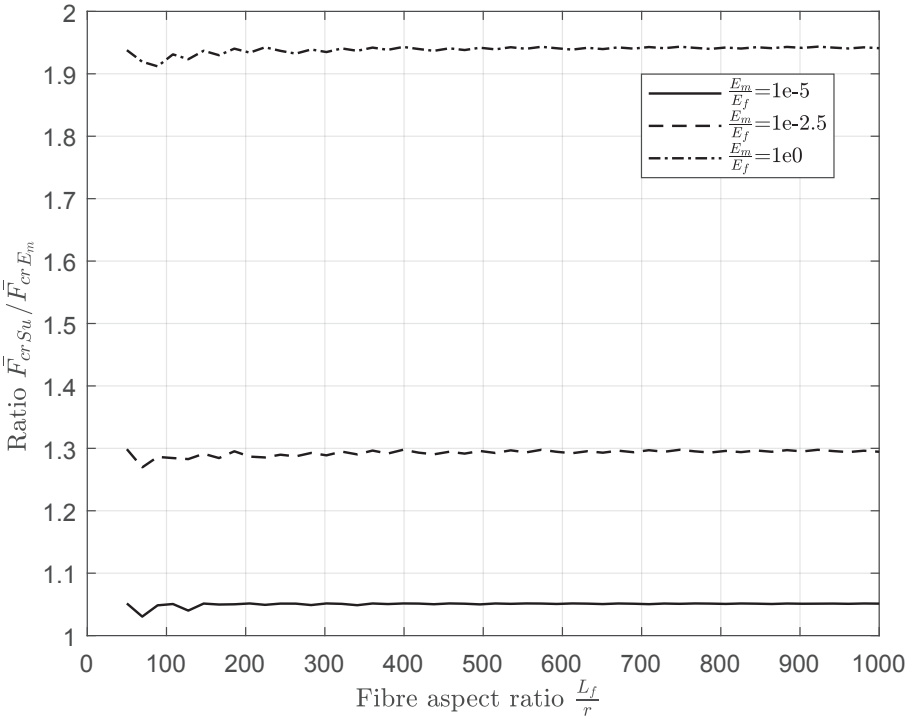

Figure 3.6: Ratio between approximation methods for $\overline{F}_{cSu}$ / $\overline{F}_{cE_m}$ plotted versus the fibre aspect ratio $\frac{L_f}{r_f}$ for three different matrix-fibre stiffness ratios.

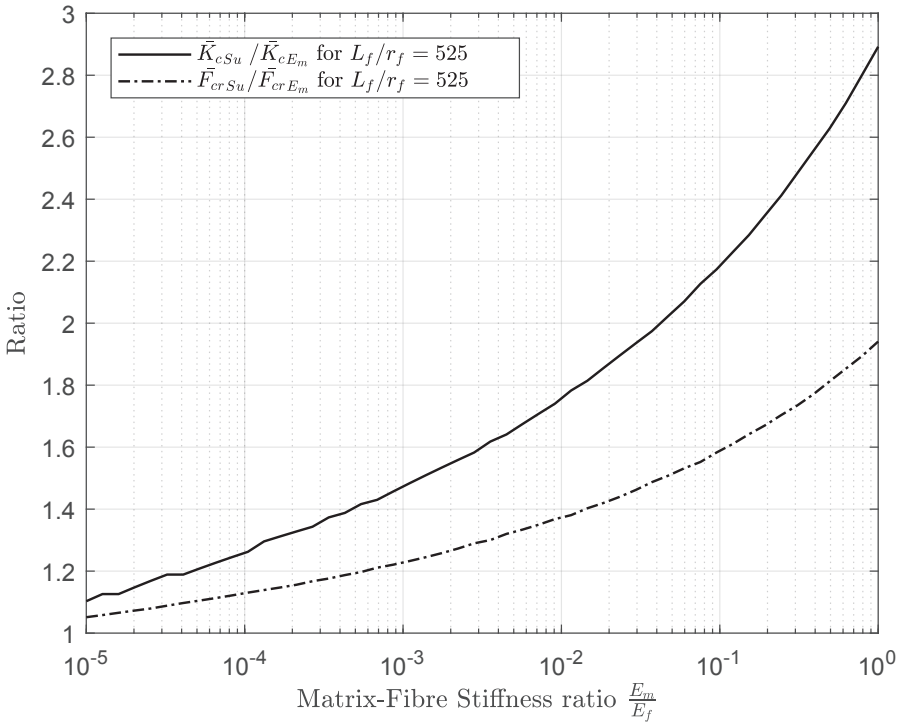

Figure 3.7: Ratios $\overline{K}_{cSu}$ / $\overline{K}_{cE_m}$ and $\overline{F}_{cSu}$ / $\overline{F}_{cE_m}$ plotted versus the matrix-fibre stiffness ratio. It is concluded that for low values of E_m/E_f the difference is sufficiently small so that the approximation of the foundation modulus by $K_c = E_m$ may be adopted.

matrix interface is considered. This effect is modelled by discrete vertical translational springs, which place the frictional resistance over the fibre-matrix interface to the element nodes.
The discrete spring stiffness $\overline{k}_v$ is approximated using the shear modulus of the matrix

$$G_m = \frac{E_m}{2(1+\nu_m)}, \tag{3.8}$$

in which ν_m represents the Poisson's ratio of the matrix which may range between zero and 0.5 $0 \leq \nu_m \leq 0.5$. Adopting this range, one may find the shear modulus to vary between

$$\frac{E_m}{3} \leq G_m \leq \frac{E_m}{2}. \tag{3.9}$$

From the previous section, it is concluded that the discrete spring stiffness representing the lateral support is proportional to the Young's modulus of the matrix, $\overline{k} \sim E_m$. Assuming the vertical discrete spring stiffness, which represents the frictional resistance, is proportional to the shear modulus of the matrix $\overline{k}_v \sim G_m$, then leads to the following approximation of $\overline{k}_v$:

$$0,33\overline{k} \lesssim \overline{k}_v \lesssim 0,5\overline{k}. \tag{3.10}$$

Eq. 3.10 is implemented in the numerical model. It has no influence, however, in the linear buckling model since the bifurcation load is found upon the loss of stability in the initial equilibrium condition using a linear buckling analysis, no vertical displacement of the nodes is taken into account.
In the non-linear analysis, another issue arises due to the modelling technique used in the present work. The influence of the vertical springs is depending on the vertical displacement of the nodes directly, whereas is should depend on the net vertical displacement between the nodes of the fibre and their initial neighbouring matrix elements. The contribution of the vertical springs is therefore overestimated.
Moreover, the contribution of the vertical springs increases when the system is subjected to higher loads. This causes the springs to 'absorb' relatively more energy while modelling fibre composites with higher matrix moduli, since the associated buckling load for those composites is higher. The results obtained for different matrix moduli, then become incomparable.
Due to these modelling issues and the limited influence of the frictional resistance on the buckling behaviour of the fibre, the vertical translational springs are omitted in the remainder of the present work.

3.1.3 Application

An experimental setup used to simulate the behaviour of unidirectional fibres embedded in a matrix, is composed out of (uncooked) spaghetti strands embedded in a silicone elastomer matrix (Scappin, 2017). The material properties of both constituents fall within the range of parameters for common fibre reinforced composites as represented in Section 3.1.1 and are shown in table 3.1. The non-linear DEM model is used to analyse the behaviour of a single spaghetti strand in a silicone elastomer subjected to axial compressive loading. The results are shown in Figure 3.8. The deflection of the strand is shown at several locations in the force-displacement diagram.

Table 3.1: Fibre and matrix properties

Spaghetti strand in Silicone Elastomer

Spaghetti	Young's modulus	6000	MPa
	Poisson's ratio	0.3	-
	Length	80	mm
	Radius	0.85	mm
Silicone elastomer	Young's modulus	3	MPa
	Poisson's ratio	0.42	-

Irrespective of the initial imperfection, the strand buckles into the critical buckling mode corresponding to the continuous spring stiffness $\overline{K}_c$, which is based on the matrix-fibre stiffness ratio. For the embedded spaghetti strand, the fifth buckling mode appears to be the governing mode, which is in accordance with the analytical predictions.

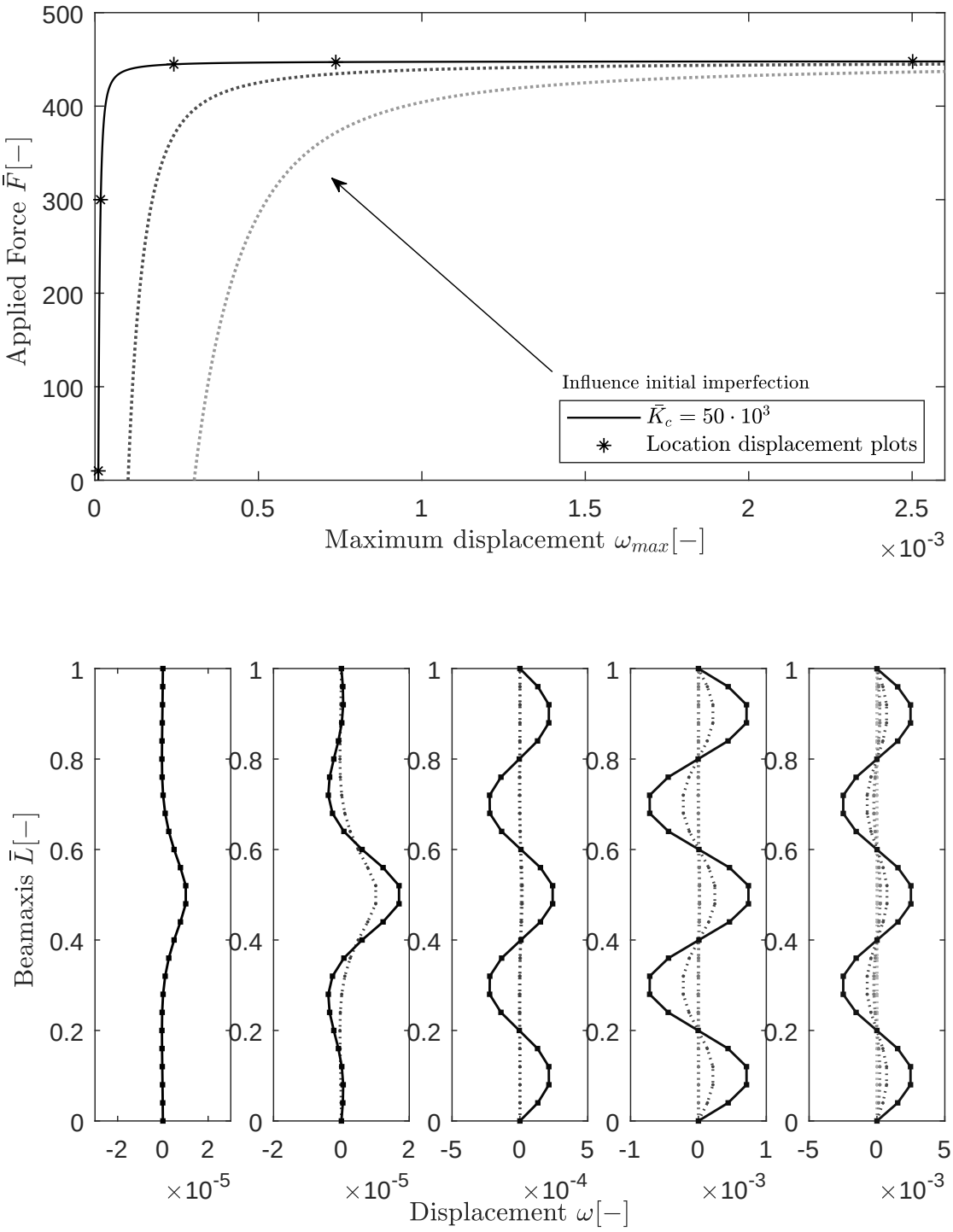

Figure 3.8: Buckling of a spaghetti strand in a silicone elastomer. The deflection of the strand is shown for several locations in the load-displacement diagram.

3.2 Bilinear matrix behaviour

In this sectionm the non-linear behaviour of a matrix is approximated with a bilinear material model. The initial Young's modulus of the matrix is modified when the strain of the matrix exceeds a certain value. It is assumed that the strain is proportional to the nodal horizontal displacement of the fibres in the Discrete Element Model. If the displacement of a certain node exceeds a certain predefined displacement ω_0, the value of the associated discrete spring stiffness is adapted according to a bilinear reduction factor α, which relates the linear Young's modulus of the matrix in the second branch to the initial Young's modulus:

$$\begin{aligned} \overline{\omega}_n \leq |\omega_0| &\rightarrow \overline{k}_{bl1} = \overline{k}, \\ \overline{\omega}_n \geq |\omega_0| &\rightarrow \overline{k}_{bl2} = \alpha \cdot \overline{k}. \end{aligned} \tag{3.11}$$

In Figure 3.9 the buckling behaviour of a single embedded fibre is plotted for varying values of the reduction factor α. It is observed that when the onset of the bilinear branch occurs before the buckling load corresponding to the initial Young's modulus of the matrix is reached, the Young's modulus of the second branch of the bilinear model determines the critical buckling load. Depending on the value of ω_0 defined as the nodal displacement of the fibres corresponding to the onset of bilinear behaviour, the reduction factor α influences either only the post-buckling behaviour (if the fibre buckles before ω_0 is reached) or the critical load as well if ω_0 is reached before the fibre buckles.

3.3 Damage behaviour

The evaluation of non-linear matrix behaviour can be further extended by taking damage of the matrix into account. In accordance with 3.2 the matrix behaviour is approximated using a bilinear

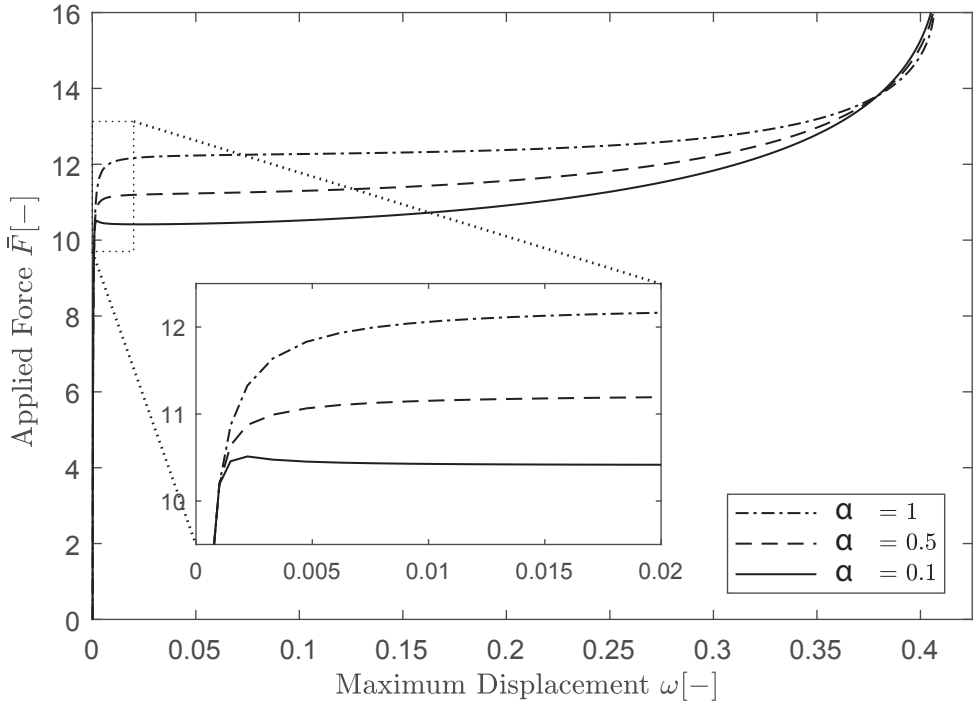

Figure 3.9: Force versus maximum nodal displacement of an embedded fibre for varying values of the bilinear reduction factor α and a fixed value for the onset of bilinear behaviour ω_0.

material model. Additionally, matrix failure is taken into account as soon as the nodal displacement of the fibre exceeds a certain predefined value ω_f. In the present work, this value is taken to be merely depending on the initial Young's modulus of the matrix, the onset of bilinear behaviour ω_0 and the bilinear reduction factor α by:

$$\omega_f = \omega_0 + \frac{\overline{k} \cdot \omega_0}{-\alpha \cdot \overline{k}}. \tag{3.12}$$

It should be noted that the bilinear reduction factor α is assumed to be negative for damage models of the matrix, so that $\overline{k}_{bl2} = \alpha \cdot \overline{k}_{bl1}$ results in a negative value for $\overline{k}_{bl2}$.

To illustrate the meaning of introduced parameters, Figure 3.10 is created. In the left, a stress-strain diagram showing the matrix constitutive behaviour is given, whereas in the right, the translation towards the discrete springs is illustrated. The stress-strain behaviour of the matrix is approximated using a bilinear material model. The onset of bilinear behaviour relates to the strain at which plasticity is initiated. The spring stiffness related to the second branch of the bilinear model $\overline{k}_{bl2}$ depends on the bilinear factor α. The nodal displacement associated with failure, ω_f is shown to be dependent on both α and ω_0. The influence of the different non-linear matrix properties can be best observed with the results of a non-linear analysis of a single embedded fibre for varying values of the onset of bilinear matrix behaviour, ω_0. In figure 3.11a these results are plotted.
Firstly it is noted that the post-buckling behaviour for all modelled parameter sets finally equals the post-buckling behaviour of an unsupported fibre. This can be explained by the fact that if the nodal displacements of the fibre exceed the displacement associated with failure of the matrix, $\omega > \omega_f$, the spring stiffness representing the matrix becomes zero. Hence, the post-buckling behaviour will equal the post-buckling behaviour of a fibre without matrix support.
The displacement associated with the onset of this post-buckling behaviour is merely depending on ω_0 as is illustrated in Figure 3.11b with the continuous grey lines. The range of displacements in which the post-buckling behaviour from an embedded fibre converges towards the post-buckling behaviour of an unsupported fibre, as shown by the arrows in Figure 3.11b, depends directly on ω_f and therefore merely on the initial Young's modulus of the matrix, the onset of bilinear behaviour ω_0 and the bilinear reduction factor *alpha* itself. Hence, for fixed values of the bilinear reduction factor and initial Young's modulus of the matrix, this range increases for increasing values of ω_0.

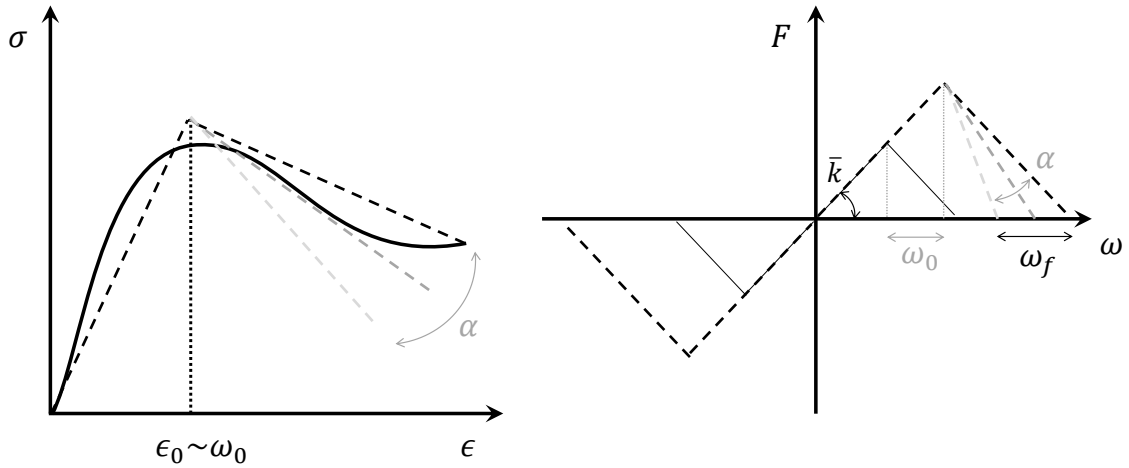

Figure 3.10: Illustrative representation of the parameters concerned with bilinear matrix behaviour. The left figure shows she matrix constitutive behaviour and on the right the influence of the parameters on the stiffness of the springs in the discrete system is shown.

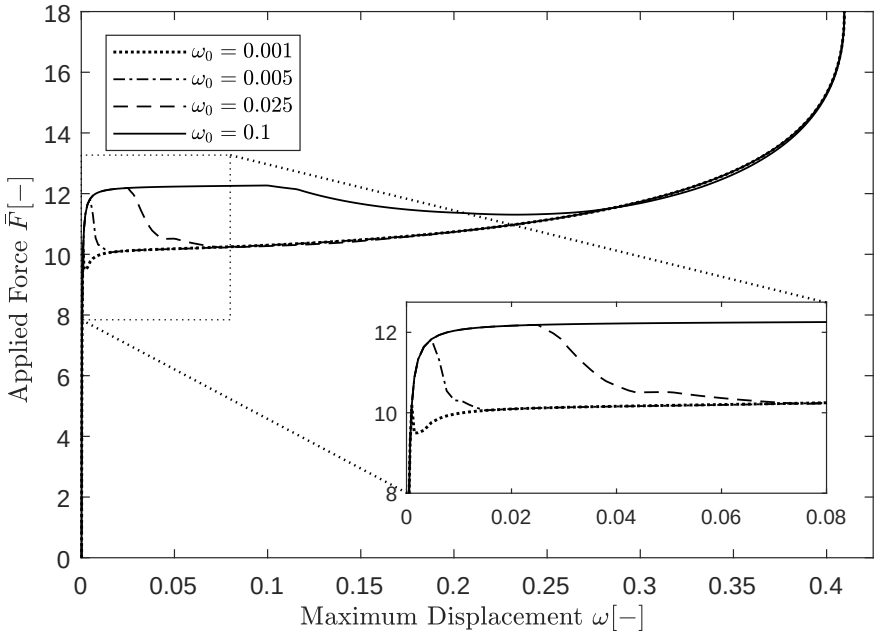

(a)

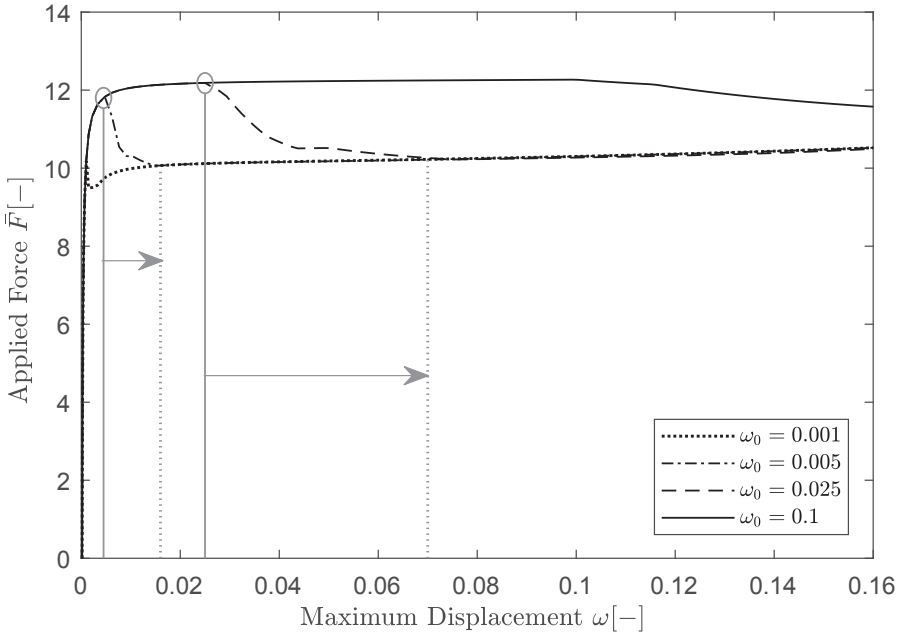

(b)

Figure 3.11: The influence of varying values for the onset of bilinear matrix behaviour. The arrows in the bottom figure indicate the range of displacement needed to reach the final post-buckling behaviour that equals the post-buckling behaviour of an unsupported fibre.

4 Multiple embedded fibres

In this Section the numerical model is extended towards multiple embedded fibres.
The compressive failure of fibre bundles in a composite due to elastic or plastic micro-buckling is examined. Multiple fibres embedded in an elastic medium may buckle either in-phase (shear buckling mode), or out-of-phase (transverse buckling mode) with each other. When the surrounding matrix behaves non-linear, fibre kinking (plastic micro-buckling) is in most cases expected to govern the compressive failure of the fibre bundle. The governing mechanism strongly depends on the foundation modulus of the matrix K_c and the initial fibre imperfections.
In Section 4.1 the extension of the individual fibre model towards a model for multiple embedded fibres is elaborated. To capture the fibre-matrix interaction correctly, several adaptions to the original extended model are proposed. Finally, for one modelling approach the influence of the Fibre Volume Fraction (FVF) and plastic material behaviour is discussed.

4.1 Multiple fibre model

To model the behaviour of fibre bundles in a matrix, the discrete individual fibre model is extended for multiple fibres as shown in Figure 4.4. A certain number of fibres m_f is modelled using m discrete elements. The support by the matrix is modelled, in accordance with the individual fibre model, by discrete translational springs. The spring stiffness is computed similarly to Section 3.1, following the Young's modulus approach. The springs connect the corresponding nodes of adjacent fibres to each other, thus coupling the behaviour of the fibres within a bundle. The translational springs are relaxed for the initial position of the fibre. Hence, the buckling behaviour of the fibres is strongly correlated with the initial imperfection and the corresponding misalignment of the fibres. This is illustrated using a model of a fibre bundle consisting of 5 fibres with different buckling shapes as initial imperfections. The results are shown in Figures 4.1 and 4.2. In Figure 4.1 the load-displacement curve for all fibres is shown. Buckling of the individual fibres is observed at the same critical load, however the maximum displacement of the fibres during the load steps differs slightly depending on the initial imperfection. In Figure 4.2 the displacements over the beam axis of the fibres is plotted at several steps in the load-displacement curve (as indicated with a '$*$' in Figure 4.1). It is observed that the fibres, according to this model, eventually buckle in phase. Moreover, in a parameter study with varying buckling modes as initial imperfection, it is observed that the governing buckling mode equals the highest buckling mode imposed to the system as an initial imperfection. For the example in Figures 4.1 and 4.2, this results in buckling of the fibre bundle according to the fourth buckling mode.

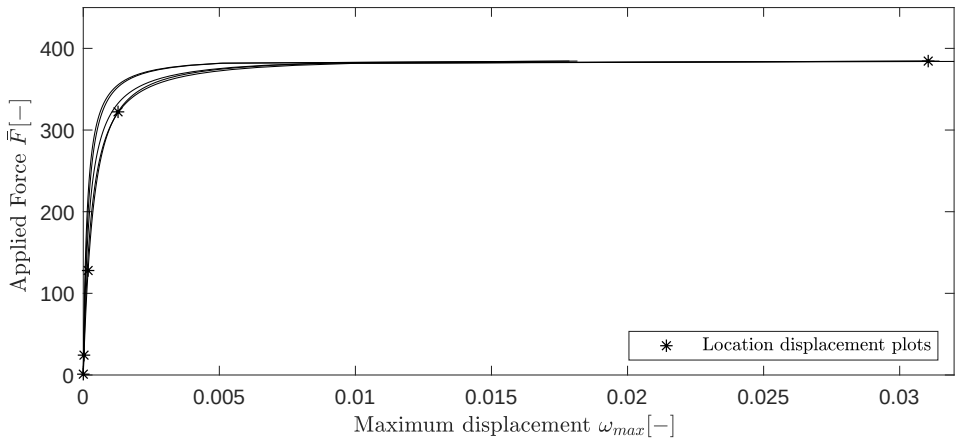

Figure 4.1: Load-displacement curve for a fibre bundle consisting of 5 fibres with different initial imperfections.

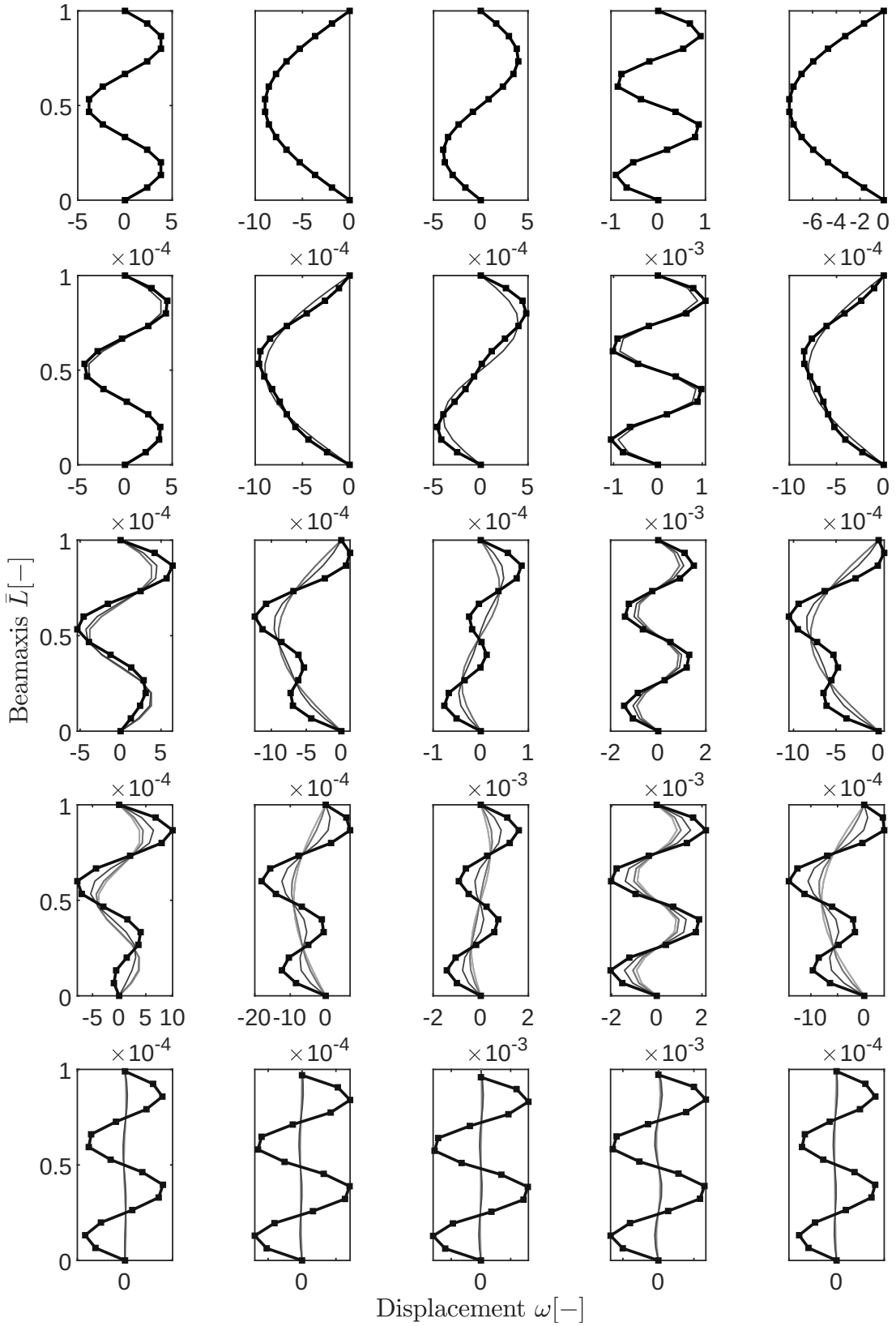

Figure 4.2: Displacements of the fibres at several locations in the load-displacement curve. The initial imperfection is shown in the top row, whereas the final buckling shape is shown in the bottom row.

4.1.1 Discrepancy with true fibre-matrix interaction

With the current DEM model for multiple embedded fibres, the buckling behaviour appeared to be less depending on the foundation modulus of the matrix and strongly correlated with the highest buckling mode imposed as initial imperfection. When the same buckling mode is imposed as the initial imperfection of all fibres, it is observed that the buckling load of the fibres, obtained with the current DEM model, depends on the number of fibres modelled in the fibre bundle, m_f. For large values of m_f, the buckling load converges towards the analytical value for the buckling load of an un-embedded individual fibre, $\overline{F}_c = \pi^2$.
In Figure 4.3 the load-displacement curves of fibre bundles are plotted for a varying amount of fibres within a bundle, m_f, showing the convergence towards $\overline{F}_c = \pi^2$ for large m_f. This behaviour can be explained by the fact that with the current modelling approach, once the fibres within a bundle buckle in phase, the contribution of the internal springs to the total potential energy is eliminated. Hence, the influence and support of the surrounding matrix is from that moment on only felt near the edge of the fibre bundle. For increasing amounts of fibres within a bundle, the influence of the matrix is therefore decreasing, resulting in lower critical buckling loads, eventually converging towards the buckling load of an un-embedded fibre. It is therefore concluded that the current modelling approach, as illustrated in Figure 4.4, does not capture the influence of the surrounding matrix correctly, since it does not capture the support by the matrix to the inner fibres of a fibre bundle. Additionally, this causes the modelling approach to be incapable of taking the influence of the fibre volume fraction into account. Two alternative modelling approaches are therefore considered.
In Figure 4.5 the first approach is shown. The coupling between the fibres in a bundle is captured in a similar way as the original model shown in Figure 4.4, by internal translational springs connecting the nodes of adjacent fibres to each other. The spring stiffness of these internal coupling springs is computed as

$$\bar{k}_{i,coupling} = f(\mathrm{v}_f) \cdot \bar{k}, \tag{4.1}$$

in which $\bar{k} = \frac{\bar{K}_c}{m}$ is computed following the Young's modulus approach (Section 3.1), and $f(\mathrm{v}_f)$ is a function of the fibre volume fraction v_f which is in the range of $0 \leq f(\mathrm{v}_f) \leq 1$. For large fibre volume fractions, the function equals 1, for small fibre volume fractions, the influence of adjacent fibres is limited and the stiffness of the coupling springs is approaching 0. The influence of fibre volume fractions is further elaborated in Section 4.2.

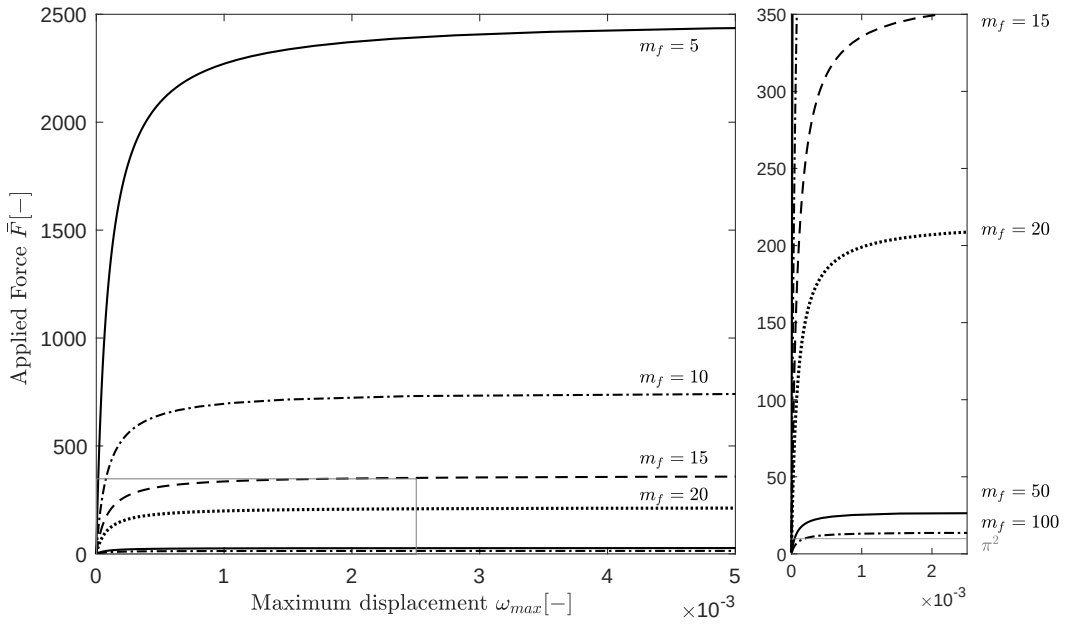

Figure 4.3: Load-displacement curve of fibre bundles plotted for varying amounts of fibres.

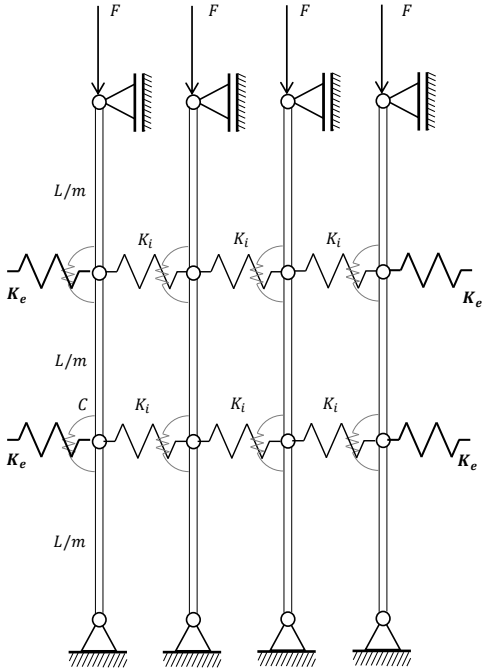

Figure 4.4: Extension of the model for individual fibres towards the model for fibre bundels in a matrix.

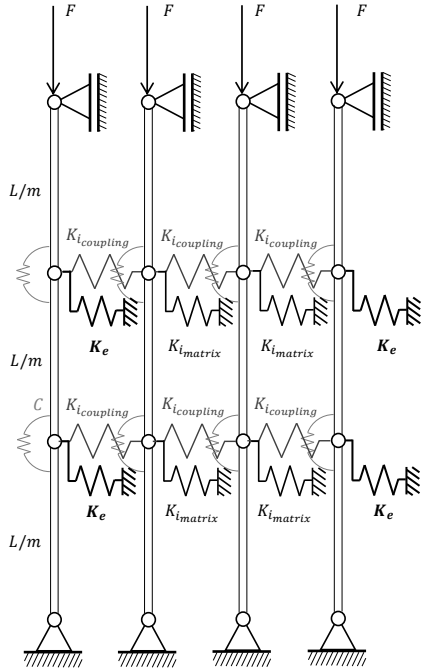

Figure 4.5: Adaption to the multiple fibre model to capture the fibre-matrix interaction correctly.

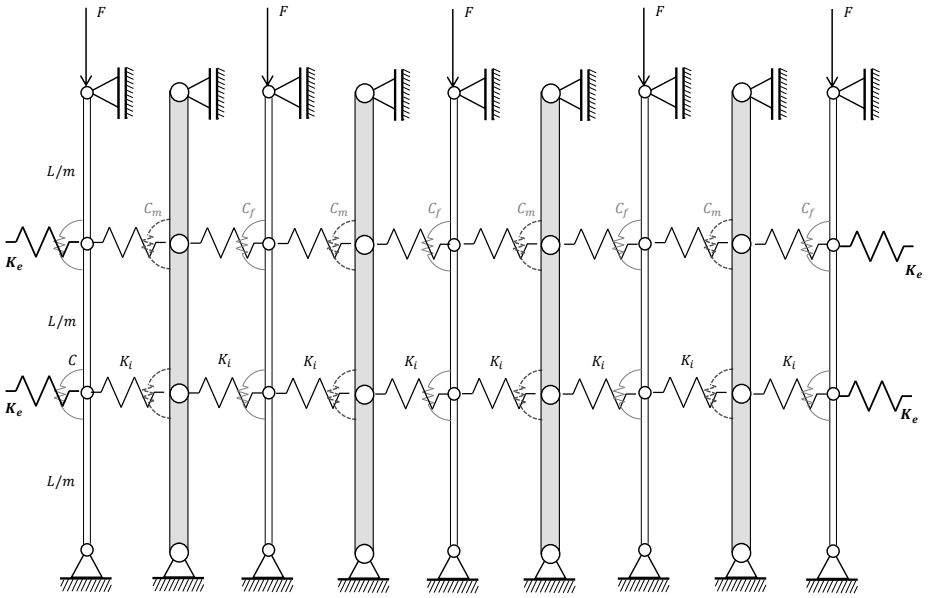

Figure 4.6: Alternative approach for capturing the fibre-matrix interaction correctly by modelling the matrix material directly.

In addition to the internal coupling springs, so called internal matrix springs are introduced to capture the support of the surrounding matrix to the internal fibres of the bundle. These springs are connected to the ground and act similar to the external springs. The stiffness of the internal matrix springs is equal to the external springs for low fibre volume fractions, but reduced for high fibre volume fractions. In case of the former, the centre-to-centre distance of the fibres is large, causing the support of the matrix to equal the support to a fibre by an unbounded medium (similar to the individual fibre model). For the latter, the centre-to-centre distance of the fibres is small, causing the support of the matrix to be decreased, since the bending stiffness of the matrix layer is limited. The spring stiffness of these internal matrix springs is therefore computed as

$$\bar{k}_{i,matrix} = g(\mathrm{v}_f) \cdot \bar{k}, \tag{4.2}$$

in which $g(\mathrm{v}_f)$ is a function of the fibre volume fraction acting in the range of $0 \leq g(\mathrm{v}_f) \leq 1$ with $g(\mathrm{v}_f)$ approaching 1 for small fibre volume fractions, and 0 for high fibre volume fractions.

The computation of the reduction function $g(\mathrm{v}_f)$ can be challenging since a transition in support mechanism of the matrix to the fibres is observed. For large centre-to-centre distances, the support of the matrix is provided by resistance against compression while the behaviour of the matrix approaches the behaviour of an unbounded medium subjected to compression. For small centre-to-centre distances, the support is governed by the bending resistance of the matrix layer. The second modelling approach for the multiple fibre model, directly models these matrix layers as shown in Figure 4.6. In this approach, the matrix layers are modelled similar to the fibres with discrete elements. The bending stiffness of the matrix is taken into account by rotational springs of which the value is computed in correspondence to Section 2.2.2.1. The coupling between the fibres and matrix is captured by internal translational springs in correspondence with the first approach (Figure 4.5).
For the second approach, it is required to, besides the fibres, also model the matrix using discrete elements. In this research it is, however, tried to capture the behaviour of embedded fibres by only modelling the fibre elements and taking the influence of the matrix in account by translational springs, following Rosen's approach. Therefore, in the present work, the first approach is adopted in order to capture the matrix fibre interaction correctly and analyse the influence of fibre volume fractions, while the incorrect strong dependence of the buckling load of the fibres on the amount of fibres in a bundle (m_f) is eliminated.

4.1.2 Influence of imperfection modelling

For very low fibre volume fractions, i.e. for large centre-to-centre distances of fibres, the behaviour of a fibre in the multiple fibre model is expected to correspond with the behaviour of an individual embedded fibre. This dependency on the fibre volume fraction is taken into account by the reduction functions $f(\mathrm{v}_f)$ and $g(\mathrm{v}_f)$, approaching the values of 0 and 1 respectively for low v_f. However contrary to the expectation, for low v_f and a fixed value of the foundation modulus $\bar{K}_c$, a large discrepancy is observed between the results obtained with the current DEM models for individual fibres and fibre bundles.
Further research has shown that this discrepancy is caused by the modelling approach of the initial imperfections of the fibres. Whereas initial imperfections required for the initiation of the non-linear analysis were modelled by a small perturbation force in the individual fibre DEM model, in the multiple fibre DEM model a buckling shape corresponding to a n-th buckling mode has been imposed to the fibres. If the initial imperfection is modelled using the same method for both the individual and multiple fibre model (either a perturbation force or an imposed buckling shape), the results for low volume fractions coincide as expected. However, when the initial imperfection is imposed as a buckling shape, a much stiffer behaviour and higher critical buckling load is found, compared to the results found for the same foundation modulus $\bar{K}_c$ with an initial imperfection introduced by a small perturbation force and the analytical solution, see Figure 4.7. In Figure 4.7 it can be seen that for low volume fractions, the results of the multiple fibre DEM model coincide with the results of the individual fibre DEM model. Moreover, it is observed that if the buckling mode imposed as initial imperfection of the fibres equals the governing buckling mode for that specific foundation modulus of the matrix (according to the analytical solution), the same buckling behaviour is found with the perturbation force approach and buckling shape approach. The offset

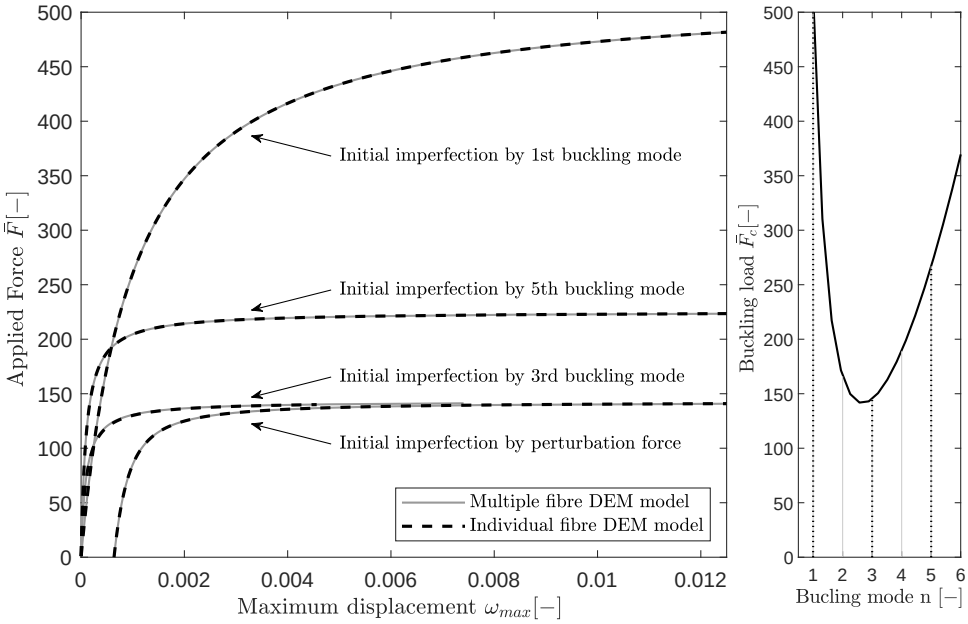

Figure 4.7: The influence of the modelling approach of the initial imperfections on the buckling behaviour of individual and embedded fibres for a foundation modulus of $\bar{K}_c = 5000$. The buckling loads according to the analytical solution are shown in the right graph.

in maximum displacement for the perturbation force approach is due to a larger initial displacement caused by the force compared to the initial displacement by the buckling shape. However, when a buckling shape corresponding to any other buckling mode is imposed, a higher buckling load is found for the fibres. The observed buckling loads for those initial imperfections approach the buckling load for the corresponding mode as obtained with the analytical solution, as plotted in the right graph of Figure 4.7. The effects of initial imperfections by buckling modes other than the initially governing buckling mode on the buckling behaviour is similar to the behaviour of axially loaded members subjected to second order imperfections in the work of Bos (2019).
It is concluded that the buckling behaviour of the fibres is strongly correlated with the imposed initial imperfections, however, further research is required to obtain the relation between those imperfections and the true behaviour of fibres embedded in a composite. In the current work, a further imperfection sensitivity analysis is not conducted and it is therefore chosen to model the initial imperfections with a small perturbation force, solely to initiate the non-linear analysis.

4.2 Fibre Volume Fractions

As introduced in Section 4.1, one of the characteristics of fibre reinforced composites is their fibre volume fraction (FVF) v_f. The fibre volume fraction can be related to the geometrical properties of a fibre reinforced composite using the definitions as shown in Figure 4.8. Assuming equal circular cross sections for all fibres with corresponding fibre radius r_f and a centre-to-centre distance of the fibres of $2R$, the fibre volume fractions for the two packing arrangements are found as

$$\mathrm{v}_f = \frac{\pi}{4}(\frac{r_f}{R})^2 \quad \text{for square packing arrangements,} \tag{4.3a}$$

$$\mathrm{v}_f = \frac{\pi}{2\sqrt{3}}(\frac{r_f}{R})^2 \quad \text{for hexagonal packing arrangements.} \tag{4.3b}$$

A theoretical maximum fibre volume fraction is reached when neighbouring fibres are touching, i.e. $w = 0$ and therefore $r_f = R$. Accordingly, the theoretical maximum fibre volume fractions are $\mathrm{v}_{f,max} = 0.785$ and $\mathrm{v}_{f,max} = 0.907$ for square and hexagonal packing, respectively. However, due

to slight variation in fibre diameter and irregularities in fibre packing, the maximum fibre volume fraction for unidirectional composites varies in practice between 0.6 and 0.7 (Altenbach, Altenbach, & Kissing, 2018; Spowart & Dève, 2000).
The influence of the fibre volume fraction is captured by the reduction functions $f(\mathrm{v}_f)$ and $g(\mathrm{v}_f)$ for $\bar{k}_{i,coupling}$ and $\bar{k}_{i,matrix}$ respectively, following Ueda et al. (2011). For increasing fibre volume fractions, the centre-to-centre distance of the fibres is decreasing resulting in the reduction functions $f(\mathrm{v}_f)$ and $g(\mathrm{v}_f)$ to approach 1 and 0, respectively. For low fibre volume fractions, the centre-to-centre distance of the fibres is large, resulting in a limited influence of neighbouring fibres on the behaviour of a single fibre. Hence, $f(\mathrm{v}_f)$ approaches 0. On contrary, the support of the matrix approaches the support to a fibre by an infinite medium, resulting in $g(\mathrm{v}_f)$ becoming 1.
The exact relation between the fibre volume fraction v_f and the value of the reduction functions falls outside the scope of the present work and requires additional research. It is suggested that the reduction function $f(\mathrm{v}_f)$, influencing the coupling term, can be determined analogous to the strains in the matrix. Since the strains of the matrix are proportional to its deformation, the function $f(\mathrm{v}_f)$ is expected to be proportional to

$$f(\mathrm{v}_f) \sim \frac{\omega_{net}}{\mathrm{w}}, \tag{4.4}$$

in which ω_{net} represents the deformation of the matrix calculated by the net difference in displacements of adjacent fibre nodes and w is the initial width of the matrix layer between the fibres, as shown in Figure 4.8. For decreasing fibre volume fractions, the matrix width is increasing. While assuming a fixed net deformation of the matrix, the value of $g(\mathrm{v}_f)$ will then be decreasing, causing the influence of coupling between the fibres to reduce for decreasing v_f.
The initial width of the matrix layer can be calculated based on the fibre volume fraction, packing arrangement and fibre aspect ratio (Phoenix & Beyerlein, 2000) and is roughly approximated by

$$\mathrm{w} \approx \frac{1 - |\sqrt{\frac{4\mathrm{v}_f}{\pi}}|}{|\sqrt{\frac{4\mathrm{v}_f}{\pi}}|} \frac{L_f}{r_f}. \tag{4.5}$$

The results are shown in Figure 4.9 for varying fibre volume fractions and fibre aspect ratios.
It should be noted that the exact relations between the fibre volume fraction and reductions functions $f(\mathrm{v}_f)$ and $g(\mathrm{v}_f)$ require additional research. However, to indicate the influence of the fibre volume fractions, in the current work three sets of reduction values are evaluated for a fibre bundle in a matrix with foundation modulus $\bar{K}_c = 5000$. The fibres in the bundle are subjected to an initial imperfection defined by a small horizontal perturbation force at $x = 0.5L$, which alternately equals 1 or -1.
For the first set, the values for the reduction functions are taken as $f(\mathrm{v}_f) = 0$ and $g(\mathrm{v}_f) = 1$,

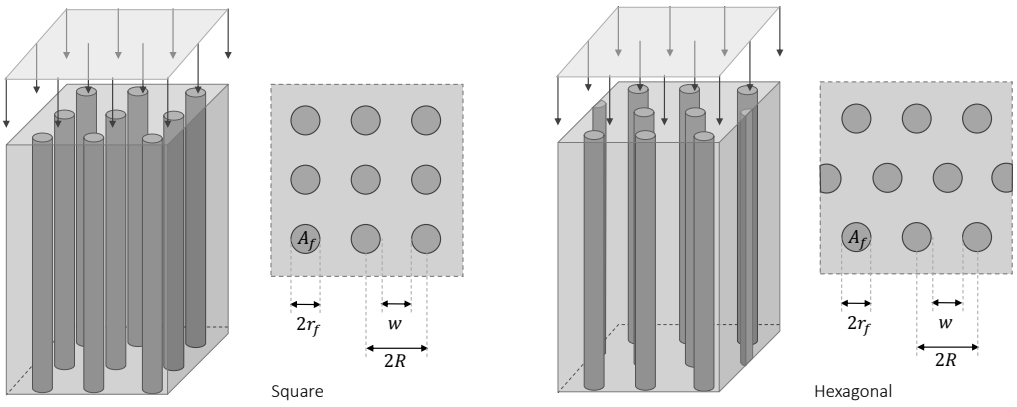

Figure 4.8: Two common fibre packing arrangements, square and hexagonal packing, with their geometric parameters.

resembling a fibre reinforced composite with very low fibre volume fractions. The influence of neighbouring fibres is eliminated and it is found that the fibres buckle individually in the direction of their initial imperfection according to the governing buckling mode based on $\bar{K}_c = 5000$. The load-displacement curve of the fibres in the bundle and their deformation is plotted at several increment steps in Figure 4.10. Without influence of neighbouring fibres, the fibres do not buckle in phase. In practice, this behaviour is expected for composites with a fibre volume fractions below 0.2 (Fleck, 1997).
For the second set, the values for the reduction functions are taken as $f(\mathrm{v}_f) = 1$ and $g(\mathrm{v}_f) = 0$, resembling a fibre reinforced composite with high fibre volume fractions. For high fibre volume fractions, the width of the matrix layer is small, resulting in no or only limited support of the fibres by the matrix itself. However, the coupling between the displacements of adjacent nodes increases. The results are plotted in Figure 4.11. Despite the opposite directions of the initial imperfections, it is observed that the fibres within the bundle now do buckle in phase. Due to the lack of support by the matrix, the buckling load for the fibres approximates the buckling load of an unsupported fibre. It should, however, be noted that the load which is plotted in the graphs corresponds to the load applied to a single fibre. For higher fibre volume fractions the distance between the fibres is smaller, hence the density of the load application is higher than for composites with lower fibre volume fractions. Therefore, it may be possible that a lower buckling load for a single fibre as shown in the graphs, may still cause a higher failure stress for a certain composite. To be able to evaluate which composite has the highest failure stress, the relation between the reduction functions and the fibre volume fraction should be established. Therefore, in this research, only the influence of physical parameters on the buckling behaviour and load of a single fibre, either individually embedded or present in a bundle, is evaluated.
Finally, for the third set, an attempt has been made to find the values for the reduction functions at which the break-even point between in- and out-of-phase buckling is located. Such a break-even point is found at $f(\mathrm{v}_f) = 0.32$ and $g(\mathrm{v}_f) = 0.68$ and the results are shown in Figure 4.12. Since both $f(\mathrm{v}_f)$ and $g(\mathrm{v}_f)$ depend on the fibre volume fraction, a certain relation between both values should hold, depending on the yet undefined relation of both reduction functions with v_f. The obtained values for the break-even point should therefore be considered as merely illustrative indication of the presence of a certain break-even point. The exact fibre volume fraction and corresponding values for the reduction functions for which a break-even point is found, can only be determined when the relation between v_f and $f(\mathrm{v}_f)$ and $g(\mathrm{v}_f)$ is constructed.

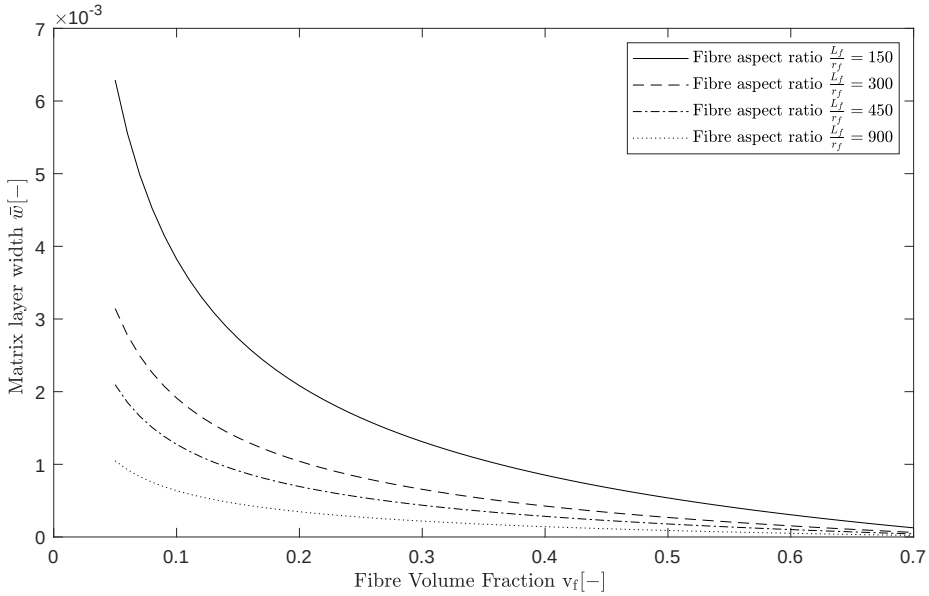

Figure 4.9: Matrix width required for the calculation of $f(\mathrm{v}_f)$ approximated using the applied fibre volume fraction and fibre aspect ratio.

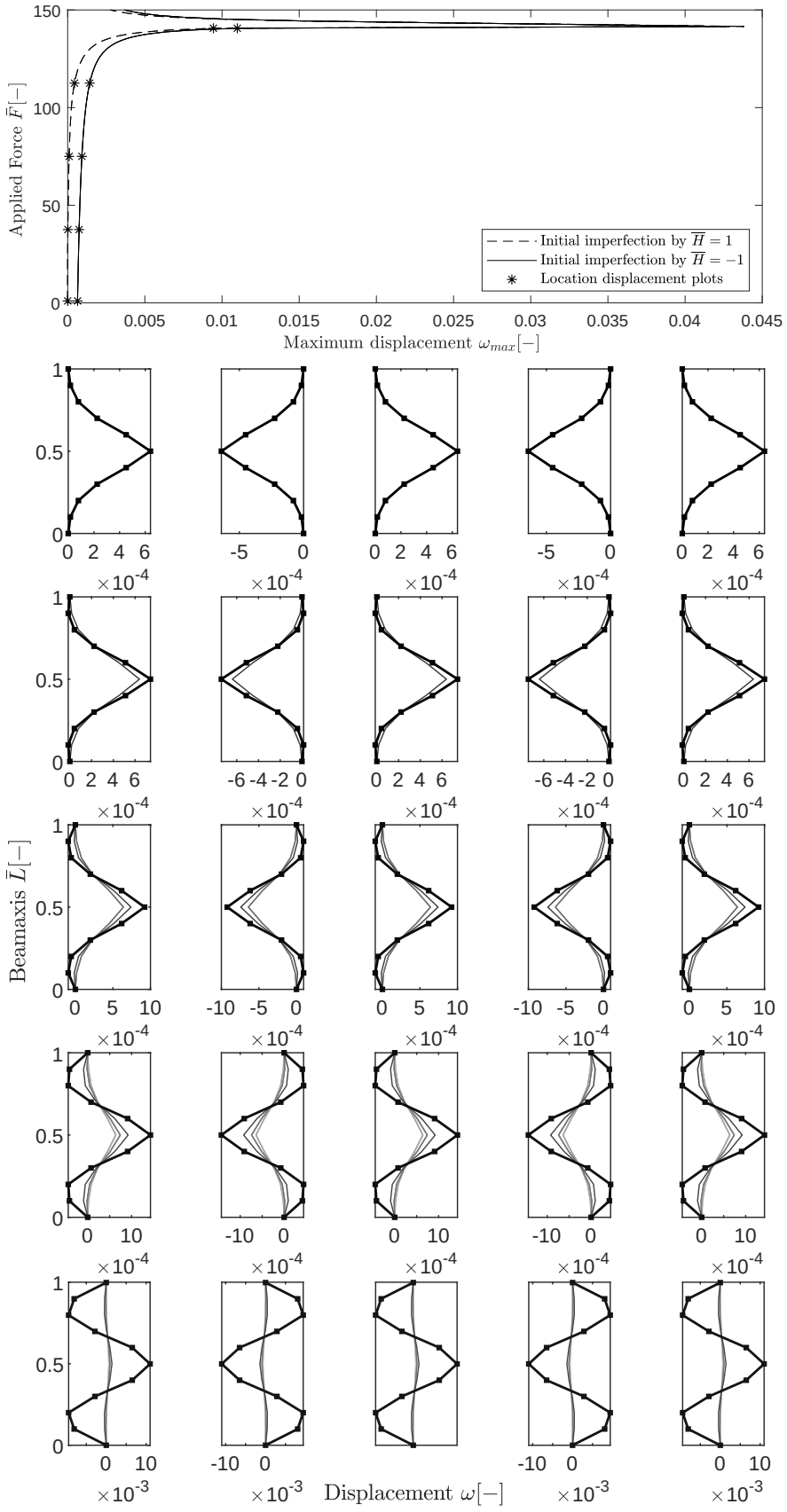

Figure 4.10: Load-displacement curve for fibre bundle in a composite with low fibre volume fraction, modelled using $f(\mathrm{v}_f) = 0$ and $g(\mathrm{v}_f) = 1$. The displacement of the fibres is shown at several increments.

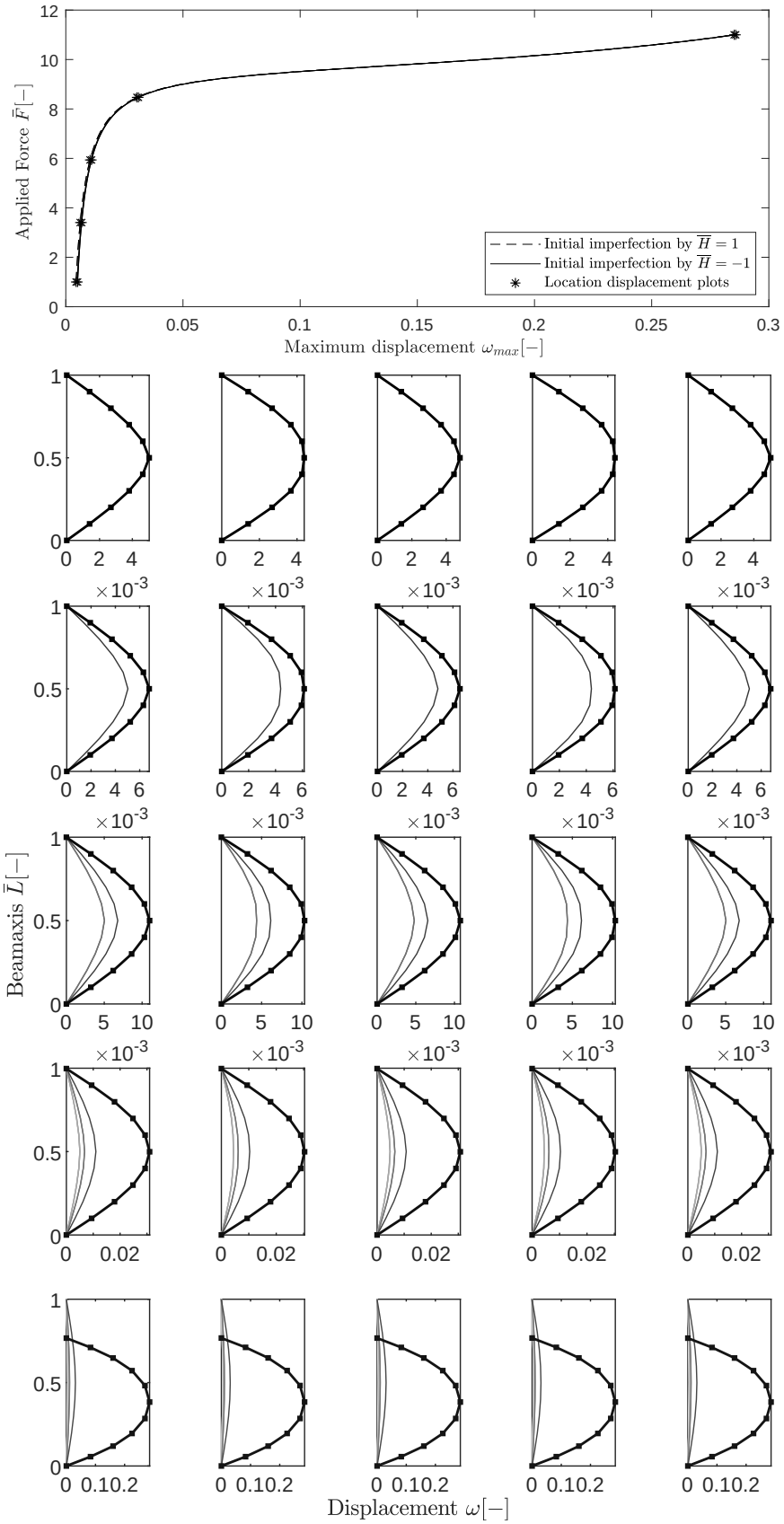

Figure 4.11: Load-displacement curve for fibre bundle in a composite with high fibre volume fraction, modelled using $f(\mathrm{v}_f) = 1$ and $g(\mathrm{v}_f) = 0$. The displacement of the fibres is shown at several increments.

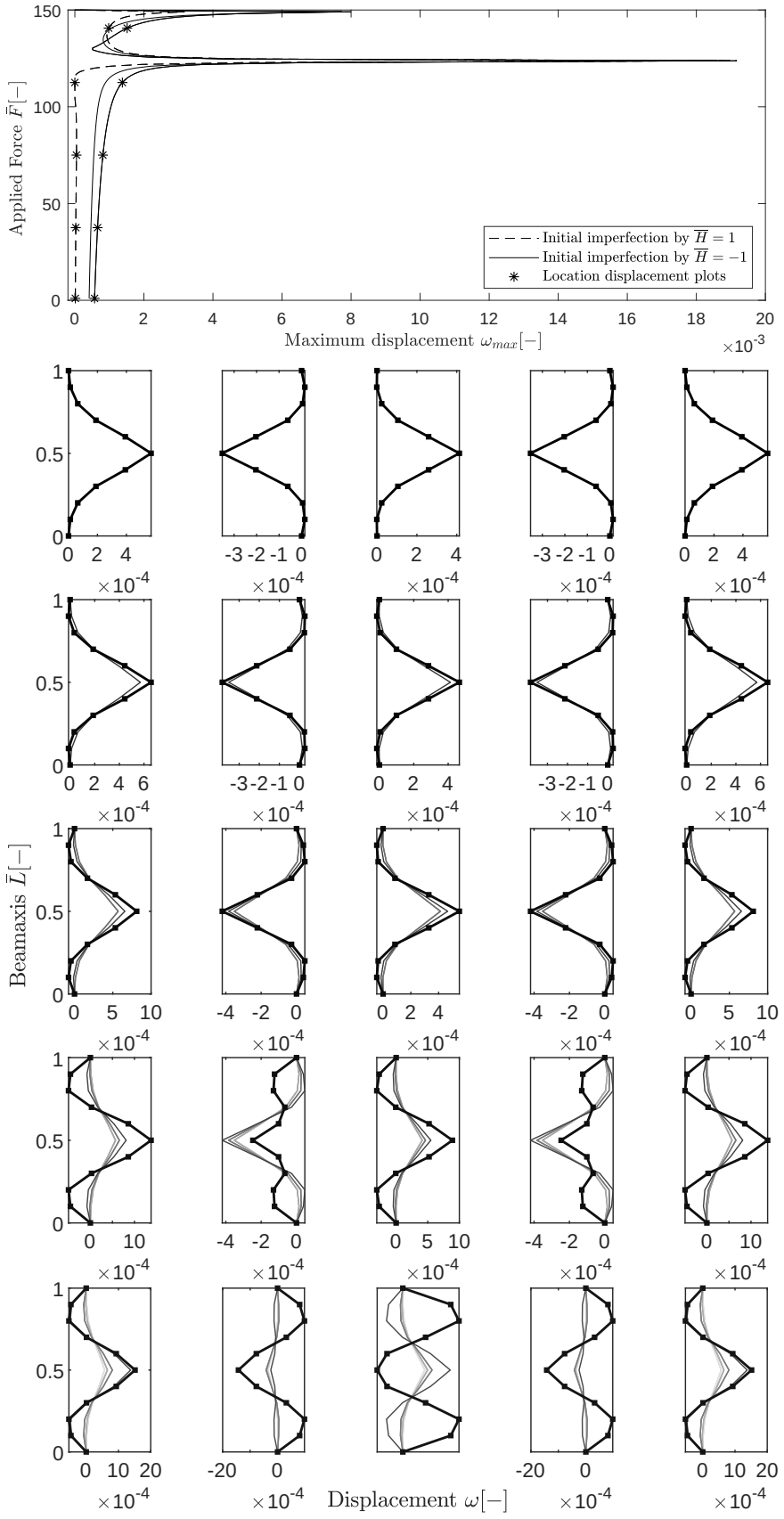

Figure 4.12: Load-displacement curve for fibre bundle in a composite with low fibre volume fraction, modelled using $f(\mathrm{v}_f) = 0.32$ and $g(\mathrm{v}_f) = 0.68$. The displacement of the fibres is shown at several increments.

As an alternative to an initial perturbation load, the initial imperfections can be modelled by imposing a certain buckling mode as initial imperfection to the fibres (as presented in Section 4.1.2). Similar results as shown in Figures 4.10 to 4.12 are obtained for such fibres and the graphs are presented in Appendix B. The same behaviour of the fibres is observed for the first set with $f(\mathrm{v}_f) = 0$ and $g(\mathrm{v}_f) = 1$. For the second set, in-phase buckling is observed. However, the obtained buckling load does not approximate the critical buckling load of an unsupported fibre, but equals the buckling load corresponding to a mode imposed as initial imperfection.
It may be concluded that the fibre volume fraction has a large influence of the buckling load of a single fibre, whether the fibre is a part of a fibre bundle or an individual embedded fibre. The created DEM models are able to capture the influence of the fibre volume fraction using reduction functions for the coupling spring stiffness and matrix spring stiffness. However, more research is required to establish the exact relation between the fibre volume fraction of a composite and the corresponding values of the reduction functions $f(\mathrm{v}_f)$ and $g(\mathrm{v}_f)$, respectively. The values may vary between 0 and 1 and a inverse relationship may be established between both functions based on v_f. It should finally be noted that, the relation of the reduction functions to the fibre volume fraction is required to be able to obtain the failure stress of the composite. In the current research merely the influence of v_f on the buckling load of a single fibre is evaluated.

4.3 Plastic fibre behaviour

The influence of plastic matrix behaviour is evaluated in Section 3.2 and 3.3. In a similar way, the influence of plastic fibre behaviour may be evaluated. The behaviour of the fibre material is approximated using a bilinear material model. From the onset of yielding, the stiffness of the rotational springs is reduced using reduction factor β. The yield stress of the material is related to a certain net rotation in the nodes using the formula for the plastic moment capacity of a circular cross section. Using this relation, the net rotation in a node for which yielding occurs, ϕ_0, is determined. As soon as this value is reached in a certain node, the spring stiffness of the rotational springs is reduced using reduction factor β which depends on the stress-strain diagram of the fibre material in a similar way as described for reduction factor α in Section 3.2 and is illustrated in Figure 3.10. Eventually, the ultimate resistance of the fibre is reached and the spring stiffness of the rotational springs is set to zero:

$$\begin{aligned} &|\phi_n| \leq \phi_0 \rightarrow \overline{C}, \\ &\phi_0 < |\phi_n| < \phi_f \rightarrow \beta \cdot \overline{C}, \\ &|\phi_f| \leq \phi_n \rightarrow \overline{C} = 0. \end{aligned} \tag{4.6}$$

If the modelled matrix and fibre both exhibit non-linear matrix behaviour, the initiation of fibre kinking or plastic micro-buckling of the fibres is observed. In Figure 4.13, the behaviour of a single clamped fibre, present in a fibre bundle is plotted. The initiation of a fibre kink is observed at the node with a net rotation exceeding the rotation associated with fibre plasticity. The kinking occurs at nodes for which in an earlier stage, the matrix has started to show plastic behaviour due to large displacement of the nodes. The stiffness of the springs representing the matrix is then reduced according to Section 3.2, eventually causing large rotations in the nodes with fibre plasticity as a result.
For the fibre in Figure 4.13, another kink is expected to develop at the third or fourth node from below. A fibre behaviour as shown in the micrograph in Figure 4.14 is expected to occur. However, the current DEM models are not able to capture this behaviour yet.
In previous research, fibre kinking has been explained as an matrix shear yield stress and fibre misalignment driven mechanism (Argon, 1972; Budiansky, 1983). To simulate this behaviour correctly, the created DEM models should be developed further by including these influences more accurately. The net displacement and rotation corresponding to the onset of matrix and fibre plasticity respectively, require additional (experimental) research. Moreover, the boundary conditions at the fibre ends are expected to have a large influence on the observed behaviour and may be one of the reasons the current model is unable to fully describe the kinking behaviour.
It is concluded that with the current DEM models, the initiation of fibre kinking is observed, however, it is not yet possible to describe and predict the kinking behaviour of fibre bundles and their corresponding kink-band widths.

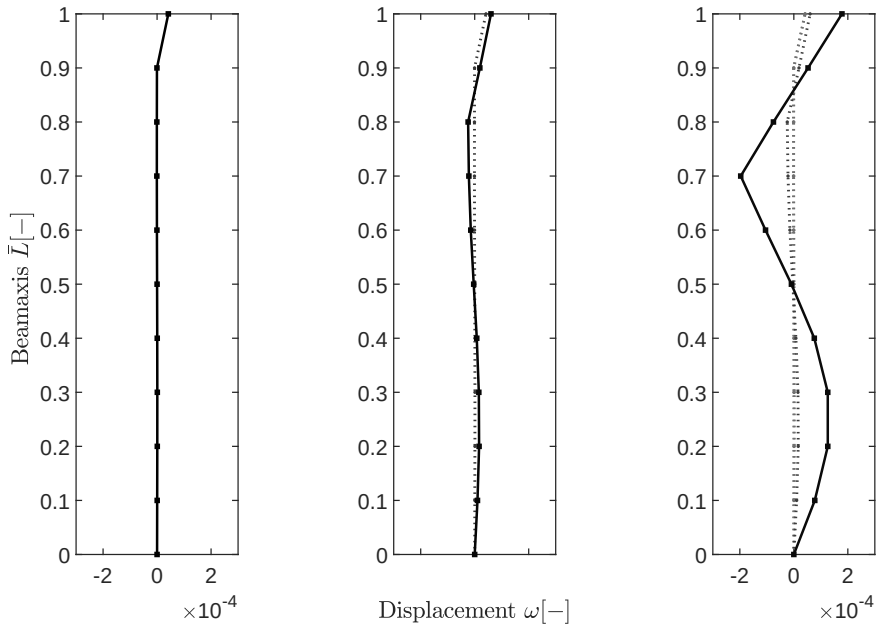

Figure 4.13: The initiation of fibre kinking or plastic fibre behaviour.

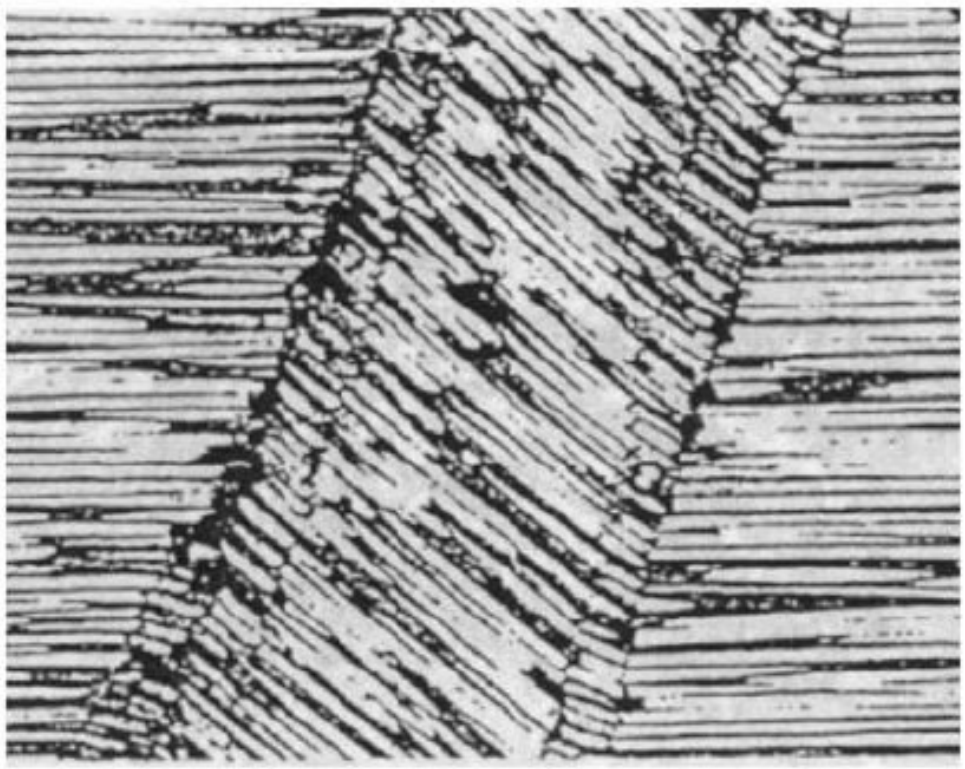

Figure 4.14: Micrograph of plastic micro-buckling or fibre kinking (Feld et al., 2011)

5 Conclusions and recommendations

5.1 Conclusions

A numerical model using the Discrete Element Method has been developed to simulate the behaviour of individual fibres and fibre bundles embedded in a matrix. With this model, the influence of material properties on the micro-buckling of fibres in fibre reinforced composites is analysed, while the complexity, required element types and computational capabilities are kept to a minimum.

Rosen's theory is adopted, approaching embedded fibres as aligned and slender columns supported by an elastic foundation representing the matrix. The critical buckling load of a fibre is obtained using linear buckling analysis, starting from the principle of stationary potential energy. For individual embedded fibres, it is concluded that the buckling load does not decrease monotonically with increasing fibre length, as is the case for unsupported elements. Instead, the fibre buckles according a n-th order mode, in which the associated number of half sines, n, increases with increasing matrix stiffness. The critical buckling load is found to be highly sensitive to small heterogeneities in the bending stiffness of the fibre $E_f I_f$, the fibre length L_f and the foundation modulus of the matrix K_c.

The ability of the DEM model to approximate the bifurcation load accurately, depends on the governing buckling load and boundary conditions at the fibre ends. The number of elements required for the approximation increases when the governing buckling mode increases, i.e. for increasing matrix stiffness. For clamped boundary conditions, the inclination is approximated using the bending stiffness of the fibre. Hence, the model describes the buckling behaviour of fibres with one or more clamped connections less accurately. After comparison with the analytical solution and FEM modelling, it is concluded that both the linear and non-linear DEM models provide accurate predictions of the buckling behaviour of embedded fibres. Moreover, a higher mesh convergence rate is observed for the DEM models than for the FEM models.

Two ways to compute the foundation modulus of the matrix have been evaluated. Following Su et al. (2014), the continuous spring stiffness is computed using Kelvin's solution for the displacement field of an infinite unbounded elastic medium subjected to a concentrated force. Alternatively, a simplified approximation for the continuous spring stiffness is computed using merely the Young's modulus of the matrix. It is concluded that the value of the spring stiffness is linearly dependent on the matrix-fibre stiffness ratio E_m/E_f. The difference between both approximations is found to be independent of the fibre-aspect ratio and merely depends on $\frac{E_m}{E_f}$. For low values of the matrix-fibre stiffness ratio, the difference is sufficiently small, allowing for the application of the more simple approximation of the foundation modulus by $K_c = E_m$.

Plasticity of the matrix is included using a bilinear material model. The stiffness of the springs representing the matrix support is adapted using reduction factor α as soon as the matrix starts to yield. Depending on the moment at which the displacement corresponding to the onset of plastic matrix behaviour is reached, matrix plasticity influences either the critical buckling load, or merely the post-buckling behaviour of the fibres. When modelled in combination with fibre plasticity, plastic matrix behaviour causes the fibres eventually to fail in plastic micro-buckling and the initiation of fibre kinking is observed.

A model for fibre bundles embedded in a matrix is constructed and used to evaluate the influence of initial imperfections and fibre volume fractions on the buckling behaviour of fibres. Besides the springs representing the support of the matrix, coupling springs, connecting adjacent fibre nodes are introduced to capture the fibre-matrix interaction correctly. The fibre volume fraction of the composite material is accounted for by the reduction functions $f(\mathrm{v_f})$ and $g(\mathrm{v_f})$, for the coupling and matrix springs respectively. Although the exact relation between the values of both functions needs to be established in further research, it is observed that for low fibre volume fractions, fibres may buckle out of phase, depending on their initial imperfections and misalignment. For composites with high fibre volume fractions, the limited distance between adjacent fibres causes the fibres to buckle in phase, despite their possibly in opposite direction imposed initial imperfections.

5.2 Recommendations

The DEM models created during this graduation project are able to describe the elastic micro-buckling of embedded fibres accurately and can be used to increase the insight into various relations between fibre behaviour and material parameters of composites. Due to their simplified and clear modelling approach, the models are accessible and may provide users with a quick approximation of the buckling behaviour of the fibres. However, further research and development of the models is required to link the results to the failure behaviour of fibre reinforced composites in practice.
Firstly, experimental research is required to validate the predicted buckling behaviour of the fibres and research the influence of initial imperfections. In the current work, a small imperfection sensitivity study has been executed, however, it is recommended to enlarge the scale of this study and evaluate the modelling approach of imperfections based on observations of unidirectional composite specimens.
Secondly further research should be done in order to link the constitutive matrix and fibre behaviour to the bilinear material model used for the DEM models. Experimental material data is required to obtain the values for the reduction factors α and β which are used for the simulation of plastic matrix and fibre behaviour, respectively. Moreover, other material models describing the true constitutive behaviour of the matrix and fibre may be researched as well, in order to increase the accuracy of the behaviour of fibres under compressive loading.
Additionally, the exact relation between the fibre volume fraction of composites and the reduction functions $f(\mathrm{v_f})$ and $g(\mathrm{v_f})$ should be established if further research is conducted. When the exact relation between both reduction functions and $\mathrm{v_f}$ is known, an extended parameter study may be executed to analyse the influence of the fibre volume fraction more accurately. Moreover, it is recommended to validate the current modelling approach to the fibre volume fraction by comparison with experimental results and comprehensive FEM models.
In this research, the influence of several parameters on the buckling behaviour of fibres is researched, assuming that those fibres are the only load-carrying constituents of a fibre reinforced composite. A buckling load is obtained for those fibres and may be related to the failure stress of the composite using the fibre volume fraction and its relation to the reduction functions. However, in practice, stress will also be applied on the matrix itself. With the matrix having a certain Poisson's ratio, it may be expected that additional support against buckling of the fibres is provided and possibly even other failure modes may intervene. Additionally, the matrix-fibre interaction along the boundary of both materials is recommended for further investigation.

To conclude, firstly, it is recommended to perform experimental research in order to validate the predictions of the buckling behaviour with the current DEM models and extend them with relevant material models. Before an extended parameter study can be conducted, the models should be validated with experimental data and the relations between the constitutive material behaviour and the fibre volume fractions to the reduction factors and functions respectively, should be established. Moreover, it should be verified whether Rosen's approach may indeed be adopted, as done in this project, for the prediction of the compressive failure behaviour of fibre reinforced composites. Secondly, once the models are validated, a larger parameter and imperfection sensitivity study could be conducted. And thirdly, an effort could be made to incorporate other compressive failure mechanisms in the DEM models as well, allowing for the construction of failure maps. Eventually, the model may even be expanded to be able to predict the failure behaviour of other fibre architectures and orientations as well.

Although, as summed up above, extensive further research could be conducted on the modelling of compressive failure of fibre reinforced composites with the DEM, a critical note has to be made with regard to the added value of this research to the existing knowledge within this field of science. From extensive previous research, numerous ways to predict the failure of fibre reinforced composites have been established. Among others, comprehensive FEM models and sophisticated homogenisation techniques have been developed, which are able to predict the failure mechanisms of composites with great accuracy. It is therefore expected that value of the created DEM models lies in particular in their accessibility and their capability to provide a quick understanding of the governing relations between material properties and the micro-buckling of embedded fibres, while still providing a sufficiently accurate prediction of the failure load.

References

Alfutov, N. A. (2011). *Stability of elastic structures.* Springer.

Altenbach, H., Altenbach, J., & Kissing, W. (2018). *Mechanics of composite structural elements.* Springer.

Andrianov, I. V., Kalamkarov, A. L., & Weichert, D. (2012). Buckling of fibers in fiber-reinforced composites. *Composites Part B: Engineering*, *43*(4), 2058–2062.

Argon, A. S. (1972). Fracture of composites. *Treatise on Materials Science and Technology*, 79–114.

Batoz, J.-L., & Dhatt, G. (1979). Incremental displacement algorithms for nonlinear problems. *International Journal for Numerical Methods in Engineering*, *14*(8), 1262–1267.

Bos, D. H. (2019). *Effects of imperfections on axially loaded members and experimental verification on 3d printed polypropylene* (Unpublished master's thesis). Eindhoven University of Technology, The Netherlands.

Budiansky, B. (1983). Micromechanics. *Computers and Structures*, *16*(1-4), 3–12.

Crisfield, M. A. (1981). A fast incremental/iterative solution procedure that handles "snap-through". *Computers and Structures*, *13*(1-3), 55–62.

El Naschie, M. S. (1990a). The discrete element method. In *Stress, stability and chaos in structural engineering: an energy approach* (chap. 8). Mc Graw Hill.

El Naschie, M. S. (1990b). Energy and variational principles. In *Stress, stability and chaos in structural engineering: an energy approach* (chap. 6). Mc Graw Hill.

El Naschie, M. S. (1990c). The work of internal forces - strain energy. In *Stress, stability and chaos in structural engineering: an energy approach* (chap. 2). Mc Graw Hill.

El-Naschie, M. S., Wu, C. W., & Wifi, A. S. (1988). A simple discrete element method for the initial postbuckling of elastic structures. *International Journal for Numerical Methods in Engineering*, *26*(9), 2049-2060.

Fafard, M., & Massicotte, B. (1993). Geometrical interpretation of the arc-length method. *Computers and Structures*, *46*(4), 603–615. doi: 10.1016/0045-7949(93)90389-u

Feld, N., Allix, O., Baranger, E., & Guimard, J.-M. (2011, 10). Micro-mechanical prediction of ud laminates behavior under combined compression up to failure: Influence of matrix degradation. *Journal of Composite Materials*, *45*, 2317-2333.

Fleck, N. A. (1997). Compressive failure of fiber composites. *Advances in Applied Mechanics*, *33*, 43–117.

Fleck, N. A., & Budiansky, B. (1991). Compressive failure of fibre composites due to microbuckling. *Inelastic Deformation of Composite Materials*, 235–273.

Herrmann, L. R., Mason, W. E., & Chan, S. T. K. (1967). Response of reinforcing wires to compressive states of stress. *Journal of Composite Materials*, *1*(3), 212–226.

Hoff, N. J. (1966). *The analysis of structures.* Wiley.

Holtzer, B. P. F. (2017). *Topology optimization of geometrically nonlinear structures* (Unpublished master's thesis). Delft University of Technology, The Netherlands.

Lanir, Y., & Fung, Y. C. B. (1972, Jul). Fiber composite columns under compression. *Journal of Composite Materials*, *6*(3), 387–401.

Mallick, P. K. (2008). *Fiber-reinforced composites: materials, manufacturing, and design.* CRC Press.

Parnes, R., & Chiskis, A. (2002). Buckling of nano-fibre reinforced composites: a re-examination of elastic buckling. *Journal of the Mechanics and Physics of Solids*, *50*(4), 855–879.

Phoenix, S., & Beyerlein, I. J. (2000, 12). Statistical strength theory for fibrous composite materials. In (Vol. 1, p. 559-639).

Ritto-Corrêa, M., & Camotim, D. (2008). On the arc-length and other quadratic control methods: Established, less known and new implementation procedures. *Computers and Structures*, *86*(11-12), 1353–1368.

Savage, G. (2010). Formula 1 composites engineering. *Engineering Failure Analysis*, *17*(1), 92 - 115.

Scappin, N. (2017). *Experimental observations and fe modelling of fibre kinking in the presence of constraints* (Unpublished master's thesis). Eindhoven University of Technology, The Netherlands.

Spowart, J. E., & Dève, H. E. (2000). 3.09 - compressive failure of metal matrix composites. In A. Kelly & C. Zweben (Eds.), *Comprehensive composite materials* (p. 221 - 245). Oxford: Pergamon. Retrieved from http://www.sciencedirect.com/science/article/pii/B0080429939001248

Su, T., Liu, J., Terwagne, D., Reis, P. M., & Bertoldi, K. (2014, Jun). Buckling of an elastic rod embedded on an elastomeric matrix: planar vs. non-planar configurations. *Soft Matter*, *10*(33), 6294–6302.

Suiker, A. S. J., Askes, H., & Sluys, L. J. (n.d.). Micro-mechanically based 1-d gradient damage models. In *Proceedings european congress on computational methods in applied sciences and engineering.* Barcelona: ECCOMAS 2000.

Timoshenko, S. P., & Gere, J. M. (1961). *Theory of elastic stability.* McGraw-Hill.

Ueda, M., Hiraga, A., & Nishimura, T. (2011, 01). Compressive strength of a carbon fiber in matrix. *Journal of the Japan Society for Composite Materials*, *37*, 103-110.

Vasios, N. (2015). *Nonlinear analysis of structures - the arc length method: Formulation, implementation and applications.* Harvard.

Zhao, Y., Li, J., Cao, Y. P., & Feng, X.-Q. (2016, Jan). Buckling of an elastic fiber with finite length in a soft matrix. *Soft Matter*, *12*(7), 2086–2094.

Zhou, L., Zhao, L., Liu, F., & Zhang, J. (2018). A micromechanical model for longitudinal compressive failure in unidirectional fiber reinforced composite. *Results in Physics*, *10*, 841–848.

Zhou, Z., & Murray, D. W. (1995). An incremental solution technique for unstable equilibrium paths of shell structures. *Computers and Structures*, *55*(5), 749–759.

Appendix

A Non-linear buckling analysis - implementation of the Arc length method

A non-linear buckling analysis is implement in MATLAB following the procedure as outlined in 2.2.5. In this section, as an example of the implementation of a non-linear buckling analysis, the programmed MATLAB code is presented for the Newton-Raphson with arc length control and strategies for additional robustness.

MATLAB script - Main file

```
%% BUCKLING BEHAVIOR OF FIBRES EMBEDDED IN MATRICES
%  NON LINEAR BUCKLING ANALYSIS WITH DISCRETE ELEMENT METHOD
%  ITERATIVE NEWTON-RAPHSON SCHEME WITH ARCLENGTH CONTROL
%  BHHA CORDEWENER 2019

%%%%%%%%%%%%%%%%%%%%%%%%%%%%%%%%%% MAIN FILE
    %%%%%%%%%%%%%%%%%%%%%%%%%%%%%%%%%%
clear all;
close all;
clc;

%% Simulation parameters
% #itmax#       is the maximum number of iterations permitted for
    each increment.
% #itdes#       is the desired number of iterations per increment
% #conv_crit#   is the tolerance for the convergence criterium of R
% #pert#        is the numerical perturbation for calculating
    derivatives
% #psi#         corresponds to the version of the Crisfield method
    used.
%               Its value is 1 in case of spherical, 0 in case of
    cylindrical and
%               psi>0 ~1 in case of elliptical arc length control
% #AL#          is the initial value of the arc length increment

simpar={100 20 3 1e-8 1e-6 1 1 1 25 1e-1};
[tmax,itmax,itdes,conv_crit,pert,psi,AL,ds,ALmax,ALmin]=simpar{:};

%% Parameterset
% #bc#      is the boundary condition represented by a pair of
    letters.
%           c=clamped, f=free, p=pinned. 4 combinations are
    possible: pp, cc, cf(=fc), cp(=pc)
% #H#       is the horizontal perturbation load to initiate the NL
    analysis
% #k#       is the dimensionless discrete springstiffness of the
    matrix
% #BLF#     is the BiLinearityFactor of the spring of the matrix
% #u0#      is the dimensionless displacement corresponding to the
    start of
%           the binlinear traject of the spring representing the
    matrix
% #m#       the number of discrete elements used to simulate the
    fiber
```

```
33
34 modelpar = {'pp' 5 500 1 0 100 100 10 2500};
35 [bc,H,k,BLF,KVF,u0,uv0,m,Ftot] = modelpar{:};
36
37 %% Calculation
38 % Initialize variables
39 if bc == 'cf'
40     var= zeros(m,1);      % var=[phi] when no symmetry
41 else
42     var= zeros(m+1,1);    % var=[phi;Lgrs]  when symmetry (extra
       constraint)
43 end
44 Dvar= zeros(length(var),1);
45 DF=zeros;
46 F= zeros;
47
48 % Initialize counters
49 it = 0;
50 t = 0;
51 cmov = 1;
52
53 %% Increment loop
54 R = getRfhc(m,bc,H,F,var)+ getRk(m,bc,var,k,BLF,KVF,u0,uv0);
55
56 while t<=tmax && F<Ftot
57     t=t+1
58
59     % Predictor stage
60     dR = getdR(m,bc,H,F,k,BLF,KVF,u0,uv0,var,pert);
61     Fex= getFex(m,bc,H,F,var,pert);
62
63     dvarres = -dR\R;
64     dvarext =  dR\Fex;
65
66     if t==1
67         dF = AL/(sqrt(dvarext.'*dvarext+psi.^2));
68     else
69         if dvarext.'*Dvar+psi.^2*DF>=0
70             dF = AL/(sqrt(dvarext.'*dvarext+psi.^2));
71         else
72             dF =-AL/(sqrt(dvarext.'*dvarext+psi.^2));
73         end
74     end
75     DF=DF+dF;
76     F=F+dF
77     dvar=dvarres+dF*dvarext;
78     Dvar=Dvar+dvar;
79     var =var +dvar;
80
81     R = getRfhc(m,bc,H,F,var)+ getRk(m,bc,var,k,BLF,KVF,u0,uv0);
82     Residu = sqrt(sum(R.^2));
83
84     %% Iterative loop
85     while it<=itmax && Residu>conv_crit
86         it=it+1
87
```

```
88          dR = getdR(m,bc,H,F,k,BLF,KVF,u0,uv0,var,pert);
89          Fex= getFex(m,bc,H,F,var,pert);
90
91          dvarres = -dR\R;
92          dvarext =  dR\Fex;
93
94          % Corrector stage
95          a = dvarext.'*dvarext + psi.^2;
96          b0= 2*dvarext.'*Dvar+2*psi.^2*DF;
97          b1= 2*dvarext.'*dvarres;
98          b = b0+b1*ds;
99          % b = 2*dvarext.'*(Dvar+dvarres)+2*psi.^2*DF
100         c0= Dvar.'*Dvar+psi.^2*DF.^2-AL^2;
101         c1= 2*dvarres.'*Dvar;
102         c2= dvarres.'*dvarres;
103         c = c0+c1*ds+c2*ds^2;
104         %c = (Dvar+dvarres).'*(Dvar+dvarres)+psi.^2*DF.^2-AL^2
105
106         if b^2-4*a*c<0 % using partial corrections in case of
                complex roots
107             as=b1^2-4*a*c2;
108             bs=2*b0*b1-4*a*c1;
109             cs=b0^2-4*a*c0;
110             if abs(as)<eps
111                 ds=-cs/bs; % quadratic equation reduces to linear
                        equation
112             elseif bs^2-4*as*cs<0 && as>0 % b^2-4*a*c>0 for all
                    real Deltas
113                 ds=-bs/(2*as); % global optimum
114             else
115                 sqrtds=eig([-bs/as -cs/as;1 0]);
116                 ds1=sqrtds(1);
117                 ds2=sqrtds(2);
118                 ds=max([ds1,ds2]);
119             end
120             % Decreasing step length if ds<0.1
121             if ds<0.1 || it==itmax
122                 AL=0.5*AL;
123             end
124             % recalculate b and c with partial correction ds
125             b = b0+b1*ds;
126             c = c0+c1*ds+c2*ds^2;
127         end
128
129         % Calculate dF
130         if abs(a)<eps
131             dF=-c/b; % quadratic equation reduces to linear
                    equation
132         else
133             dF1= (-b/(2*a)+sqrt(abs(b^2/(4*a^2)-c/a)))
134             dF2= (-b/(2*a)-sqrt(abs(b^2/(4*a^2)-c/a)))
135             % Corrector root selection
136             dot= Dvar.'*dvarext+psi^2*DF;
137             if dot*dF1>dot*dF2
138                 dF=dF1;
139             else
```

```
140                     dF=dF2;
141                 end
142             end
143             dF
144             % Proceed to next iterative solution point
145             DF=DF+dF;
146             F=F+dF
147             dvar=dvarres+dF*dvarext;
148             Dvar=Dvar+dvar;
149             var =var +dvar;
150 
151             R = getRfhc(m,bc,H,F,var)+ getRk(m,bc,var,k,BLF,KVF,u0,uv0)
                    ;
152             Residu = sqrt(sum(R.^2));
153         end
154         % store output
155         Fout(t,1)=F
156         [w,wv,wmax] = getdispl(m,bc,var);
157         Uout(t,1)=wmax
158         ALout(t,1)=AL
159         itout(t,1)=it;
160         dsout(t,1)=ds;
161         varout(:,t)=var;
162         wout(:,t)=w';
163         wvout(:,t)=wv';
164 
165         % Reinitialisation parameters
166         ds=1
167         AL=min(AL*(itdes/it)^0.5,ALmax)
168         it=0
169         Dvar= zeros(length(var),1);
170         DF=zeros;
171 
172         % Plot shapes during simulation
173         if mod(t,5)==0
174             for cshapey=1:m
175                 shapey(cshapey+1)= 1/m*sum(cos(var(1:cshapey)));
176             end
177             shapex=[0 w];
178             plot(shapex,shapey,'-s')
179             ylim=([0 1]);
180             xlabel('Horizontal displacement $\bar{U}$ ','Interpreter','
                    Latex')
181             ylabel('Beamaxis $\bar{L}$ ','Interpreter','Latex')
182             drawnow
183             frame(cmov)=getframe;
184             cmov=cmov+1;
185             hold on
186         end
187 end
188 %% Save and plot
189 figure
190 plot(Uout,Fout)
191 xLim = get(gca, 'XLim')
192 xlabel('Displacement $\bar{U}$ ','Interpreter','Latex')
193 ylabel('Force $\bar{F}$ ','Interpreter','Latex')
```

```
194
195 figure
196 plot(wvout(m,:),Fout)
197 xLim = get(gca, 'XLim')
198 xlabel('Vertical displacement $\bar{U_{v}}$ ','Interpreter','Latex'
    )
199 ylabel('Force $\bar{F}$ ','Interpreter','Latex')
```

MATLAB script - Subroutine Rfhc

```
1  %% NONLINEAR BUCKLING ANALYSIS
2  %  DISCRETE ELEMENT METHOD
3  %  BHHA CORDEWENER 2019
4
5  %%%%%%%%%%%%%% SUBROUTINE %%%%%%%%%%%%%%
6
7  function [R] = getRfhc(m,bc,H,F,var)
8  R=zeros(length(var),1);
9
10 if bc == 'pp'
11     R(1)= m*(var(2)-var(1));
12 else
13     R(1)= m*(var(2)-2*var(1));
14 end
15
16 if bc == 'cc'
17     R(m)= m*(var(m-1)-2*var(m));
18 else
19     R(m)= m*(var(m-1)-var(m));
20 end
21
22 for i=2:m-1
23     R(i) = m*(var(i-1)+var(i+1)-2*var(i));
24 end
25
26 if bc == 'cf'
27     for i=1:m
28         R(i)=R(i)+F/m*sin(var(i))+H/m*cos(var(i));
29     end
30 else
31     for i=1:m
32         R(i)=R(i)+F/m*sin(var(i))-var(m+1)/m*cos(var(i));
33     end
34     for i=1:fix(m/2)
35        R(i)=R(i)+0.5*H/m*cos(var(i));
36     end
37     for i=1:round(m/2)
38         R(i)=R(i)+0.5*H/m*cos(var(i));
39     end
40     R(m+1)=-sum(sin(var(1:m)))/m;
41 end
42 end
```

MATLAB script - Subroutine Rk

```
%% NONLINEAR BUCKLING ANALYSIS
%  DISCRETE ELEMENT METHOD
%  BHHA CORDEWENER 2019

%%%%%%%%%%%%%% SUBROUTINE %%%%%%%%%%%%%%

function [Rk] = getRk(m,bc,var,k,BLF,KVF,u0,uv0)
Rk=zeros(length(var),1);
% Computation of elastic residuals
for i=1:m
    for ii=1:m
        Rke(i,ii)=-k/m^2*cos(var(i))*sum(sin(var(1:ii)));
        Rkve(i,ii)=-(k*KVF)/m^2*sin(var(i))*(ii-sum(cos(var(i:ii)))
            );
    end
end
Rke=triu(Rke);
Rkve=triu(Rkve);
% Computation of plastic residuals
for i=1:m
    for ii=1:m
        Rkp(i,ii)=-k/m*cos(var(i))*(BLF/m*sum(sin(var(1:ii)))+u0
            *(1-BLF));
        Rkvp(i,ii)=-(KVF*k)/m*sin(var(i))*(BLF/m*(ii-sum(cos(var(1:
            ii))))+u0*(1-BLF));
    end
end
Rkp=triu(Rkp);
Rkvp=triu(Rkvp);
% Checking for elastic or plastic behaviour
[w,wv,wmax] = getdispl(m,bc,var);
for i=1:m
    if abs(w(i)) <= u0
        Rkm(:,i)=Rke(:,i);
    else
        Rkm(:,i)=Rkp(:,i);
    end

    if abs(wv(i)) <=uv0
        Rkmv(:,i)=Rkve(:,i);
    else
        Rkmv(:,i)=Rkvp(:,i);
    end
end

for i=1:m
    Rk(i)=sum(Rkm(i,:))+ sum(Rkmv(i,:));
end
```

MATLAB script - Subroutine dR

```
%% NONLINEAR BUCKLING ANALYSIS
%  DISCRETE ELEMENT METHOD
%  BHHA CORDEWENER 2019

%%%%%%%%%%%%%%% SUBROUTINE %%%%%%%%%%%%%%%

function [dR] = getdR(m,bc,H,F,k,BLF,KVF,u0,uv0,var,pert)
dR=zeros(length(var),length(var));

varR=repmat(var,1,length(var)) + eye(length(var))*pert;

for i=1:length(var)
    dR(:,i)=(getRfhc(m,bc,H,F,varR(:,i))+ getRk(m,bc,varR(:,i),k,
       BLF,KVF,u0,uv0)-getRfhc(m,bc,H,F,var)-getRk(m,bc,var,k,BLF,
       KVF,u0,uv0))/pert;
end

end
```

MATLAB script - Subroutine Fex

```
%% NONLINEAR BUCKLING ANALYSIS
%  DISCRETE ELEMENT METHOD
%  BHHA CORDEWENER 2019

%%%%%%%%%%%%%%% SUBROUTINE %%%%%%%%%%%%%%%

function [Fex] = getFex(m,bc,H,F,var,pert)
Fex=zeros(length(var),1);
Fex=(getRfhc(m,bc,H,(F+pert),var)-getRfhc(m,bc,H,F,var))/pert;
end
```

MATLAB script - getdispl

```
%% NONLINEAR BUCKLING ANALYSIS
%  DISCRETE ELEMENT METHOD
%  BHHA CORDEWENER 2019

%%%%%%%%%%%%%%% SUBROUTINE %%%%%%%%%%%%%%%

function [w,wv,wmax] = getdispl(m,bc,var)

for cw=1:m %cw is counter over w
    w(cw)= 1/m*sum(sin(var(1:cw)));
end

for cwv=1:m %cw is counter over w
    wv(cwv)= cwv*1/m-1/m*sum(cos(var(1:cwv)));
end

  if bc == 'cf'
        wmax=w(m);
    else
        wmax=mean([w(round(m/2)) w(fix(m/2))]);
  end
end
```

B Influence of v_f on fibres with buckling modes as initial imperfection

The initial imperfections of fibres within a fibre bundle can be modelled by imposing a certain buckling mode as initial imperfection to the fibres (as presented in Section 4.1.2). A similar buckling behaviour of the fibres is observed as was found for fibres subjected to a small perturbation load as initial imperfection (as shown in Figures 4.10 to 4.12). On the next pages, the load-displacement curve and fibre displacements are shown for fibres with an initial imperfection defined by a certain buckling mode.

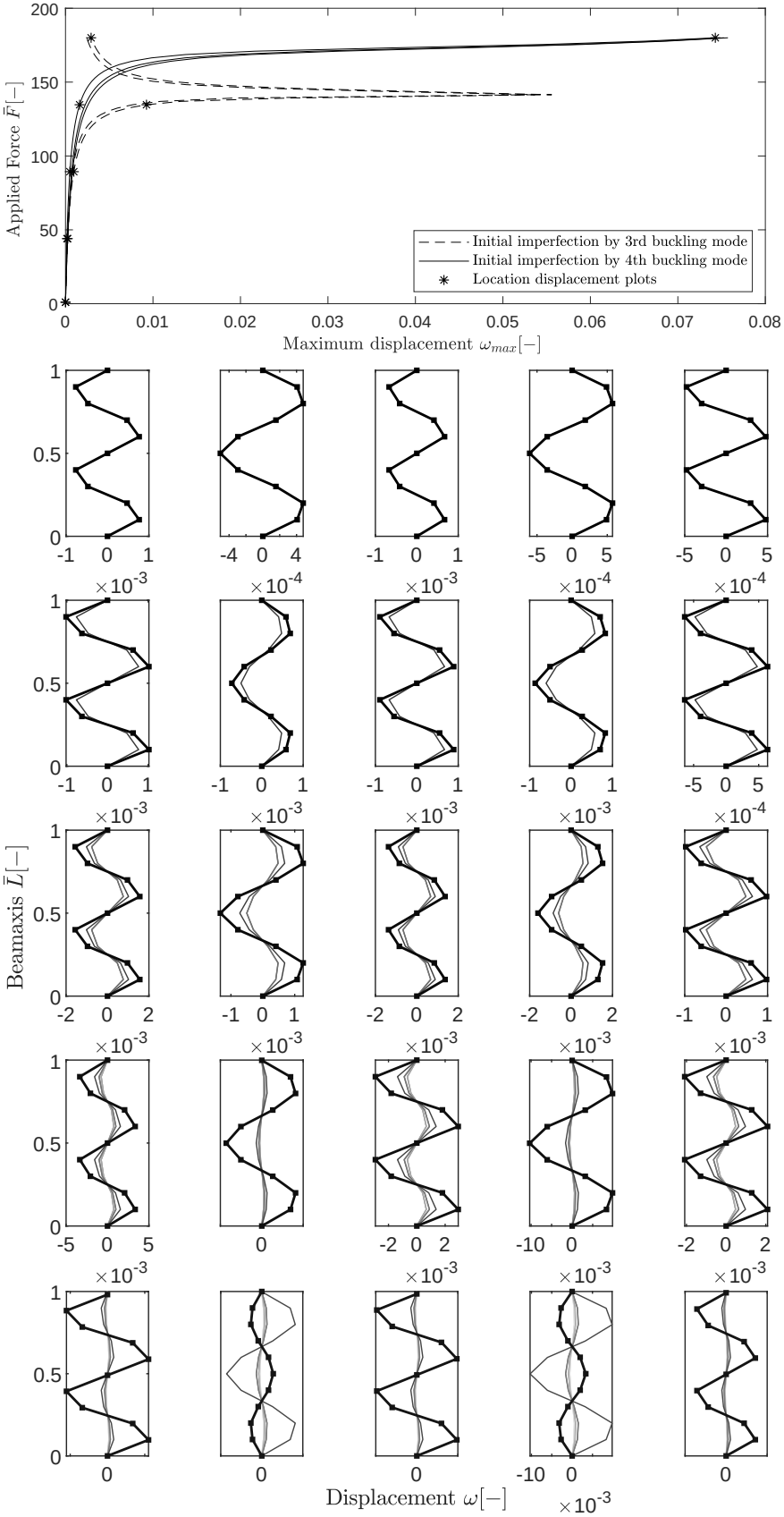

Figure B.1: Load-displacement curve for fibre bundle in a composite with low fibre volume fraction, modelled using $f(\mathrm{v_f}) = 0$ and $g(\mathrm{v_f}) = 1$. The fibres have either a 3rd or 4th buckling mode as initial imperfection and their displacement are shown at several increments.

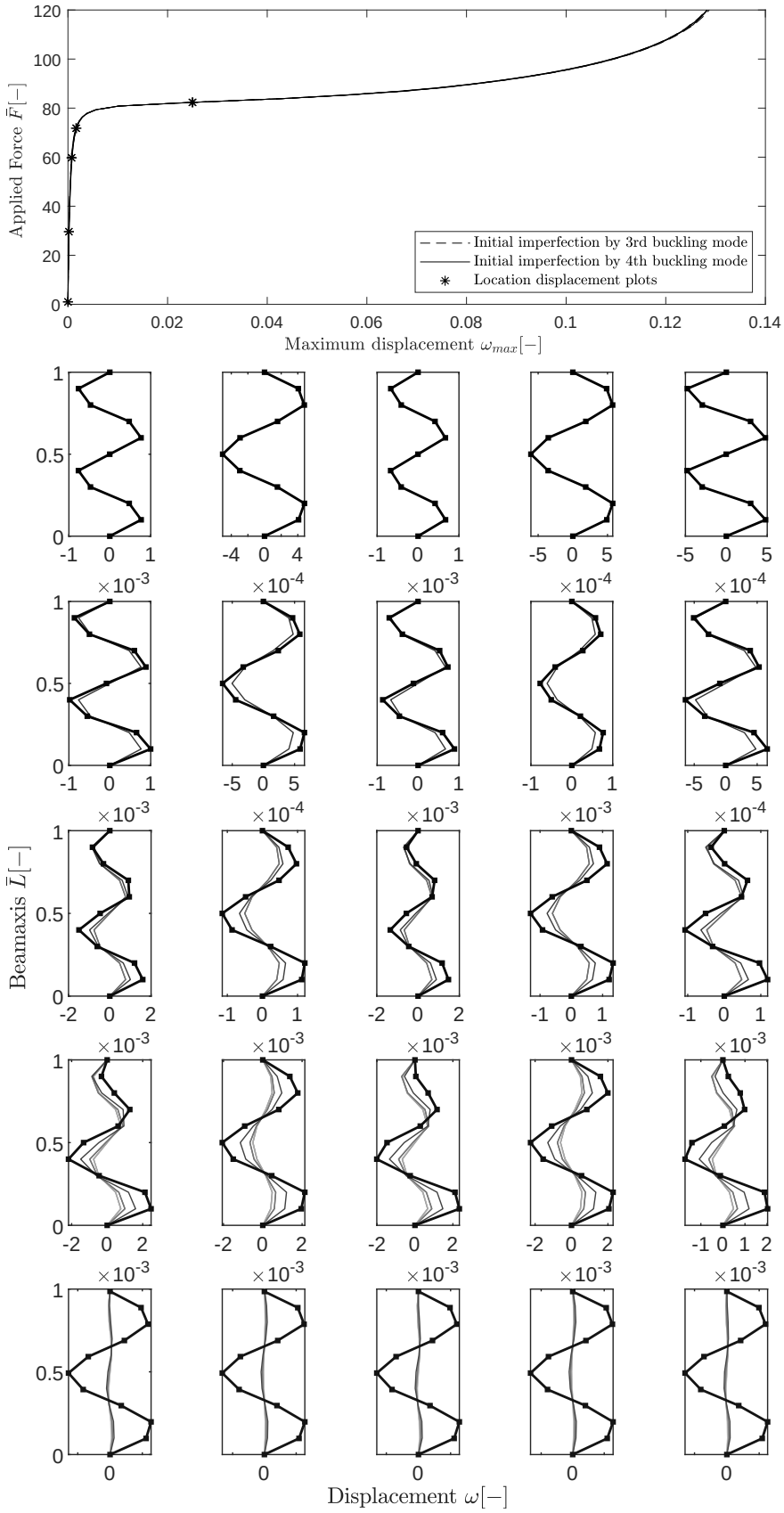

Figure B.2: Load-displacement curve for fibre bundle in a composite with high fibre volume fraction, modelled using $f(\mathrm{v_f}) = 1$ and $g(\mathrm{v_f}) = 0$. The fibres have either a 3rd or 4th buckling mode as initial imperfection and their displacement are shown at several increments.

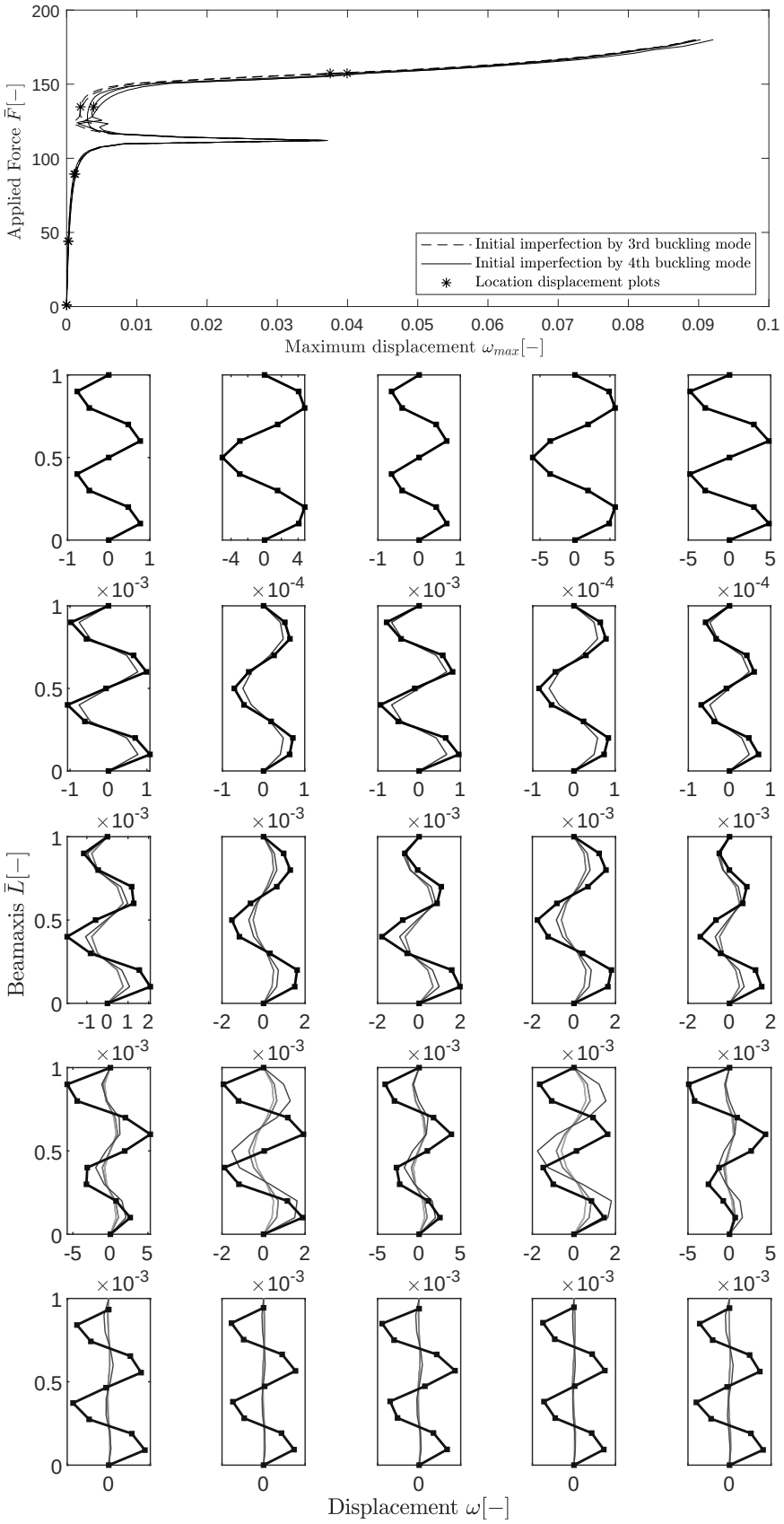

Figure B.3: Load-displacement curve for fibre bundle in a composite with low fibre volume fraction, modelled using $f(\mathrm{v_f}) = 0$ and $g(\mathrm{v_f}) = 1$. The fibres have either a 3rd or 4th buckling mode as initial imperfection and their displacement are shown at several increments.

DEPARTMENT OF THE BUILT ENVIRONMENT
MASTER ARCHITECTURE, BUILDING AND PLANNING
UNIT STRUCTURAL ENGINEERING AND DESIGN
CHAIR OF APPLIED MECHANICS